Rheology of Dense Granular Mixtures and Slurries

A DISSERTATION
SUBMITTED TO THE FACULTY OF THE GRADUATE SCHOOL
OF THE UNIVERSITY OF MINNESOTA
BY

Bereket Yohannes Tewoldebrhan

IN PARTIAL FULFILLMENT OF THE REQUIREMENTS
FOR THE DEGREE OF
Doctor of Philosophy

Kimberly M. Hill

September, 2012

Acknowledgements

It is a pleasure to thank the many people who made this thesis possible. First of all, I would like to thank my advisor Prof. Kimberly M. Hill for the technical guidance and financial support. I have benefitted greatly from the collaborations with Prof. William E. Dietrich (University of California at Berkeley). Continuous encouragement and discussions with Prof. Chris Paola have made this thesis much better. I would also like to thank the rest of my thesis committee Prof. Lev Khazanovich, Prof. Vaughan Voller, and Prof. James Kakalios. I enjoyed working with Prof. Dietrich's students Leslie Hsu, Marisa C. Palucis and Roland Kaitna on the rotating drum experiments. I also thank former students in our group Jiafeng Zhang, Leslie Dellangelo, Jehoo Yoo, Greg Shaffer, Meghan Flanagen, John Gaffney, and Kirby Templin for providing essential feedbacks and encouragement. I thank my friends Mizan Haddish, Mary Vancura, and Isaias Petros for tirelessly encouraging me throughout my graduate studies. I also enjoyed my friendship with fellow students Eyoab Zegeye, Mohammed Hajit, Vamsi Ganti, Paola Passalacqua, Arvind Singh, Mohammed Ebtehaj, Jorge Lorenzo, and Man Liang.

My deepest appreciation goes to my family. My elder brother Minassie encouraged me to pursue graduate school and worked on the application process on the behalf of me. Without the continuous support, comfort, encouragement, and prayer from my Mom Fanus and Dad Yohannes, graduate school would have been impossible. The love and kindness of my younger brother Ephraim and my two beautiful sisters Bethel and Mahlet have always added a big smile to my face. My family is my hero.

The love, kindness, and humor of my most beloved Nbsrat is a strength and reason to go on. Had it not been for her love, everything would have lost its taste. I thank God about her and everything else!

Dedication

To my beloved mom.

Abstract

Dense granular flows, characterized by multiple contacts between grains, are common in many industrial processes and natural events, such as debris flows. Understanding the characteristics of these flows is crucial to predict quantities such as bedrock erosion and distance traveled by debris flows. However, the rheological properties of these flows are complicated due to wide particle size distribution and presence of interstitial fluids. Models for dense sheared granular materials indicate that their rheological properties depend on particle size, but the representative particle size for mixtures is not obvious. Using the discrete element method (DEM) we study sheared granular binary mixtures in a Couette cell to determine the relationship and rheological parameters such as stress and effective coefficient of friction and particle size distribution. The results indicate that the stress does not depend monotonically on the average particle size as it does in models derived from simple dimensional consideration. The stress has an additional dependence on a measure of the effective free volume per particle that is adapted from an expression for packing of monosized particles near the jammed state. The effective friction also has a complicated dependence on particle size distribution. For these systems of relatively hard particles, these relationships are governed largely by the ratio between average collision times and mean-free-path times. The characteristics of shallow free surface flows, important for applications such as debris flows, are different from confined systems. To address this, we also study shallow granular flows in a rotating drum. The stress at the boundary, height profiles and segregation patterns from DEM simulations are quantitatively similar to the results obtained from physical experiments of shallow granular flows in rotating drums. Individual particle-bed impacts rather than enduring contacts dominate the largest forces on the drum bed, which vary as the grain size squared and the 1.2 power of particle-bed impact velocity. In the presence of interstitial fluids (water + fine particles) these characteristics might change significantly. Modeling particle-particle and fluid-particle interaction in dense granular flows is still a challenge. We propose a modification to the DEM to account for specific effects of the interstitial fluid on the dynamics of certain granular fluid flows. The results from this simple model are qualitatively similar to results from experiments.

Contents

List of Tables

List of Figures

Chapter 1

Introduction

Granular materials are present in a variety of natural phenomena and industrial processes [1, 2, 3]. Examples include debris flows, avalanches, sandpiles, pharmaceutical powders and food grains. Granular materials are sometimes described [4] as a large conglomeration of discrete particles. The size of the particles within a granular material can vary from that of very fine particles on the order of micrometers to that of large boulders of the order of meters. The properties of individual particles within a granular material, such as shape, stiffness and roughness, may also vary. In addition to the particles, granular materials may also contain some liquid. Such granular materials are usually referred to as slurries.

The behaviors of a granular material depend on the properties of individual particles, interparticle interactions, particle-fluid interactions, and imposed boundary conditions [5, 6, 7]. The particle properties and associated particle-particle and particle-fluid interactions can be considered as microscopic measures which dictate the macroscopic characteristics of a granular material. Due to the presence of large numbers of particles, granular materials possess a very high degree of freedom, which makes accurate prediction of the behavior of granular materials difficult. Much research has been performed to understand the kinematics and dynamics of granular materials. Some granular materials research has been driven by pure scientific interest [4], and other granular materials research has been driven by the important application of granular materials on a daily basis in various processes [8].

One of the earliest of applications of flowing granular materials is the hourglass,

which was used to measure time in some situations [9]. However, other than Reynolds research on dilatancy (the expansion of granular materials under shear) [10] there has been little systematic research on granular materials until recently. Recent research on granular materials is wide-reaching and includes experiments [11], simulations [12] and analytic solutions [13]. Perhaps the most notable and wide-reaching research results on granular flows involved Bagnold's [11] theoretical hypotheses and experimental studies on stresses in sheared suspended granular materials. However, the complicated nature of granular materials makes it difficult to simply apply results, such as these from Bagnold's research, to all types and states of granular materials because of the sensitivity of their behaviors to particle type and boundary conditions.

One of the challenges of modeling granular materials is that under different types of boundary conditions the constitutive laws change dramatically. The different behaviors are often categorized in terms of specific regimes or states: solid, liquid and gaseous states [4, 14, 15, 8, 16]. Constitutive laws formulated for one state are typically inapplicable to another state. Specific factors that have been associated with determining the state of a granular material include applied stress, solid volume fraction (or its opposite, porosity), velocity fluctuations and physical properties of the particles. Granular materials behave as solids at the limits of low shear stress, high normal stress, high solid volume fractions, and low velocity fluctuations [17]. On the other hand, granular materials behave as gases at the limits of high shear stress, low normal stress, low solid volume fractions and high velocity fluctuations. At intermediate values of stresses, solid volume fractions, and velocity fluctuations, granular materials behave in many ways as liquids.

For example, in many geotechnical and packing applications the granular materials behave as solids. In such cases deformations in response to applied stresses are very small and rate independent. These types of deformations are usually referred to as quasi-static flows. Various theories, taking forms similar to the theory of plasticity, are usually used as a framework to model the macroscopic quasi-static deformations of granular materials [17]. At the microscopic, i.e., particle-scale, level the solid state of a granular material is usually associated with persistent and enduring contact between the particles. The contacts typically organize into force chains [18, 19]. In solid-like granular materials composed of relatively uniformly sized spherical particles, each particle is on average in

contact between four and six other particles [20]. At the limit of highest solid volume fraction the particles in a granular material are hexagonally close packed; each particle is in contact with 12 other particles and the solid volume fraction is about 74%. Recent modeling efforts for the solid-like granular state have included consideration of statistics of the microscopic measures of the system such as force chains and the coordination number (the average number particles that are in contact with each particle) along with the properties of the particles such as the coefficient of friction and stiffness.

Alternatively, in many industrial applications when a granular material is violently shaken in a closed container, or poured from a chute, the solid volume fraction is low and/or the velocity fluctuations of the particles are high, and the granular material behaves like a gas. The macroscopic measures of gas-like flows are dependent on the rate of application of the stress or strain. In this state the particles spend most of the time without touching other particles. Most of the contacts between the particles are binary, that is, most of the particles that are in contact with *any* particle are in contact only with one other particle, and the contacts are typically collisional (the particles rebound with well-defined rebound velocities). In these binary collisional contacts the contact duration is also well-defined and depends on many factors including the stiffness and mass of the particles. The contact duration also weakly depends on the relative velocity of the two particles [21]. Kinetic theory of dense gases has been adapted to modeling these gas-like granular materials [13]. Essentially, statistics of particle collisions are modeled based on microscopic particle-scale statistics, according to assumptions based on the approximation that all collisions are random and binary. Then, the macroscopic constitutive behaviors are based on calculations such as energy and momentum exchanges integrated over the collisional interactions in the system. This adaptation of kinetic theory to gas-like granular flows has been shown successful in modeling these types of flows [13, 22].

Liquid-like granular flows, usually referred to as dense granular flows, are very important in industrial mixing and transport processes as well as certain geophysical flows such as debris flows. Dense granular flows involve some characteristics of both quasi-static deformation and gaseous flows. The rate of application of stress (or strain) is important as is true for gas-like flows. On the other hand, the particles may be in enduring contact with more than one other particle. As dense granular flows show

characteristics of both the quasi-static and gaseous flows, the mechanics of the flow has proven more difficult to model than the two other types of flows. However, the theories developed for the quasi-static and gaseous flows have been adapted to formulate constitutive laws for study of dense granular flows [2, 23, 24, 25]. In this thesis we will focus on dense granular flows.

To this point, there has been no uniformly accepted method for modeling liquid-like, dense granular flows, though several attempts have been made to model the visco-plastic like behavior [23, 26, 16, 27, 25, 28, 29, 30, 31, 32, 33, 8, 34, 35, 36]. Some approaches focus on special features of dense granular systems. Savage and Hutter [34] introduced depth-averaged equations to finite, thin flows, assuming that the flow is incompressible and the spatial variation of the flow takes place on a scale larger than the flow thickness. In their model the granular materials follow a Mohr-Coulomb failure criteria with a basal friction term μ_b at the particle-boundary interface. Later, Savage [23] developed a model for dense granular flows based in part on a model for a frictional plastic continuum with coefficients adjusted to merge smoothly with the kinetic theory for rapid collisional flows. Mills et al. [26] modeled the flowing granular medium as a network of transient solid chains, immersed in sheared viscous fluid. Based on this, they proposed a constitutive law for the stress tensor, which has three components: viscous, frictional, and non-local function of velocity field and material structure (force chains). Aranson and Tsimring [27] also developed theories in which the shear stresses are composed of two parts: the dynamic part proportional to the shear strain, and the strain-independent or static part independent of strain rate. More recently, Pouliquen and colleagues [6, 30, 31] suggested new constitutive relationships based on dimensional arguments and experiments [8] in several types of dense granular flows.

While this research represents a wide range of approaches to modeling dense granular materials, it is generally held [16, 33] that the rheology must depend in some way on a single non-dimensional number known as the inertial number I where:

$$I = \frac{\dot{\gamma} d}{\sqrt{p/\rho}} \tag{1.1}$$

Here, $\dot{\gamma}$ is the shear rate, d, the particle diameter, p, pressure, ρ the particle density, g is the gravitational acceleration constant, This scaling has been associated with the ratio of collisional stress to total stress [34] and also as a ratio of time scales [37], microscopic

time scale (time for particle to fall in a hole of size d under pressure p) and macroscopic time scale $1/\dot{\gamma}$. Based on experiments of dense granular flows over an inclined plane, Pouliquen [6, 37] proposed a relationship between I and μ^*. Unfortunately, there is very little data - experimental or computational - on how mixture behavior depends on particle concentrations from which to derive the relationships between these parameters and concentrations.

Previous studies have utilized experiments, various theoretical frameworks, and numerical simulations to investigate kinematics and dynamics of granular flows. All approaches have some advantages and disadvantages. In experiments, one does not have to assume any material property or physical laws. However, accurately measuring quantities such as stresses in the bulk, is difficult. Most models of granular materials treat them as continua. However, granular materials are inherently discrete and heterogenous. Therefore, its advantageous to use a model framework that accounts for the discrete nature of granular materials and where we can measure all the microscopic scale quantities. The discrete element method (DEM) is an ideal tool for this purpose. Since the DEM method is used as a backbone for the studies in this thesis, some relevant details are briefly reviewed here.

1.1 Discrete Element Method

The discrete element method (DEM, also known as the distinct element method) was first proposed by Cundall and Strack [38]. Though there is a variety of DEM frameworks, they all have a common theme. In the DEM, all particles in a granular media are represented as individual entities. The particles are allowed to interact among each other via physical contact. Real particles deform when they are in contact with other particles or a boundary. In the DEM, this deformation is represented by the overlap distance between the particles (Fig. 1.1). The overlap (deformation) is used to compute the interaction force between the contacting particles. In addition to the overlap, the particle properties and velocities of the particles are required to compute the forces. Our particle-particle and particle-wall contact forces are represented using a non-linear force model based on Hertzian and Mindlin contact theories (e.g.,[39], [40], [41], [42]), a damping component based on the derivation outlined by [42] for spherical particles,

and the Coulomb friction law:

$$F_n = -k_n \delta_n^{3/2} - \zeta_n \delta_n^{1/4} \dot{\delta}_n \tag{1.2a}$$

$$F_t = min\{-k_t \delta_n^{1/2} \delta_t - \zeta_t \delta_n^{1/4} \dot{\delta}_t, \mu F_n\}. \tag{1.2b}$$

F_n and F_t are the magnitude of the contact forces in the directions normal and tangential, respectively, to the plane of contact between two contacting spheres. δ_n and δ_t refer to the effective deformation in the normal and tangential directions, respectively, modeled here, as is common practice, as overlap between contacting spheres. $\dot{\delta}_n = d\delta_n/dt$ and $\dot{\delta}_t = d\delta_t/dt$ are the rates of overlap in the normal and tangential directions respectively. k_n is the normal stiffness coefficient, which is given as $k_n = \frac{4}{3}\sqrt{\frac{d_{\text{eff}}}{2}} E_{\text{eff}}$ based on the Hertzian contact theory. $d_{\text{eff}} = \frac{d_1 d_2}{d_1 + d_2}$ is the effective particle size particle size, E_{eff} is the effective modulus of elasticity ($\frac{1}{E_{\text{eff}}} = \frac{1-\kappa_1^2}{E_1} + \frac{1-\kappa_2^2}{E_2}$), E is the modulus of elasticity of particle, and κ is the Poissons ratio. k_t is the tangential stiffness coefficient, which is given as $k_t = 8\sqrt{\frac{d_{\text{eff}}}{2}} G_{\text{eff}}$ based on the Mindlin contact theory. G_{eff} is the effective shear modulus of the particle, ($\frac{1}{G_{\text{eff}}} = \frac{2(1+\kappa_1)(2-\kappa_1)}{E_1} + \frac{2(1+\kappa_2)(2-\kappa_2)}{E_2}$). ζ_n and ζ_t are the normal and tangential damping factors respectively. The damping factors are functions of the coefficient of restitution (e), the stiffness coefficients, and mass of the particles. For example, the maximum value of ζ_n and is $2\sqrt{\frac{m}{k_n}}$, in which case the particles lose all of their energy after collision ($e = 0$). The minimum value of ζ_n is 0, in which case the particle do not lose any energy after collision ($e = 1$).

At each time step of the simulation, we calculate all forces on each particle (due to weight and particle-particle and/or particle-wall contacts). Based on this, we determine the translational and rotational accelerations of the particles. Then, we calculate particle velocities and displacements at each time step by numerically integrating the translational and rotational accelerations; we use the fourth order Runge-Kutta method for this. The stability and accuracy of the simulations depend on the size of the time step. The time steps should be small enough to resolve all contacts between particles, which is of the order of microseconds in real world. Our time step is small enough to integrate each contact a minimum of 60 times, apparently sufficient given that, previously, it has been suggested that 20 - 100 time steps are necessary for stability and accuracy of the simulations [43].

By using the force model described above, all particles and their material properties may be represented explicitly in the DEM simulations. No assumptions need to be made regarding macroscopic measures of the constitutive behaviors of the bulk granular materials, as in the case of continuum models. The direct representation of the particles makes the DEM a primary choice for modeling heterogeneous granular materials where phenomenology such as segregation arises spontaneously. Another advantage of the DEM is its simplicity that it can be relatively easily modified to simulate different particle interaction laws and different boundary conditions, and it can be coupled with other solvers. In this thesis we used the DEM to model flows of dense granular mixtures and slurries.

The main disadvantage of the DEM is the computational expense in terms of time and memory required to simulate even tens of thousands of particles. To reduce the time and memory required we have implemented efficient contact detection subroutines. Instead of checking possible contacts between all particles, we limit the contact search among near neighbors. To do so, we divide the whole domain into cubic cells that are slightly larger than the largest particle in the granular material. The cell in which a particle is located is identified and this guarantees that the particle can only interact with the particles in the same cell or in the 13 neighboring cells (half of the 26 neighboring cells, to avoid repetition of force calculations).

1.2 Thesis overview

We used this simulation framework to investigate the effect of particle size distribution and the presence of certain amounts of fluids on the behaviors of dense granular flows. Most of the research described in this thesis involves mixtures of particles of different sizes. For part of the work, we consider the effect of fluids on the behavior of dense granular flow. To study this computationally, we further modify the force model to account for hypothesized fluid effects, as described in Chapter 5.

The work described in this thesis is focused on some specific aspects of the flow behaviors of dense granular mixtures. The ability to predict the stresses particulate mixtures exert on their boundaries is important for many critical natural and industrial applications. As mentioned, while existing models for dense granular mixtures suggest

that their rheological properties depend on particle size, the representative size for mixtures is not obvious. Chapters 2 and 3 focus on the effect of average particle size and particle size distribution on average measures of the flow behavior for simply sheared dense granular flows. In Chapter 2 we study the effect of particle size distribution on the pressure (or the normal stress) in the granular mixtures. We perform DEM simulations of sheared dense granular mixtures in a Couette cell (simple shear flows). Based on the results we propose a modification of Bagnold's model in part inspired by recent developments in research on jammed granular materials, that is, granular materials at the transition between the liquid-like and solid-like states.

In Chapter 3 we use the same simulation set up as in Chapter 2 to study frictional constitutive laws and microscopic time scales in sheared granular flows. In doing so, we find that the variation of the rheology with the particle size distribution depends on the boundary conditions. For example, under constant pressure conditions the effective friction coefficient μ^* (the ratio between shear and pressure stresses) increases mildly with the average particle size. On the other hand, under constant volume conditions, μ^* has a nonmonotonic dependence on the average particle size that is related to the proximity of the system solid fraction to the maximum packing fraction. Somewhat surprisingly, then, μ^* scales with a dimensionless shear rate (a generalized inertial number) in the same way for either boundary condition. In other words, we find that the particle size distribution does not change the frictional constitutive laws except in terms of the average particle size. We find that, for our system of relatively hard spheres, these relationships are governed largely by the ratio between average contact duration and mean-free-path times, also independent of boundary conditions. We also find that the microscopic time scales (the mean collision duration of two particles and the time a particle spends without touching another particle) can be used to determine the regime of the flow.

Chapters 4 and 5 focus on certain aspects of dense granular flows relevant to geophysical granular flows, specifically, those of debris flows, massive flows of particles and fluids that occur in nature. For this, we study shallow dense granular flows in rotating drums using DEM simulations and large scale experiments with collaborators in the Earth and Planetary Sciences Department at the University of California at Berkeley (UC-Berkeley). In Chapter 4 we first determine the relevance of relatively small scale

DEM studies to debris flows by comparing our results to experimental debris flow studies of our collaborators at UC-Berkeley. We find that our simulations reproduce experimentally measured segregation, boundary pressures, and longitudinal surface profiles. We then study the effect of particle size distribution and segregation of particles on the forces exerted on the drum bed in the context of the problem of bedrock incision associated with debris flows. We find that local time-averaged boundary pressures in thin flows are essentially the normal component of the weight of the flow, independent of particle size distribution. The statistics of local instantaneous boundary forces, however, scale with mass-averaged local particle size in similar mixtures. Individual particle-bed impacts rather than multiple-particle collisions dominate the largest particle-bed forces which vary as the grain size squared and the 1.2 power of particle-bed impact velocity as predicted from the DEM collisional mechanics model, in support of certain details of a recently proposed bedrock incision model. We describe how these new insights can be used for improved models of bedrock incision associated with debris flows.

In Chapter 5 we consider the possible modifications some of these models to more realistic debris flows, particularly those that involve some amount of interstitial liquid. The presence of a fluid can introduce an apparent cohesivity between particles, provide lubrication allowing particles to more easily slide past one another, damp relative particle movement, and can be the source of anomalous effects associated with pore pressure that is greater than the hydrostatic pressure. Modeling granular flows taking into account these effects is somewhat more complicated than modeling dry particles alone, and they involve longer-range interactions between particles. In Chapter 5 we present two methods for doing so, one for low moisture content and one for saturated granular flow. We investigate them for their effectiveness in modeling the effect of the presence of an interstitial fluid in debris flows using comparisons between some experimental results and some results from simulations employing these methods. In both cases, we use similar boundary conditions to those in Chapter 4, those of thin granular flows (slurries) in a rotating drum. We show that the results from the proposed model are qualitatively similar to results from large scale experiments.

The results in this thesis provide a foundation for modeling and predicting the wide range of complex behaviors of granular mixtures that can arise in natural and industrial granular materials associated with mixtures of different sized particles and interstitial

fluids. Chapter 6 concludes with a summary of the research performed and suggested future directions for building on the foundations provided in this thesis.

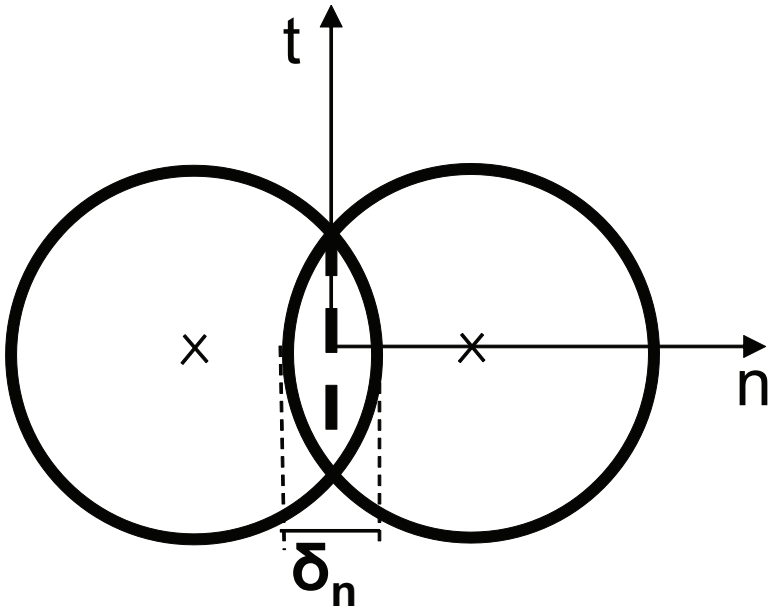

Figure 1.1: Illustration of the interaction of two particles in a DEM model. During each collision the associated deformation is represented by a normal overlap (δ_n) between the two particles. The plane of contact is assumed to be flat and perpendicular to the line joining the centers of the two particles. n is the axis perpendicular (normal) to the contact plane and t is the axis parallel (tangential) to the contact plane.

Chapter 2

Rheology of dense granular materials: stresses at the boundary

2.1 Introduction

The ability to predict the stresses particulate mixtures exert on their boundaries is important for many critical natural and industrial applications. For example, predicting boundary stresses due to bouldery debris flows – massive flows of rocks and boulders – is important for understanding landscape morphology as well as for hazard mitigation [2, 44, 45, 46]. Additionally, wear associated with boundary stresses can considerably shorten the life of industrial machinery [47]. However, a predictive model for stresses due to dense granular mixtures is elusive.

Several formulations have been proposed to predict stresses due to granular flows [11, 13, 48, 9, 49, 50]. These formulation involve assumptions of particle interactions and correlations that are specific to a certain type of granular flow. These types of formulations are are mostly based on either very energetic granular regime [11, 13, 49] or quasi-static regime [9, 51, 52]. Some of these formulations will be discussed briefly in this section.

As briefly discussed in Chapter 1, kinetic theory is used to model energetic, gas-like granular flows. In kinetic theory several forms of constitutive laws for predicting the stresses have been proposed based on assumptions about the statistics of particle motion including a radial distribution function [13, 53, 54] and assumptions about the interparticle collisions. Among other things, kinetic theory has shown that granular temperature (i.e. the sum of velocity variances) plays an important role in the dynamics of gas-like granular flows [13, 53, 54]. Though the derivation of these constitutive laws is very complex, some of the outcomes may be expressed in a simple form. For example, one of the simplest form of the pressure derived from the kinetic theory may be given as

$$p = 2\rho G T \tag{2.1}$$

where ρ is the density of the particles, $G = \nu g_o$, g_o is the radial distribution function, ν is the solid volume fraction, and T is the granular temperature, one half of the sum of the velocity variances in all directions. g_o describes how ν varies as a function of radial distance from a given particle. Different forms of the radial distribution function (g_o) have been proposed [13, 53, 54, 55, 48]. One example of the radial distribution function for identical spheres was determined numerically by [13]

$$g_o(\nu) = \frac{1}{1-\nu} + \frac{3\nu}{2(1-\nu)^2} + \frac{\nu^2}{2(1-\nu)^3} \tag{2.2}$$

Kinetic theory of granular gases was originally derived for low values of ν assuming all contacts are binary collisions and all collisions are uncorrelated with previous collisions (in effect, a "molecular chaos" assumption). Therefore, kinetic theory is ideal for sparse flows of hard particles, which have coefficient of restitution e close to unity. As the solid volume fraction increases and stiffness of the particles reduces, multiple particle contacts prevail. In such cases the kinetic theory may fail to capture the important characteristics of the flow [22]. However, kinetic theory indicates the important relationship between the solid volume fraction ν and the stresses.

For slowly sheared granular flows at the limits of high solid volume fractions the particle-particle interactions are dominated by enduring contact between the particles. Savage [9] proposed that the enduring contacts have two major effects on the flow. First, the granular temperature of individual particles plays a limited role in the magnitude

of the stresses. Second, the inter-particle sliding is more important than pure particle collisions in driving the constitutive behavior. Based on these assumptions, Savage [9] developed a constitutive law to predict the stress tensor in slowly sheared granular flows. In Savage's model the pressure (normal stress) is a function of the velocity gradient and the volume fraction gradient [51, 52].

$$\sigma = \sigma(\nu_o, \nu, \nabla\nu, \mathbf{D}) \tag{2.3}$$

where ν_o is a reference volume fraction for ν, $\nabla\nu$ is the gradient of ν and $\mathbf{D}$ is the rate of deformation $\mathbf{D} = \frac{1}{2}\left(\nabla\mathbf{u} + (\nabla\mathbf{u})^T\right)$, $\mathbf{u}$ is the local velocity. The equation for σ includes several physical parameters as well, such as cohesive forces and the coefficient of friction.

Recently, significant advances have been made in understanding pressure and structure associated with quasi-static deformation of monosized granular materials above the jamming transition, i.e., systems where the solids fraction ν is greater than the minimal solids fraction required for mechanical stability ν_c [56, 57, 58, 59, 60, 20]. For example, simulations (e.g., [56]) and experiments [58] have shown $p \sim (\nu - \nu_c)^\beta$ where β depends on the contact interaction potential between particles. Their results further suggest a power law relationship between the number of contacts per particle, or coordination number, Z, and p.

A formulation proposed by Bagnold in the 1950's [11] has held for monodispersed systems in a general sense, far beyond the regime of rapid collisional flows for which it was derived, provided the particles are sufficiently hard [29], depth of flow is sufficient deep [61, 62] and the interstitial fluids are not too viscous [63]. Based on considerations of momentum transfer via collisions in sheared flows, Bagnold proposed the average pressure p scales with both the particle size d and the shear rate $\dot{\gamma}$ squared: (see Appendix A)

$$p \sim f(\xi)\rho d^2\dot{\gamma}^2 \tag{2.4}$$

where ρ is the material density of the particles, d is the particle size, $\dot{\gamma}$ is the shear rate, and $f(\xi)$ is a functional form of the structure of the granular materials.

The relationship between p and $\dot{\gamma}$ in Equation 2.4 can be explained based on dimensional analysis [24]. In granular flows parameters such as $\dot{\gamma}$, the contact duration t_c,

and the fluid viscosity (in cases where interstitial fluids are present) have dimensional units which contain time. In the limits of hard particles (negligible contact duration [29]) and low fluid viscosity (or no fluid) [11, 63], the only parameter with dimensions of time is $\dot{\gamma}$. Therefore, pressure (which has dimensions of $\frac{Mass}{Length \times Time^2}$) must scale with the square of $\dot{\gamma}$. On the other hand, for granular materials where the viscosity of the interstitial fluid is higher [63], the stiffness of particles is lower [29, 64, 28], and the interaction force between particles include cohesive forces [65] the pressure has been shown to scale with $\dot{\gamma}^{\alpha}$, where α ranges between one and two.

For his system, Bagnold proposed $f(\xi) = \lambda^2$ where:

$$\lambda = d/s, \tag{2.5}$$

is the "linear concentration"; here, s is the mean distance between particles (e.g., Fig. 2.1 (a)). Bagnold demonstrated that for certain particle arrangements of uniform spheres $\lambda = ((\nu_{max}/\nu)^{1/3} - 1)^{-1}$ where ν_{max} the maximum solids fraction, ~ 0.74 for uniform spheres (see Appendix A). This estimation based on ν and ν_{max} is feasible for a practical measure of linear concentration, though only for monosized spherical particles. Slightly different forms of the structure of the granular materials, $f(\xi)$ (Equation 2.5) have been used elsewhere. For example, da Cruz et al. [33] showed $p \sim (\nu_{max} - \nu)^{-2} d^2 \dot{\gamma}^2$ for DEM simulations of 2-dimensional simple sheared dense granular flows.

Bagnold assumed a single particle size d is an appropriate measure of length scale in granular flows. For dense granular flows, others have argued that length scale depends on the length associated with correlated motions [66, 54]. The length of correlated motions can be estimated by directly measuring the cross-correlation of the velocities of individual particles [32, 67] or from some other measures of the system scale behavior, such as "stopping height". The "stopping height" h_{stop} was first reported in extensive experiments of granular flows over an inclined plane by Pouliquen [6]. Pouliquen [6] suggested that material starts to flow when the angle of inclination is above minimum inclination θ_{min} and indefinitely accelerates when the angle of inclination greater than maximum inclination θ_{max}. The flow attains a steady state for any angle θ between θ_{min} and θ_{max}. However, the flow stops at low depth of flow h_{stop}, even if the inclination is above θ_{min} but below θ_{max}. Therefore, h_{stop} can be considered as the critical length of correlated motions for gravity-driven granular flows. Based on this finding, Ertas

and Halsey [66] hypothesized that the appropriate length scale is the size of a cluster of particles formed by chains of contacting particles. A cluster moves as a single unit with a specific translational and rotational velocity. Similarly, some have suggested modification to the length scale used in kinetic theory to extend it to denser granular flows [54]. In this framework, a new length scale is defined instead of taking the particle size as the length scale. This length scale can be measure as the size of the cluster [54] or a measure of the distance in which a significant correlation of particle velocities exists [32, 67].

All of these realizations of Eq. 2.4 contain explicit and implicit dependencies on particle size distribution. For a mixture of two (or more) different sized particles, it is not obvious what the representative size should be, nor what one might use for ν_{max}. Further, there is not a clear unique length scale over which an average s should be calculated for such a disordered system that arises in a mixture of different sized particles (e.g., Fig. 2.1(b)). These results suggest an alternative approach for continuously sheared mixtures where information regarding how the particle size distribution affects packing may be contained in measures of the structures such as Z.

Kinetic theory predictions of stresses in granular mixtures

Some researchers have used the kinetic theory to investigate the effect of particle size distribution on the stresses for granular flows of low solid volume fractions. For example, Alam and Luding [22] used the kinetic theory to study the rheology of granular mixture of different size, mass and density. They compared the theoretical predictions with event driven simulations and concluded the kinetic theory fails above $\nu_{2D} = 0.75$ for 2D systems (which is equivalent to $\nu = 0.48$ for 3D systems). Fig. 2.2 shows the prediction of pressure for different values of f_L for binary mixture of particles with different sizes. In this figure the pressure is normalized by the inertial stresses ($\rho\dot{\gamma}^2\overline{d^2}$) to compute the nondimensional pressure p^*. A Similar approach was used by Karion and Hunt [68].

We probe the dependence of boundary pressure associated with dense sheared granular mixtures on their particle size distributions using simulations of binary mixtures of different sized particles. As did Alam and Luding [22] for sparser systems, we find there is a nonmonotonic dependence of p on the average particle size $\overline{d}$. We demonstrate this can be modeled using a relationship between effective packing efficiency and Z through a formulation derived for the packing for monosized systems of spherical particles near

the jammed state [60, 20].

2.2 Simulation set up

For our simulations we use a soft sphere Discrete Element Method (DEM) [38]. Particle-particle and particle-wall contact forces are represented using a non-linear force model in both the normal direction F_n (the direction connecting the centers of two contacting spheres) and the tangential direction F_t (perpendicular to the normal direction) according to Hertzian and Mindlin contact theories and some numerical parametrization according to Tsuji et al. [42]. The details of DEM procedure are shown in Chapter 1. For most of the results described here, all simulated particles have material properties similar to quartz. We discuss similarities and differences using softer particle at the end of this Chapter.

We primarily simulate binary mixtures of 10 mm and 20 mm particles (with a polydispersity of 10% in the diameter of each component to inhibit crystallization). Sample parameters are given in Table 2.2. In our simulations we vary the fraction of each component and we refer a given mixture by the mass fraction of the larger particle f_L. The particles are sheared in a plane Couette cell (as in Fig. 2.3) in the absence of gravity similar to the simulations performed by, for example, Campbell and Brennen [12] and daCruz et al. [33]. In his experiments, in order to eliminate the effect gravity Bagnold used neutrally buoyant particles (density matched experiments)[11]. In our simulations, two parallel walls contain the particles in the y-direction, one of which moves with constant velocity U_w as illustrated in Fig. 2.3(a). The boundaries are periodic in the other two directions. Two types of boundary conditions are used for the Couette flow simulations: one set involving constant volume and the other involving constant pressure simulations. In the constant volume simulations the height of the Couette cell is fixed. For most of the constant volume simulations the height of the Couette cell $H = 240$ mm ($H = 24d_s$, where d_s is the diameter of the smaller particle). In the constant pressure simulations the height of the Couette cell is allowed to change in response to the interparticle forces on one side, while a constant pressure is effectively applied on the other side. These, too, were performed while the bottom wall moved with a constant velocity U_w. Since the height varied less than 10% over the course

Table 2.1: Material properties of particles primarily used in the the simulations.

property	value
Modulus of Elasticity (E)	29 GPa
Material density (ρ)	2650 kg/m^3
Coefficient of friction (μ)	0.5
Poissons ratio	0.15

Table 2.2: Coefficients of the force model for each type of particle-particle interaction. The sizes of the two particles involved in each potential interaction are indicated. In the simulations, there is a slightly wider variability of the particle coefficients as there is some spread of particle size around 10 and 20 mm.

parameter	10 & 10 mm	10 & 20 mm	20 & 20 mm
k_n (N/m$^{3/2}$)	0.99×10^9	1.14×10^9	1.41×10^9
k_t (N/m$^{3/2}$)	1.36×10^9	1.57×10^9	1.93×10^9
ζ_n (Ns/m$^{5/4}$)	8.20×10^1	1.17×10^2	2.76×10^2
ζ_t (Ns/m$^{5/4}$)	9.62×10^1	1.38×10^2	3.24×10^2

of each experiment, we base our calculations on the assumption that the shear rate is essentially constant. The length of Couette cell (in the streamwise direction) $L = 288$ mm and breadth of the Couette cell $B = 150$ mm. To minimize particle slipping at the top and bottom boundaries, we affix 10 mm particles to the walls in a random array. These "glued" particles have the same material properties as the flowing particles (see Table 2.2 and 2.2). Results appear independent of the size of these particles provided they are large enough to provide sufficient roughness and arranged to prevent small particles from being preferentially trapped among them.

The Couette cell geometry has the advantage of simplicity compared to other common flow configurations used to study granular flows, such as inclined plane and rotating drum. Figures 2.3 (b)-(d) provide some examples of the flow behaviors for a constant volume simulation for a mixture of 10mm and 20mm particles of 75% and 25% by mass respectively. The total mass of the granular material is $\sim 15.6kg$, resulting in a solid fraction of $\sim 56.8\%$. The relative velocity of the two parallel walls is $830mm/s$. Under these conditions the velocity profile is linear (Fig. 2.3(b)), in other words the shear rate $\dot{\gamma}$

is uniform throughout the flow. Segregation is also minimized (Figs. 2.3(c)-(d)). Initial segregation of large particles away from the walls is minimal and quickly stabilizes, as illustrated by the temporal plot of the fraction of large particles f_L in the middle section (f_{LM}) shown in Fig. 2.3(d). f_{LM} is the fraction of large particles in the region bounded by the two dashed lines in Fig. 2.3(c). There is no segregation in the streamwise direction. The limited segregation and uniform linear velocity profile provide boundary conditions that effectively isolate the effect of particle size distribution on the boundary pressure.

2.3 Results

Boundary pressures p are obtained by summing the $y-$components of all forces on the particles affixed to the boundary and dividing the sum by the area of the boundary. Fig. 2.4 (a) shows p as a function of time t for $f_L = 0.25$. p is not constant, but the average value stabilizes after approximately 10s. The data for the shear stress at the boundary Fig. 2.4 (b) shows similar behavior. For the average results reported below, we consider the data for several seconds after the statistical stabilization is reached ($t \geq 10s$). The probability distribution function of the boundary pressures after steady state is reached may be fit well by a two parameter lognormal distribution function [69] or gamma distribution function. The latter provides the best fit in most cases and is shown in Figs. 2.5 and 2.6. The gamma distribution function is given by:

$$f(x) = \frac{x^{a-1} e^{\frac{-x}{b}}}{b^a \Gamma(a)} \tag{2.6}$$

where a is the shape parameter and b is the scale parameter. $\Gamma(a)$ is the gamma function of a. We compare results from several computational experiments where the shear rate $\dot{\gamma}$ and f_L are varied from one experiment to the next: $\dot{\gamma} = 3.44s^{-1}$ to $11.44s^{-1}$, and f_L=0 to 1. The average particle size for each mixture $\overline{d}$ is approximately proportional to f_L: $\overline{d} \sim 10(1 + f_L)$ mm. The relationship is only approximate because of the polydispersity of each of the particle species. The fitted parameters vary with the f_L. Fig. 2.7 shows the variation of the fitting parameters with f_L for $\nu \sim 56.8\%$ simulations. The variation indicates that the stress distribution at the boundary differs for different types of mixtures. However, in all cases the fits indicate that the average is well behaved

and we primarily report the average results.

Figure 2.8 shows $\overline{p}$ for several values of ν from 20% to 56.8% for $f_L = 0.0$ and 0.50. For both values of f_L, $\overline{p}$ increases moderately with ν at lower values of ν. Up to $\nu = 50$ % there is not a significant difference between $\overline{p}$ measured for $f_L = 0.0$ and 0.50. The value of $\overline{p}$ becomes different for these two values of f_L for $\nu > 50\%$. At even higher values of ν, $\overline{p}$ diverges. We focus on the effect of particle size distribution for granular flows at higher value of $\nu = 56.8\%$. This value of ν can be classified as dense granular flow, slightly higher than what is usually referred to as random loose packing for uniform spherical particles ($\nu = 55\%$).

Figure 2.9(a) shows p as a function of $\dot{\gamma}$ for different values of f_L. As in Equation 2.4, for any particular mixture $p \sim \dot{\gamma}^2$. However, for any particular value of the shear rate, the pressure does not depend monotonically on average particle size. As f_L increases, the normal stress first decreases then increases. This is made particularly clear by plotting p vs. f_L for one particular shear rate ($\dot{\gamma} = 3.44s^{-1}$) in Fig. 2.9(b). The variation of shear stress τ with f_L is similar. We focus here on developing a model for the variation of p with particle size distribution and comment on the extension to τ and $\mu^* = \tau/p$ in the summary of this chapter and in Chapter 3.

We consider results for monosized granular materials near the jammed state suggesting a power law relationship between p and Z [56, 59]. In our mixtures, $Z(y)$ is sensitive to minor variations in particle concentration and segregation (Fig. 2.9(c)), so we consider the value averaged across the cell Z and plot it as a function of f_L along with p in Fig. 2.9(b). Both Z and p follow the same trend as f_L is varied. However, when we combine these data in a parametric plot in Fig. 2.9(d), in contrast with monosized systems near the jammed state [56, 59], there is no simple relationship between p and Z for steadily sheared mixtures.

We propose that the differences between the dependence of p on Z in monosized systems and in our mixture are related to the variability of the potential packing efficiency from one mixture to the next under otherwise identical conditions. We investigate this hypothesis by considering the variation in ν with f_L under analogous constant pressure conditions. As in the constant volume simulations, steady state conditions are reached fairly early in the simulation (after $\sim$ 10s) and the statistics are well-behaved [69]. In Fig. 2.10(a) we plot the height averaged over the second 10s of each simulation, for

several values of f_L. The trend is similar to that of p vs. f_L (Fig. 2.9(b)): for the same applied pressure, ν is higher for the mixtures for which $f_L \approx 0.5$ compared to the mixtures for which $f_L \approx 0$ or $f_L \approx 1$. This indicates that while the different constant volume simulations have the same porosity, the free space effectively *available* to the particles in the mixtures for which $f_L \approx 0.5$ is greater than those for which $f_L \approx 0$ or $f_L \approx 1$. We hypothesize that the variability of this effective free space gives rise to a variability of what Bagnold referred to as a *dispersive pressure* [11] - the pressure resulting from interparticle collisions.

2.4 Discussion

To quantitatively model the variation of available free space (and ultimately p) with Z, we evoke concepts associated with free volume per particle W from quasi-static mono-sized systems [60, 20]. By experimentally measuring Voronoi volumes (V_v) and Z associated with each particle (volume V_p) in a static granular system, Aste et al. [60] showed that $W = V_v - V_p$ scales inversely with Z. Analytical results of Song et al. [20] show that $W = 2\sqrt{3}V_p/Z$. For our constant volume simulations, ν is invariant from one experiment to the next, so for the whole system, $W = (1-\nu)HLB/N$ where N is the total number of particles. However, the *available* free space is somewhat less than that; we define $W_{\text{eff}} \equiv (\nu_{max} - \nu)HLB/N$. For a computationally accessible measure of W_{eff}, we consider the analytical results of Song et al. [20] and propose a similar relationship between W_{eff} and Z:

$$W_{\text{eff}}(Z)/V_p = k/Z. \tag{2.7}$$

where k is an unknown constant, but must satisfy $k < 2\sqrt{3}$ since $W_{\text{eff}} < W$. We note that this model is limited to continuously unjammed sheared system, so that $\nu < \nu_c$, $W_{\text{eff}} > 0$, and Z remains bounded. To relate the above discussion to p, we return to Bagnold's λ (Equation 2.5). Since a direct measure of an average s for our mixtures is ambiguous, we define an effective average space between particles s_{eff} according to W_{eff}. As we sketch in Fig. 2.1(a), we relate W_{eff} to an effective spacing between particles geometrically via spherical shells, and s_{eff} is twice the thickness of these shells:

$$W_{\text{eff}}(z)/V_p = \pi/6\left[(d + s_{\text{eff}})^3 - d^3\right]/(\pi d^3/6) \tag{2.8}$$

We note that for these definitions, s_{eff} and W_{eff} are nonzero at random loose packing. Equating the righthand sides of Equations 2.7 and 2.8 and solving for $\lambda_Z \equiv d/s_{\text{eff}}$, we find:

$$\lambda_Z = \left[(k/Z+1)^{1/3} - 1\right]^{-1} \tag{2.9}$$

With this, we propose a modified version of Bagnold's model for pressure (Equation 2.4) associated with dense sheared mixtures of different sized particles:

$$p \sim \rho \lambda_Z^2 \overline{d}^2 \dot{\gamma}^2. \tag{2.10}$$

where λ_Z is given by Equation 2.9. Combining Equations 2.9 and 2.10 we consider now a relationship between a dimensionless p and Z:

$$p^* = p/(\rho \overline{d}^2 \dot{\gamma}^2) = K\left[(k/Z+1)^{1/3} - 1\right]^{-2} \tag{2.11}$$

where K is a proportionality constant. We perform a 2-parameter nonlinear least squares fit to find $k = 1.2$ and $K = 10.1$. We then plot p^* vs. λ_Z^2 in Fig. 2.10(b) for the data from Fig. 2.9(b) and analogous results from other size distributions detailed in the caption. The collapse of the data suggest that Equations 2.9 and 2.10 provide an extension to Bagnold's classic relationship for pressures [11] associated with dense flowing granular mixtures. Preliminary results for somewhat higher and lower values of ν and p indicate a limit for the applicability of Equation 2.10 even for relatively hard particles. For higher values of p and ν, p continues to increase with little increase in Z as indicated by the dashed line in Fig. 2.10 (b) possibly as the system is approaching a jammed state.

Fig. 2.11 shows the relationship between λ_z and p^* for the constant volume (CV) and constant pressure (CP) simulations. For the CV simulations ν is varied between 20% and 56.8 %. For the CV simulations it is difficult to achieve higher solid fraction volume because the particles may get jammed and require very large force to move past other particles. For such high interparticle forces, the overlap between the particles becomes unrealistically high, which violates the basic principles of the DEM. For the range of values of ν we have tested p varies from about 0.9 Pa for f_L=0.50 and ν = 20% to about 2800 Pa for $f_L = 1.0$ and $\nu = 56.8$ %. For these CV simulation the functional dependence of p^* on λ_z is the same as results shown in Fig. 2.9(b). For the CP simulations the applied pressure (p_{app}) is varied progressively from 0.089 to

$550.0kPa$. For the CP simulations the relationship between p^* and λ_z at lower values of applied pressure is the same as that of the CV simulation. However at higher applied pressure λ_z approaches a constant value.

The results for τ are similar to the results for p described above as one might expect from Bagnold's model which predicts p scales linearly with τ. Interestingly, the power law dependence of τ on λ_Z is slightly different, and there is a dependence of $\mu^* = \tau/p$ on f_L that depends on the boundary conditions as we discuss in detail in Chapter 3 [70].

Considering analogies with Bagnold's model, one may also consider whether or not λ_Z is directly related to $\overline{d}$ and s averaged over a length scale that captures the local structure, such as a cluster size or a correlation length [66, 67]. Alternatively, λ_Z may effectively capture such a measure of structure somewhat independent of $\overline{d}$. For our simulations we measure the size of cluster as the maximum distance $(l * d_s)$ as described by Ertas and Halsey [66] between any two particles that are members of a cluster, which is formed by chains of contacting particles. Fig. 2.12 shows the measured length l for constant volume simulations at $\nu = 56.8\%$. As in the case of Z and $\overline{p}$, l first decreases and then increases as f_L is increased. In addition Fig. 2.12(b) shows that pressure is related to the cluster size: pressure increases as the cluster size increases.

In addition to providing an extension to Bagnold's stress scaling for mixtures, these results provide some links between some established behaviors of monosized granular materials near the jammed state and dense flowing granular mixtures. Given this, it is interesting to consider the level and limits of their applicability to granular mixtures whose particle and mixture properties vary significantly from those we used for these results. For example, preliminary investigations into the dependence of these results on particle hardness show quantitative differences only for somewhat softer particles. Specifically, for particles with an elastic coefficient up to four orders of magnitude smaller than for the results shown here, $p \sim \lambda_Z^2 \rho \overline{\mathrm{d}}^2$. Still, over this range Z increases with decreasing hardness (e.g., Ref. [28]) while W_{eff} does not, so k must depend inversely on particle hardness. In contrast, for systems of significantly softer particles, the rheology changes qualitatively, and p is no longer proportional to $\dot{\gamma}^2$ [28]. Nevertheless, for a constant value of $\dot{\gamma}$ we find a similar non-monotonic relationship exists between p, Z, and $\overline{d}$. Z increases almost linearly with $\dot{\gamma}$, even for hard spherical particles (Fig. 2.13).

Therefore, the dependence of Z on $\dot{\gamma}$ should be studied to determine a functional form for the fitting parameter k based on system parameters. While a similar framework may apply to these systems, the full effect of varying particle hardness and indeed other particle properties such as material friction coefficient (e.g., Ref. [71]) is not yet clear.

In this chapter we have shown the dependence of p, which is macroscopic variable, on microscopic measures of structures in granular media, Z and l. However, measuring these microscopic variables in real experiments is very challenging ([60]) and in most cases impossible. Therefore, it is very important to be able to predict the microscopic variables from easily measurable quantities of the granular flow, such as particle size distribution and volume fraction. Geometric considerations likely further constrain the applicability for binary mixtures with extreme particle size differences when the size of the smaller particles approach the size of the pore spaces among larger particles ($d_S/d_L \lesssim (2/\sqrt{3} - 1)$).

For somewhat lower values of ν, the pressure appears less sensitive to Z possibly as the system is approaching a gaseous state, though segregation and other inhomogeneities increase at lower solids fractions making systematic investigation of this more difficult. More work is needed to flush out these transitions and to determine their dependencies on particle property and shear rate. As a result of the work investigating these details, more of the physics of transitions among different phases of granular liquids and solids may become apparent.

We thank William E. Dietrich, Leslie Hsu, Deveraj van der Meer, Robert Behringer, Michel Louge, and Vaughan Voller for helpful discussions.

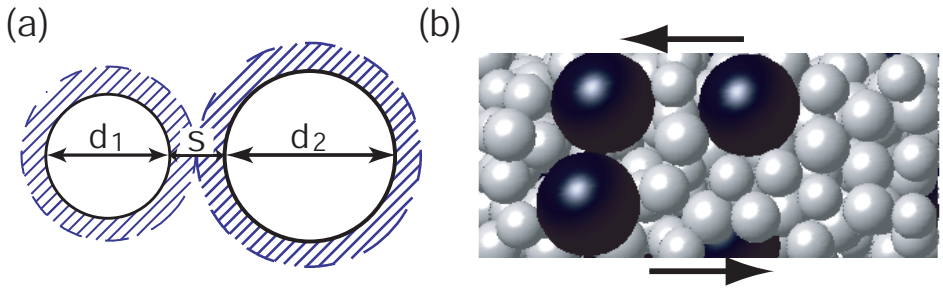

Figure 2.1: (a) Sketch of s and d from Equation 2.5. Hatched region indicates an effective free volume described in the text. (b) Image from a small section of the simulated sheared particles described in the text.

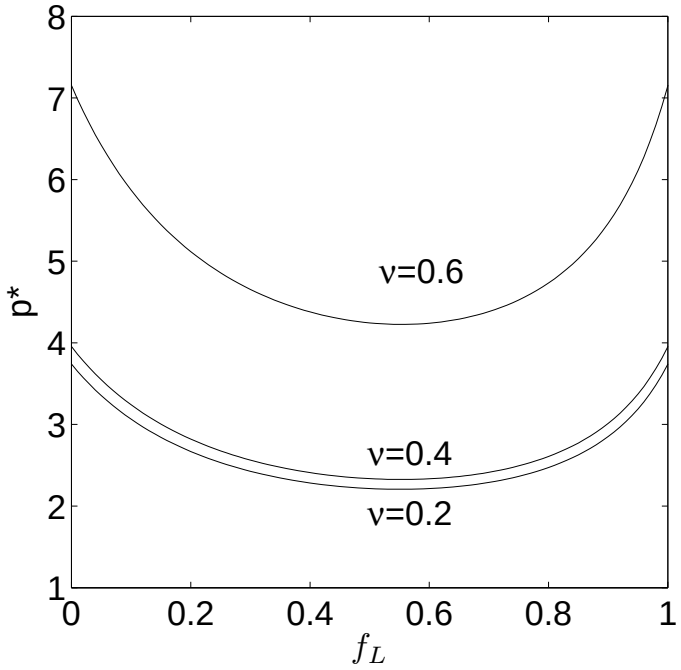

Figure 2.2: Dimensionless pressure prediction based on kinetic theory as in Alam and Luding (2003) for different values of fraction of larger particles by mass f_L

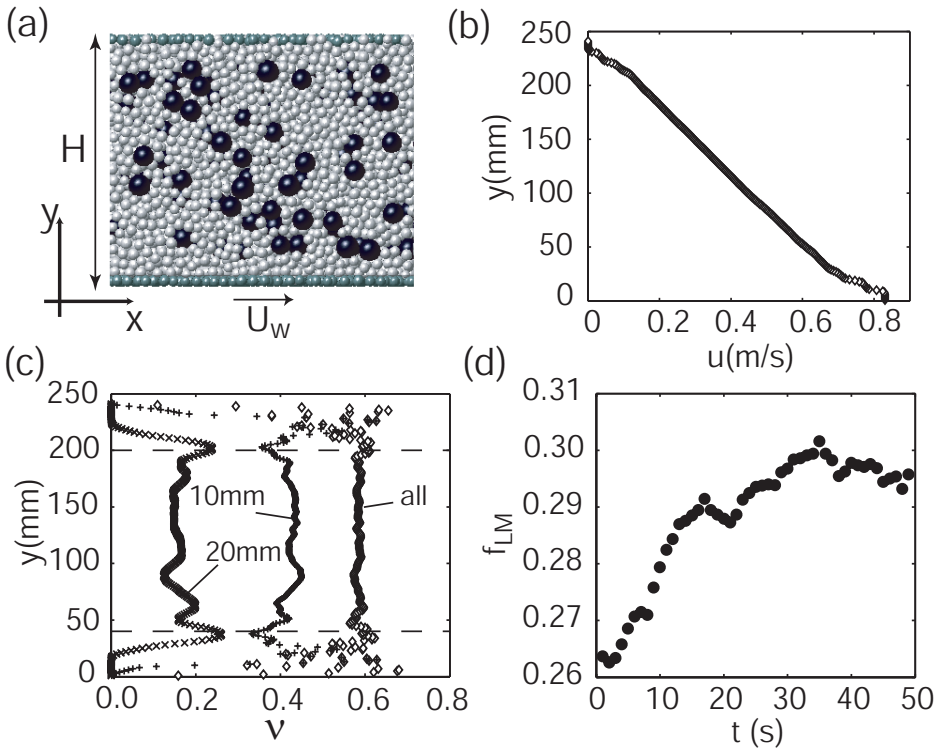

Figure 2.3: (a) Image from one time step in a parallel Couette cell simulation described in the text for $f_L = 0.25$. U_W =830mm/s ($\dot{\gamma} = 3.44s^{-1}$) (b)-(d) Some kinematics for the mixture shown in (a). (b) Streamwise velocity profile. (c) Solid volume fraction profiles for each component of the system and the mixture. (d) The fraction of large particles in the central region, i.e., $f_{LM} = \nu_{20mm}/\nu_{mix}$ for the region within the dashed lines shown in (c) ($y = [40, 200]$mm).

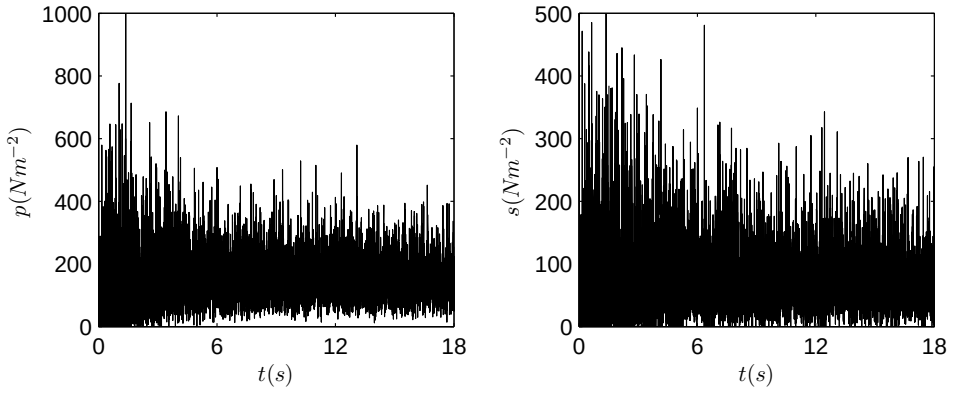

Figure 2.4: Time series of the normal and shear stress measured at the boundary. The stresses are not constant throughout the simulation, but fluctuate continuously as the granular material is sheared. This plots are for f_L=0.25, $\dot{\gamma} = 3.44s^{-1}$.

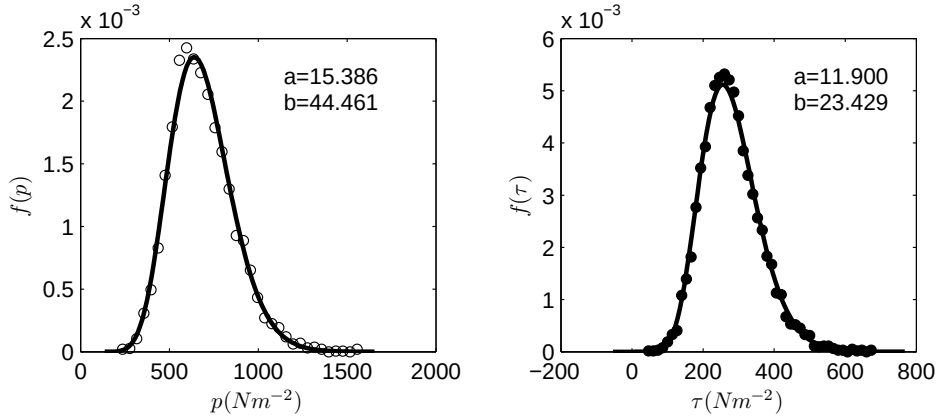

Figure 2.5: Probability distribution function (pdf) for the pressure and shear stress at the boundary from a constant volume Couette cell flow for f_L=0, $\dot{\gamma} = 3.44s^{-1}$. The solid line is a gamma distribution function fitted to the data. a is the shape parameter and b is the scale parameter.

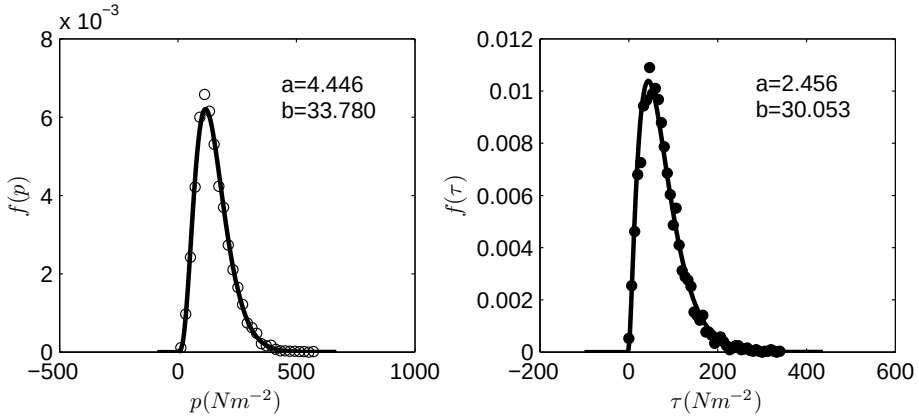

Figure 2.6: Probability distribution function (pdf) for the normal stress and shear stress at the boundary from a constant volume Couette cell flow for f_L=0.25, $\dot{\gamma} = 3.44s^{-1}$. The solid line is gamma distribution function fitted to the data. a is the shape parameter and b is the scale parameter.

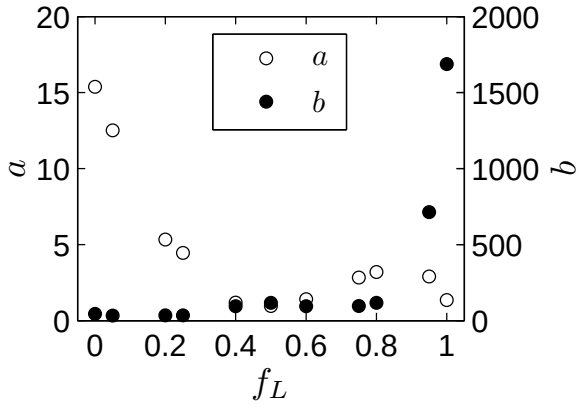

Figure 2.7: The shape parameter, a, and the scale parameter, b, of gamma distribution function fitted to the pressure distribution for several values of f_L for constant volume Couette cell simulations ($\dot{\gamma} = 3.44s^{-1}$).

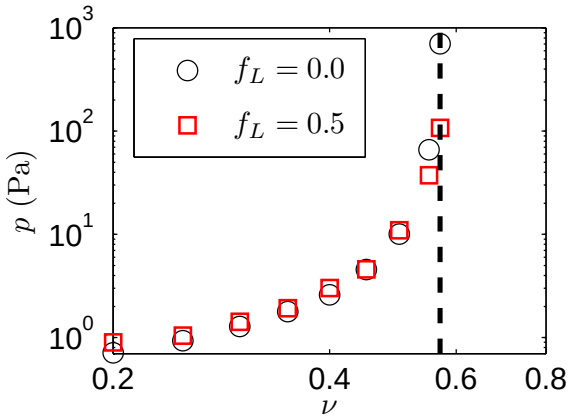

Figure 2.8: Pressure for $f_L = 0.0$ and 0.5 mixtures as a function of solid volume fraction.

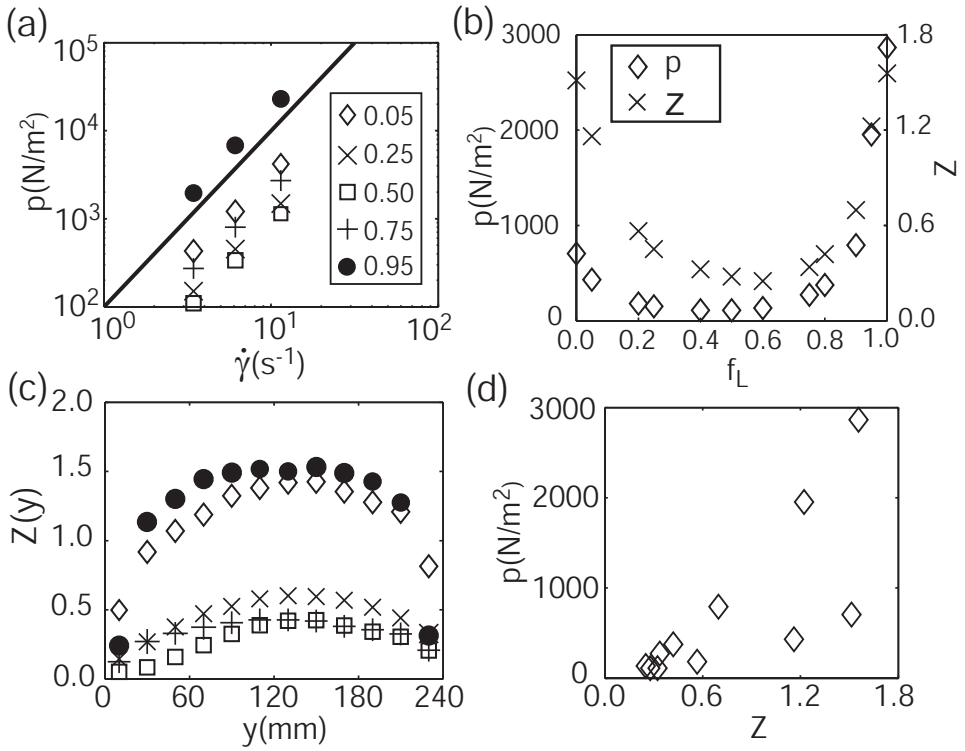

Figure 2.9: (a) p vs. $\dot{\gamma}$ for several fractions of large particles as indicated in the legend. The solid line represents a slope of two. (b) p and Z vs. f_L for $\dot{\gamma} = 3.44s^{-1}$. (c) Profile of $Z(y)$ for several fractions of large particles (symbols indicated in (a)). A minor asymmetry persists associated with the initial configuration of the particles. (d) Parametric plot of p as a function of Z for the results shown in (b).

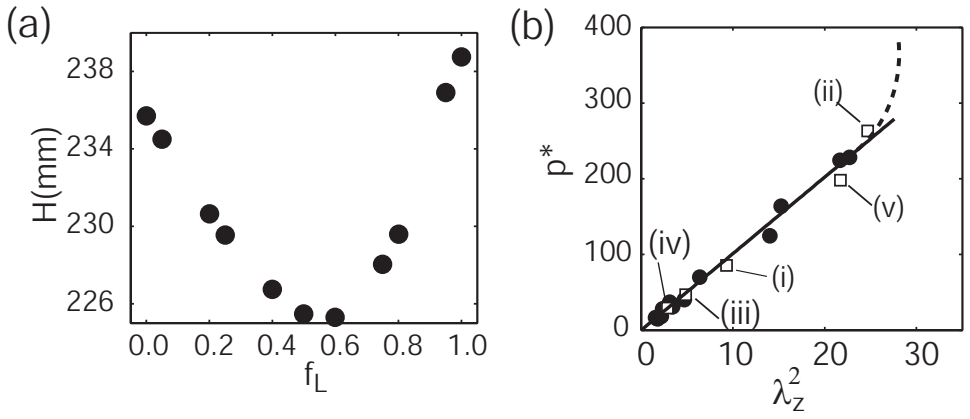

Figure 2.10: (a) H vs. f_L for several values of f_L, in constant pressure simulations where $p_{app} = 17.2kPa$, and $U_w = 830mm/s$ ($\dot{\gamma} \sim 3.44mm/s$). (b) p^* vs. λ_Z^2 ($k = 1.2$) for several mixtures, $\nu = 0.568$: those from Fig. 2.9(b) (•), and those where $\overline{d} = 15$mm: (i)12 & 18mm (ii) 14 & 16mm (iii) 10, 15, & 20mm (iv) 10,12.5,15, 17.5, & 20mm (v) 15mm particles (□). The solid line shows $p^* = K\lambda_Z^2$, K=10.1; k=1.2.

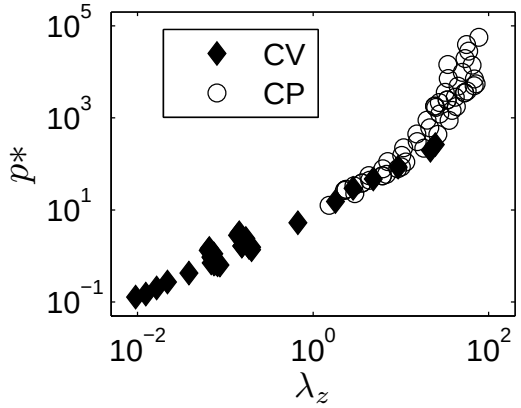

Figure 2.11: p^* vs. λ_Z^2 ($k = 1.2$) for several mixtures from constant volume (CV) and constant pressure (CP) simulations. Notice that λ_Z^2 approaches a constant value at higher pressure.

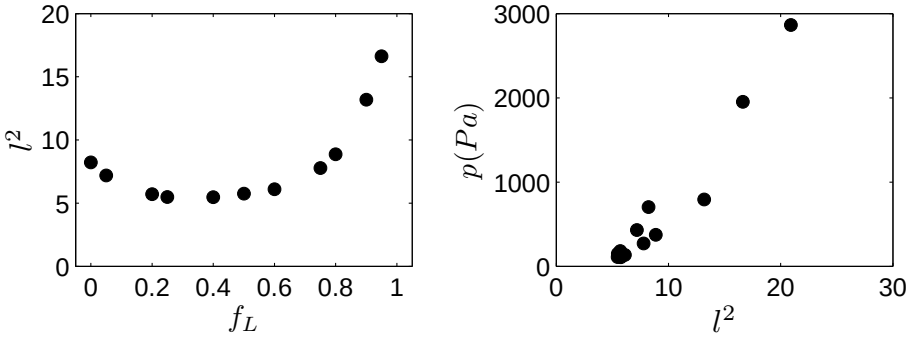

Figure 2.12: (a) l^2 vs. f_L for CV simulations $\nu = 56.8$ %. (b) p vs. l^2 for the simulations in (a).

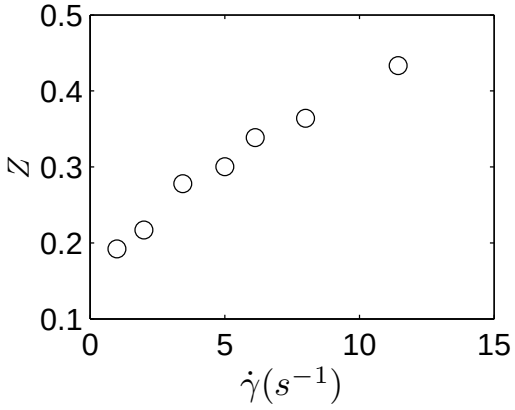

Figure 2.13: (a) Z vs. $\dot{\gamma}$ for CV simulations $\nu = 56.8$ % and $f_L = 0.50$.

Chapter 3

Rheology of dense granular mixtures: Particle-size distributions, boundary conditions, and collisional time scales

3.1 Introduction

The dependence of the rheology of granular mixtures on particle size distribution leads to dramatic local and global system dynamics. For example, an apparent feedback mechanism between local particle size distribution and rheology appears to be a primary driving mechanism for some pattern formation problems such as a fingering phenomenon observed in geophysical mass flows [72]. Another dramatic example occurs in rocky debris flows, where segregation in conjunction with the dependence of the rheology on the local size distribution has been proposed as a possible cause of what are referred to as "long run-out avalanches" where the particles flow at slopes far lower than a measured angle of repose [73, 74]. However, there has been relatively little systematic investigation of how the rheology of a mixture depends on its particle size distribution

[75, 68, 22]. A possible exception to this statement is in the development of kinetic theory which has the capacity to account explicitly for dynamics in granular mixtures (e.g., Refs. [76, 77, 78]). Current formulations have been shown to be quite effective at modeling the behavior of relatively sparse mixtures (e.g., [22], [79]). However, these formulations have been shown to be limited to sparse or moderately dense granular materials (e.g., Refs. [80, 81, 79]), below the solids fractions of certain geophysical flows such as debris flows.

In fact, until recently there has been no agreement on a modeling framework for dense sheared granular materials, even those comprised of monosized spherical particles. However, it is generally agreed that the rheology of relatively hard spherical particles should depend in some way on the following non-dimensional form of the shear rate $\dot{\gamma}$ [16, 36, 82]:

$$I = (\dot{\gamma}d)/(\sqrt{p/\rho}), \tag{3.1}$$

referred to as the inertial number. Here, d is the particle size; ρ is the material density of the particles, and p is the average pressure or normal stress.

The origin of I can be traced back to Bagnold's hypothesis [11], which states that $p = k\rho d^2\dot{\gamma}^2$, where k is a constant proportionality. In this context, I^{-2} can be assumed as the proportionality constant in Eq. 2.4. Later, Savage [82] noted that this proportionality constant serves to delineate a transition from one flow regime to the next for granular flows: he suggested that systems with smaller values of k are inertia dominated while those with larger values of k are as friction dominated. In this context, k is referred to as the Savage Number [2]. The inertial number is the square root of the Savage Number. Similarly, the value of a system's inertial number has been shown to indicate the nature of the flow: Systems of very small values of I ($\leq 10^{-3}$) are quasi-static, and their rheological properties are rate independent; Systems with relatively high values of I (≥ 0.2) (e.g., Ref. [33]) generally behave as a dissipative gas, and kinetic theory of dense gas predicts the behavior well (e.g., [76, 77, 78]); Systems with intermediate values of I are in the dense flow regime, where the kinematics and the rheology appears explicitly dependent on I. We are concerned with the systems of intermediate values of I.

The kinematics of the Couette cell flow (Fig. 3.1(a)) systematically vary with the

value of I. We explore this for constant volume simulations of different solid volume fractions in Fig. 3.2. For lower values of I the velocity profile is linear (Fig. 3.1(b)). Fig. 3.2(a) shows the velocity profile for f_L=0.0, for ν=0.3, 0.4, 0.5, and 0.568 which correspond to I value of 1.57, 1.10, 0.56 and 0.067 respectively, where I is computed by assuming a uniform $\dot{\gamma} = 3.44\ \mathrm{s}^{-1}$ so the change in I is entirely associated with changing p with ν. Under these conditions, when I increases the velocity profile changes from a linear shape to an "S" shape. Fig. 3.2(b) shows the volume fraction profile for the mixtures shown in Fig. 3.2(a). For larger values of I the profile is not uniform; the particle concentration increases towards the center of the cell.

For 2-dimensional steady dense flows such as those in a thin slowly rotated drum (e.g., Refs. [83, 84]), a thin chute (e.g., Refs. [75, 85]) or a Couette cell, as in Fig. 3.1(a) (e.g., Refs. [11, 86, 12, 87]), the rheology is efficiently described using an *effective friction coefficient* $\mu^* \equiv \tau/p$ where τ is the local averaged streamwise (shear) stress. Depending on the boundary conditions, the relationship between μ^* and I has been found described well for *monosized* particulate flows using simple relationships. These include linear [33, 88, 89] and power law [90] relations and, over the broadest range of flow conditions by more complicated relationships [72, 8, 37, 31]. da Cruz et al. [33] proposed a linear relationship of the form,

$$\mu_I^* = \mu_1 + bI. \tag{3.2}$$

μ_1 and b are fitting parameters derived from 2-dimensional DEM simulations of dense Couette flow of uniform particle size. The fitting parameters depend on many factors, such as friction coefficient of particles. μ_1 can be considered as the lower limit of μ_I^* as $I \to 0$, associated with quasi-static deformation. However, based on this model fitting μ_I^* increases indefinitely as I increases, which is not intuitively correct. This equation works for limited range of I in the dense granular flow regime. Based on similar 3-dimensional simulations Hatano [90] proposed a power law relationship

$$\mu_I^* = \mu_1 + \beta I^c. \tag{3.3}$$

β and c are fitting parameters. The linear and the power-law relationships are entirely based on fitting models to DEM simulation results. Based on physical experiments of gravity driven flow over inclined plane and chute Jop et al. [6, 37, 31] proposed that

$$\mu_I^* = \mu_1 + (\mu_2 - \mu_1)/(I_o/I + 1). \tag{3.4}$$

Here, μ_1, μ_2, and I_o are all, strictly speaking, fitting parameters, but μ_1 and μ_2 are considered effective friction coefficients associated with quasi-static deformation and rapid collisional flows, respectively.

This framework has been shown to be relatively successful for monosized particle systems (within some limits, as described in Ref. [30]). Further, there have been successful extensions of this framework to cohesive monosized particle systems [91]. However, there are two ambiguities in its application to mixtures of different sized particles depending on the boundary conditions. First, it is not immediately obvious what particle size is appropriate for the representative d in Equation 3.1. Second, for confined sheared granular mixtures, p has a complicated dependence on particle size distribution (e.g., Refs. [92, 22]) which we discuss shortly. Once these are determined, there could be other complications to the simple relationships derived for μ^* as a function of I. For example, the parameters in Equation 3.4 may vary with the particle size distribution.

There have been relatively few reports of research specifically designed to investigate the effect of the particle size distribution in a mixture on the system's rheology. Most involve sparser systems than the dense flows we consider here, (e.g., [68, 22, 93]), others, focused on specific details over a limited range of mixtures [82, 94]. Karion and Hunt [68] performed Discrete Element Method (DEM) simulations of binary mixtures of different sized particles in a constant volume Couette cell for an areal solids fraction of $\nu_A = 0.75$. For a single size ratio they found that increasing the fraction of large particles f_L increased both p and τ at the boundaries and decreased their ratio μ^*. Alam and Luding [22] performed event-driven simulations of particles up to $\nu_A \approx 0.6$ in a constant volume Couette geometry with Lees-Edwards boundary conditions [95]. For a given size ratio, they found that increasing f_L had a nonmonotonic effect on both p and effective viscosity $\tau/\dot{\gamma}$: they both decreased up to intermediate fractions of large particles and then increased again for higher fractions of large particles. These results are consistent with our recent simulation results for somewhat denser conditions [92], as we discuss in Section 3.3.

The results for p of the two studies are not consistent; however, they are not necessarily in conflict. Karion and Hunt [68] pointed out that in their simulations, changing

the particle size distribution also gave rise to differing amounts of slip between the particles and the shearing walls from one mixture to the next. The authors found for their simulations, this also resulted in variable velocity and temperature profiles. In other words, the variation of the boundary stresses from one system to the next were likely due to a combination of effects, the different particle size distributions as well as the variation of the kinematics from one system to the next. The differences between the two studies bring to light some of the difficulties in isolating the effects of particle size distributions from other features that might have an effect on local and global system rheology.

Rognon et al. [75] performed 2-d simulations of binary mixtures of particles of different sizes down a rough plane inclined at an angle θ with the horizontal. Their simulations were performed at a slightly higher solids fractions compared to those in Refs. [68, 22], $\nu_A \approx 0.8$, and the systems segregated (large particles to the free surface, small particles to the rough solid boundary). Unlike the work in Refs. [68, 22], neither p nor τ were controlled by particle size distribution; in a free-surface gravity driven non-accelerating flow such as that used in the study by Rognon and colleagues, p is equivalent to the lithostatic or hydrostatic pressure, and $\tau = p\ \tan\theta$. In the paper, Rognon et al. focused primarily on a description of the relationship between I and μ^*, where they substituted the average particle size $\overline{d}$ for d in Equation 3.1 and they used $\mu^* = \tan\theta \approx \theta$. While their mixtures segregated – large particles towards the free surface and small particles toward the rough boundary – their data suggested I was nearly independent of depth and:

$$\mu^* = a_1(d_r, f_L) + b_1(d_r, f_L)I. \tag{3.5}$$

Here a_1 and b_1 are fitting parameters, both potentially functions of d_r and f_L; d_r is the ratio of diameter of large particles to diameter of small particles and f_L is the fraction of large particles in the mixture. For the same μ^* (i.e., θ), they found that I increases for increasing f_L, particularly for larger values of d_r, though the authors comment about some slip at the boundary for larger particles as well. The work by Rognon et al. [75] presents a hopeful start for the application of recently established rheological rules for sheared dense monosized granular materials to mixtures of particles of different sizes. However, questions remain regarding the applicability of this framework for a

broader range systems, for example, constant volume systems where p, τ, and μ^* vary dramatically with particle size distribution [68, 22, 92].

In the research described in this chapter, we probe the dependence of the rheology of sheared granular mixtures in 3-d on the particle size distribution and how this response varies under different boundary conditions. As we describe in Section 3.2, we use binary mixtures of relatively hard, non-cohesive particles whose components differ only in size (not material density). We shear the particles in a plane Couette geometry without gravity (e.g., Fig. 3.1(a)) for these studies as it provides a simple set of kinematics to isolate the quantities of interest. Specifically, under the relatively high solids fractions we use ($\nu \approx 0.57$) the shear rate is relatively constant (Fig. 3.1(b)), and segregation is minimized as we describe Chapter 2 in Refs. [92],[69].

In Sections 3.3 and 3.4 we describe our results from constant volume and constant pressure simulations where we show that both I and μ^* vary with particle size distribution in a manner that depends on the boundary conditions. Regardless, a single equation describes the relationship between I and μ^* independent of boundary conditions. In Section 3.5, we probe the underlying mechanisms governing the system response to particle size distribution under different boundary conditions by investigating chief time scales associated with interparticle interactions for the different simulations. We conclude in Section 3.6 with some future challenges to the study of the rheology of mixtures of different sized particles.

3.2 Simulation setup

For our simulations we use the Discrete Element Method (DEM) as described in Chapter 1. The simulation set-up, the Couette cell and the particles are the same as what we have described in Chapter 2. We will discuss some the simulation set-up details in this section.

We perform simulations of binary mixtures of 10 mm and 20 mm particles with a polydispersity of 10% in the diameter of each component to inhibit crystallization. We vary the concentration of large particles from 0 to 100% as we detail below. The average particle diameter $\overline{d}$ is essentially linearly dependent on the fraction of larger particles f_L: $\overline{d} \sim (10 + 10 f_L)$ mm. (The relationship is only approximate because of the

polydispersity of each of the particle species.)

The particles are sheared in a plane Couette cell (as in Fig. 3.1) in the absence of gravity. Two parallel walls contain the particles in the $y-$direction, one of which moves with constant velocity in the $x-$direction, U_w. The boundaries are periodic in the other two directions. To minimize particle slipping at the top and bottom boundaries, we affix particles in a random array to the walls. These "glued" particles have the same material properties as the flowing particles. Results appear independent of the size of these "roughness elements" provided they satisfy two conditions: (1) that they are large enough to provide sufficient roughness to prevent slipping and (2) that they are arranged to prevent small particles from being preferentially trapped, subsequently altering the internal solids fraction. (We note that Ref. [96] and references within discuss how different roughness conditions give rise to varying amounts of slip.) We use $10mm$ particles arranged randomly on the walls which met most of the necessary criteria except that they allowed for a bit of slip for the mixtures of the largest fraction of $20mm$ particles, $f_L = 0.95, 1.00$. We discuss this in more detail in the subsequent sections.

For the constant pressure simulations, the non-translating wall is allowed to move vertically, but the steady state value is approximately the same, $H \approx 240$ mm as we will discuss. For the constant volume simulations the wall that is not translating in the $x-$direction is fixed and the cell height H is held constant at $H = 240$ mm for nearly all of the results presented here, the specific value of H was chosen so that the solids fraction ν corresponds to specific results from the constant pressure simulations. The other two dimensions for most of the simulations described here are length $L = 288$ mm (in the streamwise direction) and breadth $B = 150$ mm. The total mass of the particles is the same for each simulation, approximately 15.6 kg, resulting in a solids fraction of $\nu \sim 0.57$. The total number of particles in these simulations ranges between approximately 1300 for $f_L = 1$ to approximately 10500 for $f_L = 0$. A few exceptions to the system size were performed to assure independence of the results on system size, as we note below.

To calculate I and μ^*, we calculate $\dot{\gamma}$, τ, and p using the relative positions of the particles and the walls. We calculate $\dot{\gamma}$ using the average value for H after the system has reached steady state as $\dot{\gamma} = U_w/H$. We calculate the boundary stresses τ and p

by summing the x- and y- components, respectively, of all forces on a boundary wall and on the particles affixed to that boundary and dividing the sum by the area of the boundary. Finally, for d, we use $\overline{d}$ for the whole system.

3.3 Results: constant volume simulations

Figure 3.3 presents results from several sets of simulations performed under constant volume conditions. Figures 3.3 (a) and (b) show that for any particular mixture, both p (as discussed in Ref. [92]) and τ scale as $\dot{\gamma}^2$ as discussed in Chapter 2. The dependence of p and τ on $\dot{\gamma}^2$ (Figs.3.3(a) and (b)) brings to the mind a model based on momentum transfer proposed by Bagnold [11] previously discussed:

$$p_{Bag}, \tau_{Bag} \propto \rho \lambda^2 d^2 \dot{\gamma}^2 \tag{3.6}$$

where λ is what Bagnold called the linear concentration of particles: $\lambda = [(\nu_{max}/\nu)^{1/3} - 1]^{-1}$. Here, ν is the solids fraction of the granular material, and ν_{max} is the maximum solids fraction (≈ 0.74 for a uniform system of spheres). Equation 3.6 suggests a linear dependence of p and τ on d but only if ν_{max} is constant. In fact, p and τ do not depend monotonically on $\overline{d}$, most easily seen when p and τ are plotted vs. f_L for one particular shear rate, as in Fig. 3.3(c). As f_L increases, both p and τ first decrease then increase. This trend is qualitatively similar to that found by Alam and Luding for sparse 2-d systems [22]. In Ref. [92], we discussed that for our dense systems, this is likely associated with the variation of $\nu_{\max}$ for different mixtures. In other words, mixtures of particles of different sizes typically have a higher $\nu_{\max}$ than do monosized systems, and $\nu_{\max}$ for the mixtures varies from one mixture to the next. We hypothesized that for our mixtures of 10 and 20 mm particles, $\nu_{\max}$ was highest for mixtures near $f_L \sim 0.5$ and lowest for systems near $f_L \sim 0$ or 1. For our systems sheared under the same constant volume conditions, this is reflected in a lower "dispersive pressure" for mixtures near $f_L \sim 0.5$ than for systems near $f_L \sim 0$ or 1. From the results shown in Fig. 3.3(c) we can see there is an analogous effect on τ.

Based on the discussion above, we have shown in Chapter 2 and Ref. [92] that Equation 3.6 may be adapted for pressures in sheared granular mixtures in the form of $\sigma_{Bag,m}$:

$$\sigma_{Bag,m} \propto \rho\lambda_Z^2\overline{d}^2\dot{\gamma}^2. \tag{3.7}$$

Here, $\lambda_Z \sim [(k/Z+1)^{1/3}-1]^{-1}$, an effective linear concentration we have previously derived [92] by considering an effective free space for a particular mixture based on results described in Refs. [60, 20]. Z is the coordination number, or average number of contacts per particle. k is a parameter that depends on the hardness of the particle [92]. For these particles, for pressure we have found $k \approx 1.2$ [92].

Considering Equation 3.7, we plot p, τ, and $\mu^* \equiv \tau/p$ as a function of $\rho(\lambda_z\overline{d}\dot{\gamma})^2$ in Figure 3.3(d). Both p and τ increase roughly with $\sigma_{Bag,m}$. However, the increase of τ is less, so that μ^* decreases with $\sigma_{Bag,m}$. In the classic model by Bagnold, p and τ have exactly the same dependence on $\sigma_{Bag,m}$ so that μ^* is constant. We note, however, that a non-constant μ^* is entirely consistent with many experiments and simulations performed for *monosized* granular materials as in Equation 3.4. In fact, as is evident in the plot of μ^* vs. f_L in Fig. 3.3(c), there is a subtle difference in the function dependence of τ and p on f_L. As f_L increases, μ^* first increases then decreases, indicating that τ is slightly less sensitive to changes in f_L than is p. This indicates Equation 3.7 may not strictly be the correct functional form for τ, a question we are currently investigating and does not affect the focus of this chapter.

In Fig. 3.3(e) we plot I as a function of f_L and find the relationship is similar to that of μ^* vs. f_L, though the peak in I for intermediate values of f_L is sharper. This functional dependence of I on f_L makes sense considering f_L has the effect not only in changing $\overline{d}$ but also, somewhat dramatically and non-monotonically, p. As f_L is increased from 0 to 1, $\overline{d}$ doubles, while p first decreases and then increases until, for $f_L = 1$ it reaches a value of a factor of 4 over its value at $f_L = 0$. (We note that the latter is consistent with the dependence of p on d^2 in Equation 2.4.) The combined effects of the changing values of $\overline{d}$ and p on I result in a nearly symmetric plot of I as a function of f_L around $f_L = 0.5$. Figure 3.3(f) is a parametric plot of μ^* vs. I for all of the data in Figs 3.3(a)-(d). Over the range of parameters we tested, we find this is equivalently well-fit by a straight line, and power law, and Equation 3.4 as shown in the Fig. 3.3(d). The exception to this rule is for the highest fraction of large particles ($f_L =$ 0.95 and 1.0) where there is appears to be significant slip at the boundaries. We include these points in the plot for completeness but do not include them in the fits. We also

include in this plot results from a smaller system where the height is $H = 160mm$ (and where the other parameters such as $\dot{\gamma}$ and ν are the same). We find that our results are independent of the system size.

3.4 Results: constant pressure simulations

Figure 3.4 presents analogous results from our constant pressure simulations. As in the simulations by Rognon et al. [75], p is fixed by the boundary conditions, but in contrast, τ and therefore μ^* may both vary with particle size distribution. Thus in this section we consider how f_L modifies the system response to varying p as well as how f_L affects μ^* and I for a fixed p. In Figs. 3.4(a) and (b) we look specifically at the effect of f_L (and p) on H, inversely related to ν at steady state. As one might expect, as the applied pressure increases, the height of the cell decreases (Fig. 3.4(a)). However, for each pressure, the corresponding height does not depend monotonically on the average particle size in the mixture. Instead, the smallest resulting H (and consequently, the largest ν) correspond to intermediate values of f_L (Fig. 3.4(b)). As we have previously pointed out in Ref. [92], this is further indication that the packing efficiency is greater for mixtures near $f_L \sim 0.5$ than for mixtures of low concentrations of either particle component in the binary mixtures.

Figure 3.4(c) shows τ and μ^* as a function of p for the same simulations shown in Fig. 3.4(a). From these data we note that τ increases with increasing p but not linearly so; their ratio μ^* decreases with increasing pressure. On the other hand, τ and μ^* seem only slightly influenced by f_L. This is more clear in the plots of μ^* vs. f_L for specific pressures shown in Fig. 3.4(d). The results in Fig. 3.4(d) indicate there is a gentle increase in μ^* with increasing f_L. For the highest values of f_L, there is evidence for slipping at the boundary as the trend of increasing μ^* with increasing f_L dramatically reverses. We assume the results for these values of f_L are dominated by this boundary effect. We do not consider them in the subsequent discussion, and leave this to the discussion in Section 3.5.

In Fig. 3.4(d), we also plot I vs. f_L and find that I also increases with f_L. For these data, the relationship is nearly linear, not surprising given the explicit linear dependence of I on d. We note, though, that $\dot{\gamma}$ changes inversely with H which is also dependent

on f_L, and therefore I is not strictly linearly related to $\overline{d}$. Figure 3.4(e) is a parametric plot of μ^* vs. I for the data in Figs. 3.4(a),(c). As is the case for the constant volume data, over the range we report here in detail, we find this is nearly equivalently well-fit by a straight line, a power law, and Equation 3.4. The fitting parameters (as detailed in the caption of Fig. 3.4) are similar to most of those for the constant volume simulations though there are some differences, most notably in the exponent of the power law fit. As an aside, we note that for lower values of p and ν (and correspondingly higher values of I), μ^* saturates (as found in monosized systems, [33, 31]), and we find Equation 3.4 best represents this behavior.

In Fig. 3.4(f) we plot a compilation of the results from both constant pressure and constant volume simulations for all of the data shown in Figs. 3.3 and 3.4. To test dependence on system size, we also plot results for some constant pressure and constant volume results from a cell of $H = 160mm$ but otherwise of the same conditions for the other results described in this Chapter. The μ^* vs. I data from all of the different simulations appears to match well. The exceptions, as mentioned previously, are the data from the largest values of f_L where we see evidence of slip. We discuss this in some detail in Section 3.5. Otherwise, from the plot in Fig. 3.4(f), the functional dependence of μ^* on I appears independent of f_L and also independent of boundary conditions and system size.

The collapse of the μ^* vs. I data, independent of boundary conditions, seems startling at first given the stark contrast between the functional dependencies of μ^* and I on f_L for the two boundary conditions. For the constant volume simulations, the variations in μ^* and I with f_L appear controlled by two factors: the variable amount of free space per particle as it varies with mixture and the average particle size in the mixture. In contrast, for the constant pressure simulations, the change in μ^* and I appear dominated by the change in $\overline{d}$. The similarities and differences to the system responses to changes in f_L under different boundary conditions provides an opportunity to isolate the underlying mechanisms responsible for changing the inertial number. We do so in the next section.

3.5 Time scales of interparticle collisions

To gain some insight on how such different boundary conditions can give rise to similar dependencies of μ^* on I, we consider how time scales associated with interparticle collisions vary with f_L for the constant volume and constant pressure volume conditions. Here we consider two basic time scales of interparticle collisions: (1) the contact duration t_c and (2) the "mean free path" time, or the time particles spend between collisions with other particles t_{mfp}, or the time interval a particles spend without touching other particles.

Fig. 3.5(a) shows the probability distribution function of t_c for f_L =0.50 and total volume fraction ν equal 0.40, 0.45 and 0.568. The general shape of the pdf is similar for the three systems. The peak values of the pdf for the three systems correspond approximately to the same value of t_c. The most important difference between the pdf plots is the width of the pdf. For lower values of ν the width of the pdf is narrow, which indicates the contacts are dominated by pure binary collisions of particles. For higher values of ν range of t_c increases as enduring contacts also prevail in the flow. Fig. 3.5(b) shows the pdf of t_{mfp} for the same system.

In the following, we consider the average contact duration $\bar{t}_c$ and $\bar{t}_{mfp}$. In Fig. 3.6(a) we plot $\bar{t}_c/\bar{t}_{mfp}$ as a function of f_L for the constant volume results shown in Figs. 3.3(c)-(e). As shown, for mixtures where one component dominates ($f_L \approx 0$ or 1), $\bar{t}_c/\bar{t}_{mfp} \approx 1$. For intermediate values of f_L the particles spend less of their time per collision in contact with other particles. Specifically, for $f_L \approx 0.5$, $\bar{t}_c/\bar{t}_{mfp}$ dips to ≈ 0.2. When we consider this in the context of the variation of the effective free space per particle with changing f_L, this seems entirely consistent. That is, for intermediate values of f_L where the potential packing is most efficient and there is more effective free space for particles to move around, the particles spend, on average, less of their time in contact with other particles. The inverse is true for mixtures where a single species of particles dominates. That is, for $f_L \approx 0$ or 1 the particles have less free space and spend more time on average in contact with other particles.

In Fig. 3.6(b) we plot $\bar{t}_c/\bar{t}_{mfp}$ vs. f_L for the constant pressure simulations of p=0.25 kPa shown in Figs. 3.4(a)-(e). For these constant pressure simulations, $\bar{t}_c/\bar{t}_{mfp}$ decreases with increasing f_L. These results imply that either the particles take longer to travel

from one collision to another or they stay in contact for less time as the average particle size increases (or both). We discuss this in more detail shortly, but neither is immediately physically intuitive. Nevertheless, for both the constant volume and constant pressure results, lower values of $\bar{t}_c/\bar{t}_{mfp}$ correspond to systems with higher values of I. (Compare results in Figs. 3.6(a) and (b) to those in Figs. 3.3(e) and 3.4(d).)

Figure 3.6(c) is a parametric plot of $\bar{t}_c/\bar{t}_{mfp}$ vs. I for both constant volume and constant pressure simulation results shown in Figs. 3.6(a) and (b). We find that for nearly all results, $\bar{t}_c/\bar{t}_{mfp}$ monotonically decreases, nearly exponentially, as a function of I. In other words, as the system is moving a small distance along the spectrum from a quasi-static state at low values of I to a gaseous state at high values of I, the particles spend increasingly shorter times per collision in contact with other particles. There is an exception for the highest values of f_L where we have previously mentioned there is a bit of slip at the boundaries. We address the effect of the slip in more detail near the end of this section.

To further understand the physical relationships between these time scales and the system behaviors, we plot separately $\bar{t}_c$ and $\bar{t}_{mfp}$ for the mixtures (Fig. 3.6(d) and for the individual components (Fig. 3.7(a)-(d)). For the systems under constant pressure conditions, $\bar{t}_c$ is relatively independent of f_L (Fig. 3.6(d) and Fig. 3.7(a)), and the variation of the ratio $\bar{t}_c/\bar{t}_{mfp}$ is primarily controlled by the variation of $\bar{t}_{mfp}$ with f_L. For the mixture, $\bar{t}_{mfp}$ increases with f_L, and plateaus near $f_L \approx 1$ (Fig. 3.6(d)). In fact, $\bar{t}_{mfp}$ increases nearly exponentially for both components in the constant pressure simulation, though $\bar{t}_{mfp}$ is significantly less for the large particles than for the small particles. The plateau in the mixture plot of $\bar{t}_{mfp}$ vs. f_L (Fig. 3.6(d)) is the result of the increasing contribution of the large particles to the mixture at large values of f_L.

For the systems under constant volume conditions, the variation of the ratio $\bar{t}_c/\bar{t}_{mfp}$ with f_L is controlled by both the variation of $\bar{t}_c$ and $\bar{t}_{mfp}$ with f_L. For these conditions, $\bar{t}_c$ (Figs. 3.6(d) and 3.7(c)) dips for intermediate values of f_L, and then increases dramatically for the highest values of f_L. The trend is similar to that of p and τ vs. f_L (Fig. 3.4(c)). In contrast, $\bar{t}_{mfp}$ for the mixture reaches its maximum value near $f_L \sim 0.5$. $\bar{t}_{mfp}$ of the individual components increase monotonically with f_L but the curve is not so smooth as under constant pressure conditions. This is likely a superposition of two trends: an increase of $\bar{t}_{mfp}$ with f_L similar to that in Fig. 3.7(b) and an increase in $\bar{t}_{mfp}$

with increase in effective free space near $f_L \approx 0.5$. We are currently investigating this in more detail. Nevertheless, the effect on the average $\bar{t}_{\text{mfp}}$ curve is to cause an increase for small values of f_L and then a decrease for larger values of f_L as the influence of large particle properties at higher values of f_L increases. In the end, these rather asymmetric dependencies of the values of $\bar{t}_{\text{c}}$ and $\bar{t}_{\text{mfp}}$ for the individual components balance one another resulting in a symmetric curve for $\bar{t}_{\text{c}}/\bar{t}_{\text{mfp}}$ vs. f_L for the mixture.

The discussion above pertains to changes in I and $\bar{t}_{\text{c}}/\bar{t}_{\text{mfp}}$ when we vary f_L while holding ν constant. We have found the trend is similar when we decrease ν. Specifically, as we decrease ν, I increases and $\bar{t}_{\text{c}}/\bar{t}_{\text{mfp}}$ monotonically decreases, nearly exponentially as a function of I. We understand the processes that lead to this as are follows. First, as ν decreases, the pressure decreases as well. If nothing else is varied (e.g., the same mixture is used), this results directly in a lower value of I according to Equation 3.1. Also for the same mixture and same shear rate, as ν decreases, the typical distance from one particle to the next increases, thus $\bar{t}_{\text{mfp}}$ increases. On the other hand, $\bar{t}_{\text{c}}$ is relatively independent of changes in ν for low values of ν as it approaches a binary collision duration limit. As a result, $\bar{t}_{\text{c}}/\bar{t}_{\text{mfp}}$ decreases with decreasing ν. For increasingly smaller values of ν, granular temperature - corresponding to the velocity variance - has been shown to increase [97], which we believes results in a less dramatic increase in $\bar{t}_{\text{mfp}}$ at higher values of I and a correspondingly less dramatic decrease in $\bar{t}_{\text{c}}/\bar{t}_{\text{mfp}}$.

We conclude this section with a brief discussion of the effect of the slip on the boundaries on these results for the highest values of f_L. As we mentioned, both the constant pressure and constant volume simulations, the simulations with the largest values of f_L exhibited some noticeable slip at the boundaries. As illustrated by Fig. 3.8 this effect grows relatively abruptly near $f_L \approx 0.95$. We believe at this fraction the fact that the roughness elements are smaller than the $d = 20mm$ particles reduces the effective friction between the wall and the larger particles which dominates the interactions at these values of f_L. Since we calculate I using $\dot{\gamma} = U_w/H$, our calculations effectively overestimate I for the bulk of the flow for these conditions of non-negligible slip. When we recalculate I using $\dot{\gamma}$ in the bulk, this shifts the errant data in Figs. 3.3(f) and 3.4(e) to the left somewhat, but not enough to put them on the curve. Further, if I is reduced farther, the relevant points in Fig. 3.6(c) move farther away from the trend. This indicates that the slip not only reduces $\dot{\gamma}$ for the constant volume simulation

but μ^* and $\bar{t}_c/\bar{t}_{mfp}$ as well. The reduction in $\bar{t}_c/\bar{t}_{mfp}$ associated with the slipping may be directly related to the reduction in $\dot{\gamma}$ for solids fractions this high. For the constant pressure simulations the effect is essentially the same, but since I is dominated by f_L, the resulting changes of I are much less noticeable. The slip is reduced for these mixtures when larger roughness elements are used, but these walls give rise to problems with larger fractions of smaller particles which get trapped in between the larger roughness elements subsequently changing the effective sheared mass and solids fraction depending on the mixture. This might be alleviated with another type of boundary conditions, such as Lees Edwards boundary conditions.

3.6 Summary and future work

We have used numerical simulations of binary mixtures of different sized particles sheared in a Couette cell to gain some insight on how rheology of granular mixtures varies with particle size distribution. We have found that both the Inertial number I and the associated system rheology can be tuned by simply changing the mixture components. However, the nature as to how it is tuned depends on the boundary conditions. Under constant volume conditions where average particle size and effective free space per particle varies with particle size distribution, the variation in I is controlled in large part by the variation of effective free space per particle. Under constant pressure conditions, the variation in I is dominated by the average particle size alone.

Nevertheless, the underlying physical interactions that determine the system behavior for these different conditions appears the same. We find I varies similarly and inversely with the relative time the particles spend in contact with other particles. Then the average effective friction coefficient follows the same functional form of I, also independent of mixture. Over the range of the most systematic studies we described in this Chapter, the relationship between μ^* and I is equally well represented by a linear relationship, a power law relationship, and the more complicated relationship described by Equation 3.4. When considering systems which vary over a limited range of I, then, the linear representation is the simplest, but the fitting parameters are likely associated with the particular range of I of concern. We note here that when we consider results

from special cases of high shear rate and those of higher pressure for results from particularly high and low values of I along with the rest of the data shown in Fig. 3.4(f), the curve most closely resembled Equation 3.4. Thus Equation 3.4 presents the most general form relationship between μ^* and I over the broadest range, even for mixtures of different sized particles.

We note that our results appear to be in slight conflict with those of Rognon and colleagues described in the introduction. As mentioned, Rognon et al. [75] found the fitting parameters for the relationship between μ^* and I for binary mixtures to be dependent on the size ratio and relative concentration of the two components in the mixture. The variation in the coefficients $a(D_r, S_r)$ and $b(D_r, S_r)$ is especially noticeable for high values of D_r, on the order of eight. Within a smaller range of D_r, we find our results independent of D_r. More recent the DEM simulations of gravity flows over inclined planes by Tripathi and Kharkar [98] demonstrated that the constitutive law is independent of D_r and S_r. Therefore, we hypothesize that the variation in the coefficients a and b the simulations of Rognon et al. [75] is most likely due to particle slips at the boundary for higher values of D_r and S_r.

This Chapter provides a first order systematic study of how particle size distribution influences the rheology of granular mixtures through governing time scales of the process for relatively hard particles. However, more is needed to understand the broader applicability of these results for variations of other properties of the mixture shown to be important for monosized particles, including solids fraction, [12], interstitial fluids (e.g., Refs. [82], [11], [12], [8]), cohesivity (e.g., Refs. [91], [99]), the effect of boundary conditions on these flows (e.g., Refs. [87], [97], [100]) and hardness of particles (e.g., [29], [28]). In the end the influence of particle size distribution on rheology of relatively hard particle mixtures may well provide insight for rheology of a broader range of granular materials, particularly as it pertains to important time scales of particle-particle interactions.

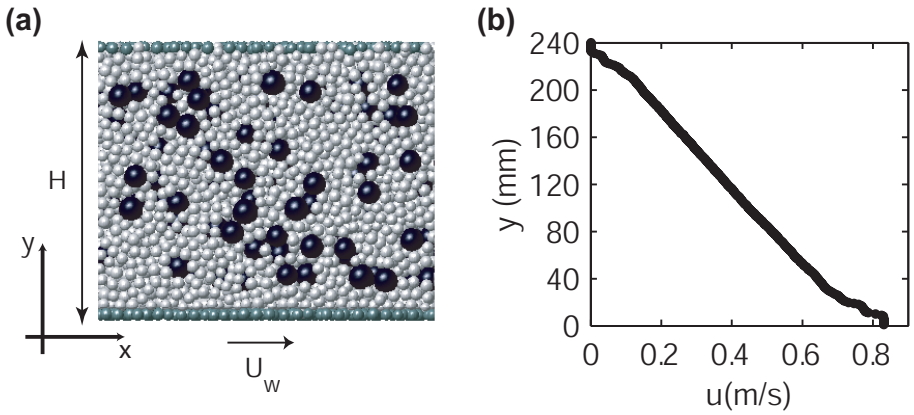

Figure 3.1: (a) Image taken from a parallel Couette cell simulation described in the text using a granular mixture consisting of 25% 20mm and 75% 10mm particles ($H = 240mm, U_w$=830mm/s) (b) Average streamwise velocity u as a function of distance across the cell y.

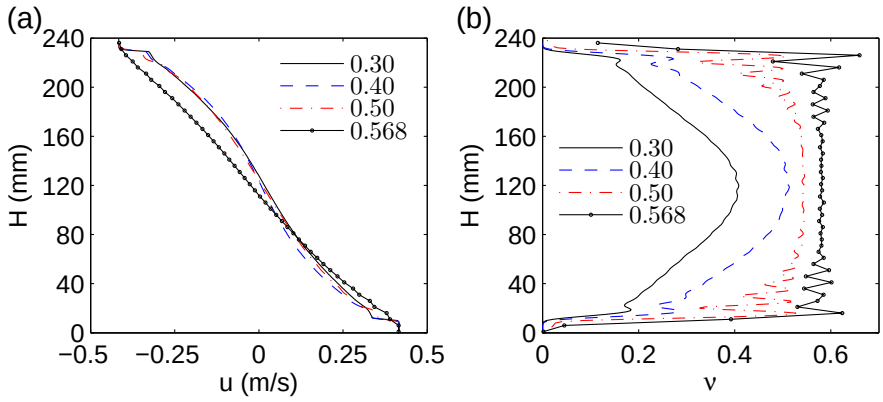

Figure 3.2: Results for simulations performed under constant volume conditions for monosized 10mm particle (f_L=0). (a) Velocity profiles for $f_L = 0.0$ and ν=0.3, 0.4, 0.5, and 0.568. (b) Volume fraction profiles for the simulations shown in (a).

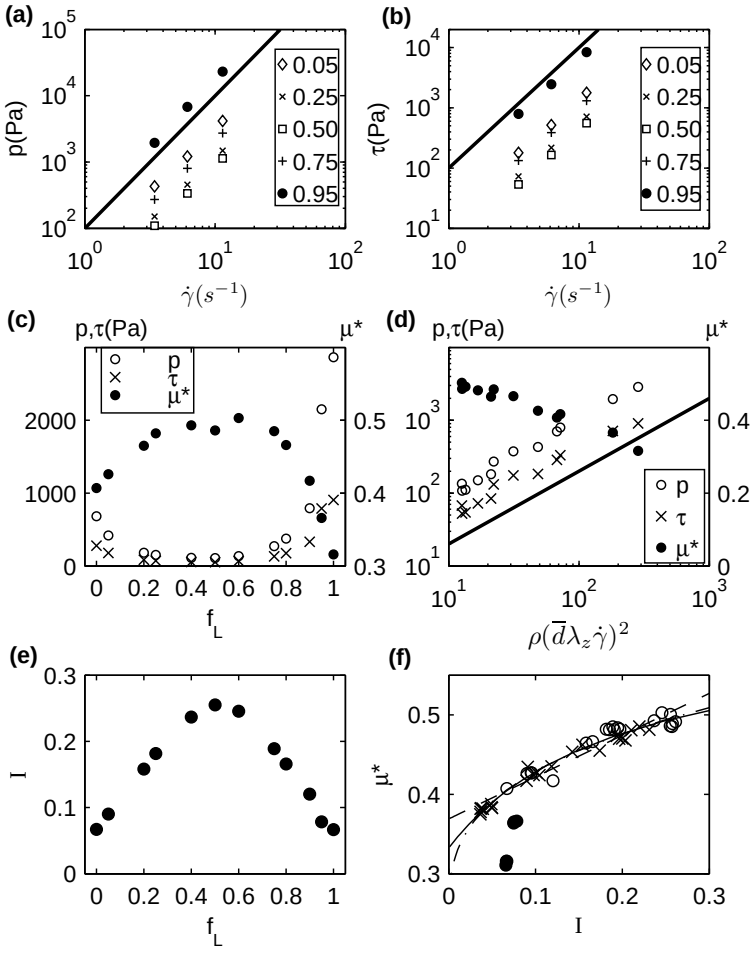

Figure 3.3: Results for constant volume simulations. (a) Pressure and (b) shear stresses as a function of shear rate for constant volume simulations. The fraction of large particles f_L for each is indicated in the legend. The solid line in each plot has a slope of two. (c) p, τ, and μ^* for one shear rate (3.44 s^{-1}) as a function of f_L. (d) p, τ, and μ^* as a function of Bagnold's inertial stress modified for particle mixtures, as described in the text. (e) I vs. f_L for the same data set plotted in (c) and (d). (f) μ^* vs. I for all data sets plotted in Figs. (a)-(d) (circles) and similar results for a smaller cell, $H = 160$ mm (marked by X's). For high fractions of large particles ($f_L = 0.95$ and 1.0) there is some slip leading to what appears to be errant data (filled circles). The lines are least squares fits to the data using: $\mu^* = a_1 + b_1 I$ (dashed); $\mu^* = a_2 + b_2 e^{c_2}$ (dot-dashed); Equation (2) (solid line). (a_1, b_1)=(0.37, 0.53); (a_2, b_2, c_2)=(0.24, 0.40, 0.32); (μ_1,μ_2,I_o)=(0.33, 0.62, 0.20). Due to the apparent boundary slip for high values of f_L (filled circles) we omit these data from the fits.

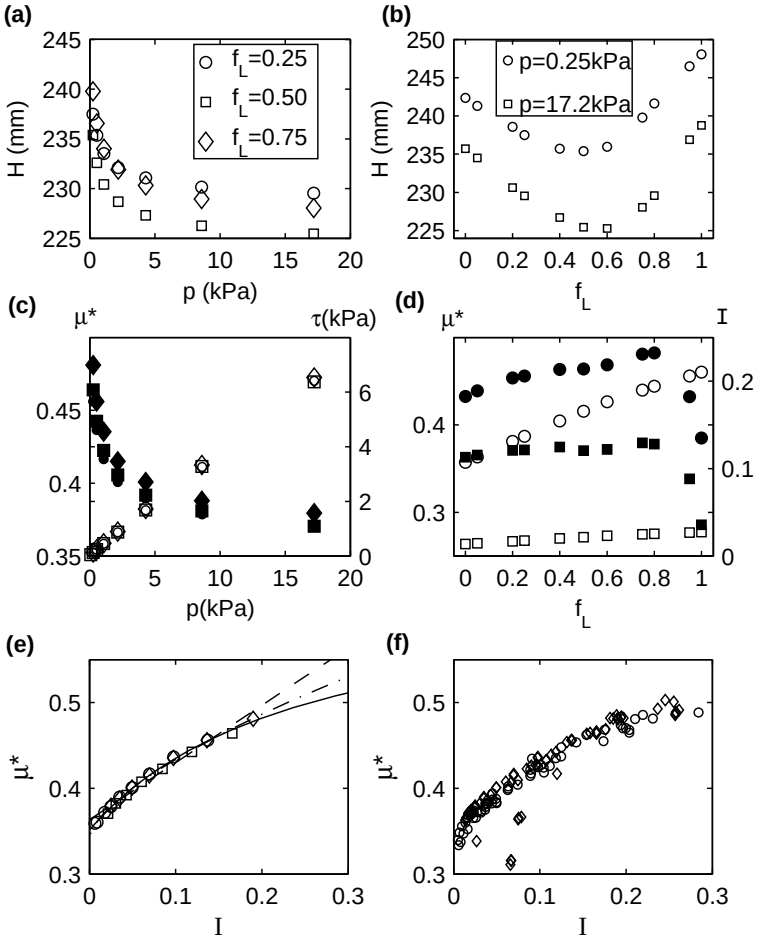

Figure 3.4: Results from constant pressure simulations. (a) The mean height of Couette cell as a function of applied pressure when the velocity of the lower wall $U_w = 830mm/s$. The fraction of large particles for each data set is noted in the legend. (b) H vs. f_L for two different pressures as noted in the legend. (c) τ (open symbols) and μ^* (filled symbols) as a function of p for the same data sets shown in (a). Symbols represent specific f_L's as noted in (a). (d) μ^* (filled symbols) and I (open symbols) as a function of f_L for the same conditions in (b). Symbol shapes correspond to the same pressures as in (b). (e) μ^* vs. I for constant pressure simulations shown in Figs. (a) and (c). Symbols represent specific f_L's as noted in (a). The lines are least squares fits to the data using: $\mu^* = a_1 + b_1 I$ (dashed); $\mu^* = a_2 + b_2 e^{c_2}$ (dot-dashed); Equation (2) (solid line). (a_1, b_1)=(0.36, 0.67); (a_2, b_2, c_2)=(0.34, 0.41, 0.66); (μ_1,μ_2,I_o)=(0.35, 0.65, 0.25). (f) μ^* vs. I for all simulations discussed in Fig. 3.3 and this figure. (Smaller cell H=160mm ($\circ$) and larger cell H=240mm ($\diamondsuit$). The points that fall below the trend are all for the highest values of f_L as discussed in the text.

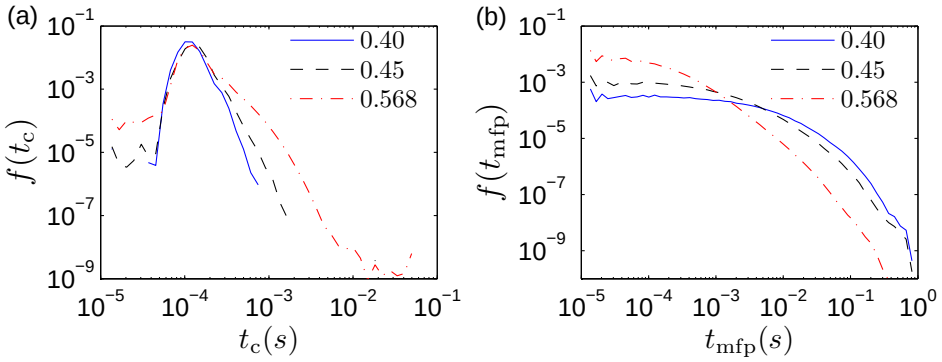

Figure 3.5: (a) Probability distribution function (pdf) of the contact duration, t_c, for $f_L = 0.5$. The legend indicates the total volume fraction, ν. (b) pdf of mean free path time for the systems in (a).

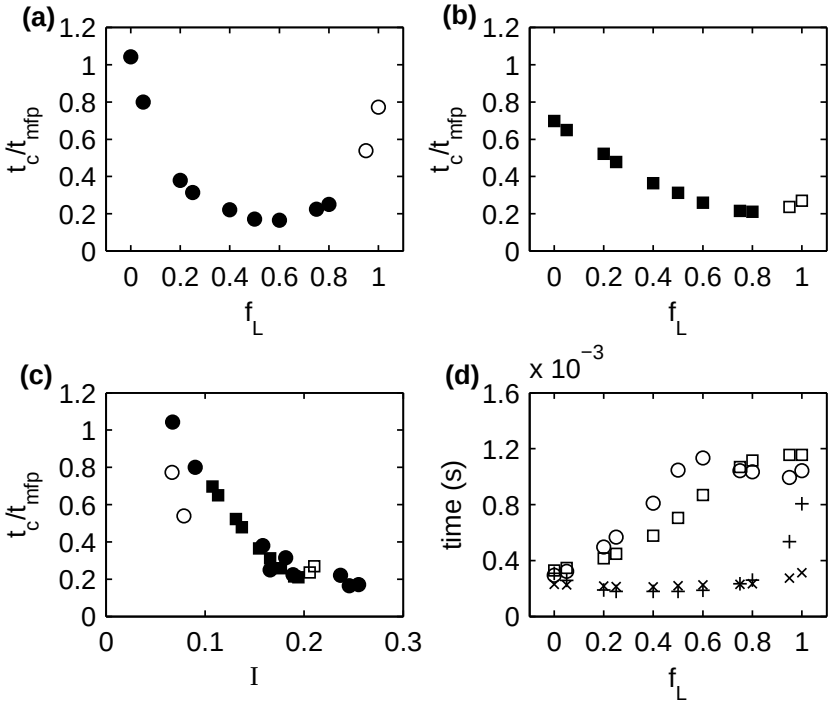

Figure 3.6: Collisional time scales for the mixtures for some of the constant volume and constant pressure results shown in Figs. 3.3 and 3.4. (a) The ratio of average contact duration $t_{\rm c}$ and time between consecutive collisions $t_{\rm mfp}$ as function of f_L for constant volume simulations shown in Figs. 3.3 (c)-(e)(H=240mm, U_w=830mm/s). Open circles are for f_L =0.95 and 1.0 mixtures. (b). The same as in (a) but for constant pressure simulations (H $\approx$ 240mm, U_w=830mm/s, p=0.25kPa). (c) The ratio of $t_{\rm c}$ and $t_{\rm mfp}$ as a function of I for constant volume simulations (circles) and constant pressure simulations (squares) shown in (a)and (b). (d) $t_{\rm c}$ and $t_{\rm mfp}$ as a function of f_L for constant volume simulation (+ and $\circ$) and for constant pressure simulation ($\times$ and $\Box$) respectively.

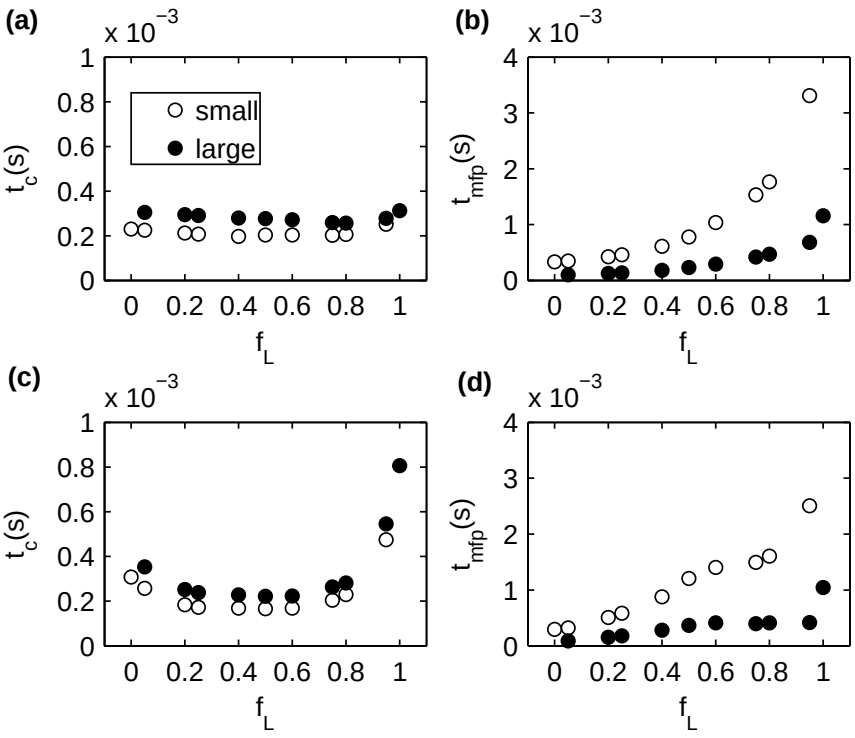

Figure 3.7: Collisional time scales for the components in the mixtures for the constant pressure and constant volume simulation results shown in Fig. 3.6. (a) and (b) Results for the constant pressure results shown in Fig. 3.6 for (a) $t_{\rm c}$ and (b) $t_{\rm mfp}$ as a function of f_L. (c) and (d) Results for the constant volume results shown in Fig. 3.6 for (c) $t_{\rm c}$ and (d) $t_{\rm mfp}$ as a function of f_L.

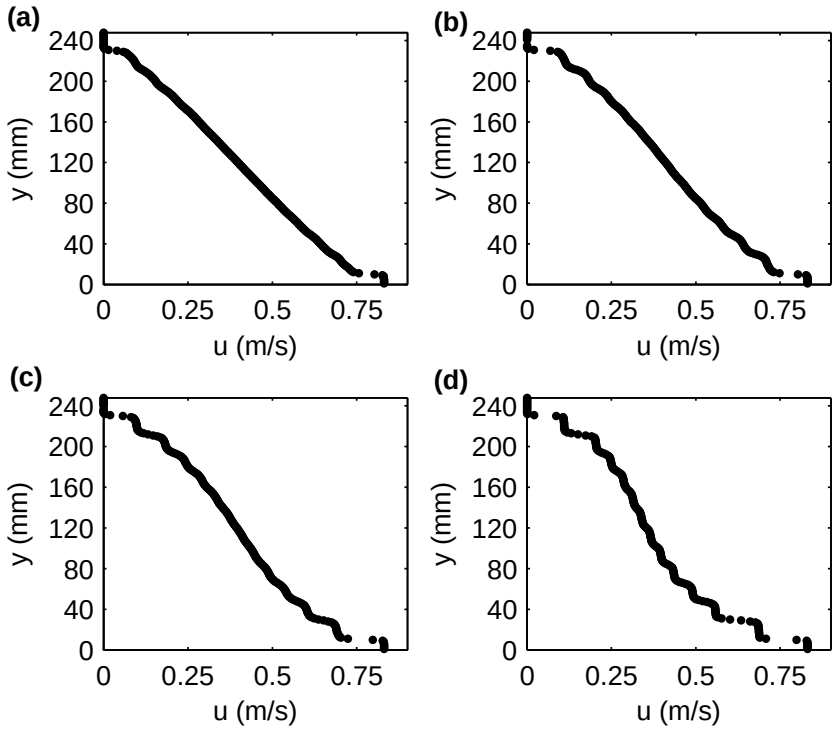

Figure 3.8: Velocity profiles for a subset of the constant volume simulations to illustrate the values of f_L where slip between particles and the roughened boundary becomes significant. For these, H=240mm, U_w=830mm/s, and f_L= (a) 0.80 (b) 0.90 (c) 0.95 and (d) 1.0

Chapter 4

Boundary stresses due to shallow granular flows

4.1 Introduction

When debris flows sweep down steep canyons they often entrain most sediment in their paths and scour to underlying bedrock. Inspection of the bedrock after such a flow event indicates that the bedrock is also worn and cut by the flow (e.g. [101, 102]).

Considerable progress has been made toward understanding bedrock incision by fluvial processes (e.g. [103, 104, 105, 106, 107, 108, 109]). However, there is significant evidence that the process by which bedrock is incised in the steepest hillslopes is fundamentally different than the processes associated with fluvial bedrock incision. For example, the common practice of plotting local channel slope as a function of cumulative drainage area along a river longitudinal profile (eg. [110, 111, 103]) typically reveals a distinct scaling break at slopes below which mass flows typically do not entrain sediment or travel [112, 102]. Experiments using flowing mixtures of gravel, sand, fine particles, and mud, here called *granular-fluid* flows, have provided further evidence for the ability of debris flows comprised of these materials to incise bedrock in a manner distinctly different from that by fluvial processes [113, 46, 114]. Relatively little work has been done on granular-fluid flow incision mechanics and theory, leaving a significant gap in the understanding of landscape evolution in steep upland regions (eg. [112, 115, 102]).

To develop a foundation for modeling bedrock incision by debris flows, Stock and

Dietrich [102] reasoned that the incision process is driven largely by the collisional forces associated with the relatively fluid-poor coarse front, or "snout" of such flows. They suggested that an expression for collisional stresses first proposed by Bagnold [11] in simple sheared granular-fluid flows

$$\sigma_{Bag} \sim \rho\lambda^2 d^2 \dot{\gamma}^2 \tag{4.1}$$

could be used to estimate the relevant collisional bed stresses resulting from debris flows. In this equation, ρ is the density of the material comprising the particles, d is particle size, and $\dot{\gamma}$ is the shear rate. The parameter λ is what Bagnold called the linear concentration (of solids), where he showed this parameter could be expressed as:

$$\lambda = \left[(\nu_{s,max}/\nu_s)^{1/3} - 1 \right]^{-1}. \tag{4.2}$$

Here, ν_s is the volumetric solids concentration of the granular material, and $\nu_{s,max}$ is the maximum solids fraction, well-known for uniform spheres to be approximately 0.74. However, while some work has been done to understand packing limits for certain mixtures (e.g., theoretical work by Rodine and Johnson [116] suggests $\nu_{s,max} \approx 1$ for multisize mixtures typical of natural debris flows), there is no general expression predicting $\nu_{s,max}$ for a mixture of different-sized particles. Based in part on Equation 4.1, Stock and Dietrich [102] proposed an expression for longterm bedrock incision rate dz/dt due to debris flows (where z is measured normal and outward from the free surface):

$$\frac{dz}{dt} = -K_0 K_1 R f L \left[\cos\phi \ \rho\nu_s D_e^2 \dot{\gamma}^w \right]^n \tag{4.3}$$

which depends on scaling of the excursion stresses with the average inertial stress (K_0), the relationship of rock resistance to incision rate (K_1), the inverse of the resistance of the bedrock to erosion (R), the frequency of occurrence of debris flows (f), the length of the snout (L), and a modified form of Bagnold's expression for collisional stress (bracketed term) raised to an empirically determined power, n. The modifications to Bagnold's collisional stress are as follows: the *cos* term is introduced to account for bed slope effects, ν_s (the volumetric solids concentration) replaces λ^2, D_e is a representative grain scale in the coarse front of a debris flow, and w is an empirical exponent. Stock and Dietrich [102] derived expressions for the coefficients of Equation 4.3 in terms of

physical parameters such as the mechanical property of the bedrock and crack spacing to develop a geomorphic transport law for debris flow incision.

In developing Equation 4.3, Stock and Dietrich [102] recognized challenges to applying Equation 4.1 to natural flows composed of particle mixtures in water or muddy fluids. Most notably, debris flows are composed of particles of a wide size distribution for which the appropriate choice of d is not clear. This choice is complicated by the fact that particles tend to self-segregate by particle size (e.g., [117, 118]), as well as by other particle properties such as density and shape (e.g., [83, 119, 120]), and there is substantial evidence that the constitutive behavior of even dry particle flows (granular flows) depends nonlinearly on the components in the mixture (e.g., [75, 121, 70, 92]). Some have suggested that for predicting the dynamics of a granular-fluid flow in general, or a debris flow in particular, a particle size representative of a debris flow or of a region of interest be used [2, 102, 114]. For mixtures of different sized particles, the expression for λ (Equation 4.2) is also ambiguous, as $\nu_{s,max}$ is extremely sensitive to the particle size distribution (e.g., [116, 70, 92]). Dimensional analysis by Iverson [2] suggests it is appropriate to replace λ with $\nu_s/(1-\nu_s)$. Others (e.g., [102, 45]) have used ν_s as a substitute for λ^2.

An additional uncertainty in the application of Equation 4.1 to debris flows involves the functional dependence of the normal stress (σ_{Bag} in Equation 4.1) on $\dot{\gamma}$, in the presence of interstitial liquids. Many (e.g., [63, 122]), including Bagnold [11] himself, suggested that for particle-fluid mixtures the power law dependence of stresses on $\dot{\gamma}$, is somewhat less than quadratic. Hsiau and Jang [122] suggested that the dependence of stress on $\dot{\gamma}$ varies if the granular temperature (or the variance of the particle velocities in a granular flow or granular-fluid flow) is non-constant, which is true for segregating mixtures [121]. Stock and Dietrich [102] addressed this uncertainty in the dependence of stress on $\dot{\gamma}$ by allowing dz/dt to vary as $\dot{\gamma}^w$, where w must be determined by the nature of the flow.

Data from physical experiments using small and large drums [46, 114] support the bedrock incision relationship proposed by Stock and Dietrich [102]. In particular, Hsu et al. [46] showed that incision rates into erodible basal panels in a 0.56m diameter drum depended on grain size and bed material tensile strength in a manner similar to that predicted by Stock and Dietrich [102]. In a 4m diameter instrumented drum, Hsu

[114] simultaneously monitored the mean and dynamic loads on the bed and bedrock incision, from which she concluded that impact wear dominates incision in both dry granular flows and liquid-poor granular-fluid flows. Further, Hsu [114] showed that this wear is associated with large excursion forces and that the local variance of the force plate outputs increased roughly as the square of D_{84}. In the presence of moderate-to-high concentrations of interstitial fluids such as water and mud, Hsu [114] found that sliding wear also becomes important in the erosion of relatively low tensile-strength bedrock substrates. In this chapter, we focus on the dynamics of liquid-poor granular-fluid flows, typical of debris flow fronts, that we consider well-represented by dynamics in granular flows. We consider primarily those dynamics relevant to the incision of high tensile strength bedrock found in nature and for which Equation 4.3 is most relevant.

To summarize, two key assumptions of the Stock and Dietrich [102] debris flow incision model (Equation 4.3) supported by experimental investigations [46, 114] are: 1) excursions in collisional stresses at the coarse front drive bedrock incision for the majority of rock strengths found in nature, and 2) these collisional stress excursions scale with the square of a representative grain size in the coarse front. Although the drum experiments by Hsu [114] support these two assumptions, the data do not reveal how, theoretically, to calculate excursion stresses or the grain size dependency of these stresses. We propose that an important next step toward building a mechanistic and predictive model for bedrock incision by rocky debris flows, debris flow snouts, and other fluid starved granular flows involves determining how the excursion stresses and the collisional forces scale with grain size distribution and flow dynamics.

To address this, we use Discrete Element Method (DEM) simulations (first proposed by Cundall and Strack [38] to explore controls on boundary forces generated by granular flows. This approach is well-suited for dry granular flows, which we suggest represents salient features of the coarse front of even muddy debris flows, and has the distinct advantage over continuum models in explicitly predicting the dynamics of individual particles. There are several benefits to using this type of simulation. Segregation dynamics that concentrate large particles toward the flow front emerge spontaneously in the simulations, so there is no need to impose an empirical model for segregation. Further, the collective and individual impact processes of the particles on the boundaries can be directly monitored and related to other variables such as local and system-wide

measures of particle size distribution (e.g., [22, 75, 121, 70, 92]).

4.2 Computational simulations and experimental comparisons

4.2.1 Discrete Element Method (DEM) simulations

For our simulations we use the Discrete (or Distinct) Element Method (DEM) [38] in 3-d. Our particle-particle and particle-wall contact forces are represented using a non-linear force model based on Hertzian and Mindlin contact theories (e.g.,[39], [40] [41], [42]), a damping component based on the derivation outlined by [42], and the Coulomb friction law. (See Chapter 1 for details).

We choose the material properties based on those associated with the material comprising the particles used in the experiments. These were determined prior to any comparison with the experiments and thus were not arrived at using calibration with the drum experiments. We use particles with the following properties typical of quartz: material density $\rho = 2650$ kg/m^3; modulus of elasticity $E = 29$ GPa; Poisson's ratio $\nu = 0.15$, and coefficient of friction (between particles) $\mu = 0.5$. The corresponding coefficient of restitution $e \approx 0.89$. The values of k_n, k_t, η_n, and η_t we derive from these material properties vary with the sizes of the particles involved in a particular collision (as in [42]). We choose particle sizes in the simulations according to the sizes of spherical marbles used in the physical experiments: d =13.8 mm, 25.0 mm, 34.0 mm, 40.0 mm, and 50.0 mm. We include the parameters for contacts between two different sized particles in Table 4.1, $d = 13.8mm$ and $d = 50.0\ mm$.

4.2.2 Experimental drums and simulated drums

We performed the experiments and simulations we describe here in rotating drums. Admittedly, the boundary conditions of a drum are somewhat different from those of a typical debris flow in the field; specifically, the base of a model debris flow in a drum is curved so the effective slope changes relatively quickly compared to a debris flow in the field. We consider the front of the flow in the drum most similar to the front of the flow of a debris flow in the field. Distinct advantages of using drums arise from the fact that

the material is recirculated, facilitating continuous and reproducible measurements of dynamic quantities including boundary pressures and detailed characterization of grain scale segregation.

We performed our experiments in either a small physical drum of (diameter D = 0.56 m; width W = 0.15 m), described in detail by Hsu et al. [46], or a large physical drum (D = 4 m; W = 0.8 m), described in detail by Hsu [114] (Table 4.3). We modeled most of our simulations after experiments in the small physical drum for which the essential details are as follows. The front vertical wall is made of clear acrylic, and the surface profile and particle locations adjacent to the wall can be captured with a digital camera. The vertical side walls are relatively smooth. For these experiments, the drum bed was roughened with sandpaper to reduce sliding of the particles along the bed. The main advantage of using this drum regards the small number of (spherical) particles used in the experiments which allows us to reproduce the experimental conditions in our simulations and complete the simulations in a reasonable amount of time.

In the large physical drum, the vertical walls are smooth, but the drum bed over which the particles move is equipped with treads of a 25 mm square cross-section that span the width of the drum. The treads were installed at 6 intervals (i.e., every 21 cm) with one exception in each quadrant. In three quadrants there is a 60 cm span without treads where samples of bedrock substrate are housed for incision experiments. In the fourth quadrant, there is a span missing three treads in the immediate vicinity of a 15 cm $\times$ 15 cm steel load plate attached at the center of the drum bed to an Interface Force Model SWP10-5KB000 Precision Force Transducer. The instrumented system was designed in-house by engineers at the University of Minnesota St. Anthony Falls Laboratory. The force recorded by the force sensor at any given time is the sum of all forces associated with particle-sensor contacts. The force is recorded at a frequency of 200kHz; these data are averaged over 1 ms intervals. Because this force is typically due to several simultaneous particle-bed contacts over the sensor area, we report this information in terms of a pressure, calculated by dividing the measured force by the area of the sensor. Because of the size of the drum and the amount of material needed for experimental flows, we performed experiments in this large physical drum using naturally occurring aspherical gravel particles rather than manufactured spheres.

We performed simulations with one of two computational drums designed to reproduce the salient boundary conditions of the physical experiments (Table 4.3). Our model for the small physical drum, the smooth computational drum, has the same dimensions as the small physical drum. The bed of the model drum is physically smooth, and the particlebed frictional coefficient $\mu_{pb} = 0.7$ is slightly greater than that between particles to account for the additional friction associated with the sandpaper in the small physical drum. Snapshots from a simulation with this drum are in Figs. 4.1(a) and (c).

In our model for the large physical drum, the "bumpy computational drum," we "installed"treads and a force sensor along the boundary, similar to those in the large physical drum. However, precise DEM simulations of the large physical drum are prohibitively computationally expensive due to the asphericity of the particles used for these experiments and the sheer number of particles. The duration of a simulation increases by ap proximately approximately NlnN, where N is the number of particles, and, although there are a number of methods available for simulating aspherical particles, these typically take significantly more time [123, 124]. Therefore, we use spherical particles in the bumpy computational drum, and the drum has the dimensions of the small physical drum (0.56 m $\times$ 0.15 m). The simulated treads are comprised of 7-mm-diameter semi-circular cylinders that span the bed, scaled down from the height of the treads in the large physical drum according to the ratio of the drum diameters. As in the large physical drum, the treads are fixed to the bed at regular 6^{o} intervals, except in the region of the simulated force plate. Force sensor data are produced from the simulations by summing the forces associated with particle.bed contacts in the $4.3^{o}\times$ 15 cm region lacking treads (Fig. 4.1(b)). Snapshots from a simulation using the bumpy computational drum are shown in Fig. 4.1(b) and Fig. 4.1(d). We address the issues of scaling the simulations to physical experiments in Section 2.3.

To produce thin flows characteristic of debris flows, for each experiment we fill only a small fraction our drums with particles (fill levels of 3.3% - 7.0%, Fig. 4.1). The particle movement in our drums, described in detail by Hsu [114], is similar to that at the front or snout of debris flows in the field as reported by Swartz and McArdell [125]. Particle trajectories in both the physical and computational drums follow a similar 3-dimensional circulation pattern: particles at the bed and walls are dragged upstream and then flow down the top surface of the flow toward the front. When viewed from

the side, the flow exhibits a shear zone between the upstream and downstream moving particles, and the shear rate is non-zero throughout the entire depth. When viewed from the top, the particles on top move toward the side walls at the front of the flow. In a mixture of different sized particles, individual particle trajectories vary with particle size giving rise to an overall segregation of the particles from the front to the back of the flow. Large particles tend to circulate near the flow front, and the larger the particles, the more their trajectories are restricted to the front. Smaller particles tend to circulate near the middle and back of the flow.

The flow of particles does not vary significantly from one drum to the next: The gravel flows in the large physical drum are similar to flows of spherical particles in the small physical drum and the two simulated drums; The flow depth to drum diameter ratio is the same when the fill fraction is the same, and casual observation of the particles in motion in the small and large physical drums indicate that the average particle motion is not affected much by the treads. However, there are some minor differences that are worth noting among the different systems. The simulation results indicate that the treads in the bumpy computational drum reduce the slip velocity adjacent to the bed and give rise to a flatter surface profile (e.g., compare Figs. 4.1(a) and (b)). Additionally, since the diameter of the large physical drum is nearly an order of magnitude larger than that of the small drums, and we used similar sized particles in all drums, the flow depth to particle size ratio was much greater in the experiments we performed in the large physical drum than in any of the smaller drums.

4.2.3 Quantitative comparisons of the dynamics in the experimental and simulated drums

We compare results from two sets of experiments and simulations whose parameters are summarized in Table 4.4.

From the first set of runs, we compare surface profiles and segregation behavior measured in the small physical drum with those in the smooth computational drum. Figure 4.2(a) shows instantaneous surface profiles measured from experiments (top) and simulations (bottom) for 13.8 mm particles. Each trace in both figures represents the surface profile for one of several drum rotations. The similarity of the experimental and computational profiles indicates that the internal stresses of the bulk flow are likely

well-represented by the DEM simulations. Figure 4.2(b) shows some results from simple segregation experiments and simulations using systems of primarily 13.8 mm spherical matrix particles and a single larger intruder particle. Figure 4.2(b) illustrates typical longitudinal positions of relatively large intruder particles using a probability distribution (pdf) of the intruder particle in each case. The plots indicate that, for all cases, the large particles spend the majority of their time toward the flow front, though this tendency decreases for a smaller intruder particle. Such behavior of large particles is similar to that observed in large-scale debris flows having a much wider particle size distribution (e.g., [126, 2]. (See Fig. 4.3 for other sizes of intruder particles). The similarity between the experimental and simulation results is further demonstrated by the similarity of the mean and standard deviation of the location of intruder particles 4.4. Despite close similarities, there are a few noteworthy differences between the experimental and computational results in Fig. 4.2(b). The experimental results are somewhat noisier and the peaks are broader than the simulation results. We propose that these differences are primarily due to the fact the simulations cannot perfectly reproduce the behavior of particles that are slightly aspherical and have asperities. Other potential causes for differences between experiments and simulations involve slight imperfections in the experimental drum, including an imperfect circular boundary. However, the simulations appear to adequately reproduce the segregation trends observed in the physical experiments.

The speed of rotation also affects the location intruder particles. Fig. 4.5 shows the pdf of the location of a 50mm intruder particle at different speeds of drum rotation speeds ω. As ω increases the peak of the pdf shifts towards the back of the flow. The shape of the pdf also changes to a symmetric shape as ω is increased. The mean location increases linearly with ω (Fig. 4.6).

We use the second set of runs to compare boundary pressures in the large physical drum with those in the bumpy computational drum (Figs. 4.2(c) and (d)). We calculate the simulated force plate measurements by considering the particle.bed forces over a time interval of 1 ms, which corresponds to analogous measurements by the physical force sensor. We report the results in terms of a pressure p_4, where the subscript "4" refers to the approximate angle over which the sensor extends ($\approx 4.3^{\circ}$) and thus the angle over which the averaging takes place (calculation details are shown in Appendix B.) All

data shown in Fig. 4.2(c) corresponds to one pass of the force sensor along the bottom of the debris flow. The top panels contain the "raw data". The middle panels of Fig. 4.2(c) contain the data from the plots of $p(\theta)$ averaged over 1^o bins, $\overline{p}_4(\theta)$. (Here and henceforth, a line over any variable q, such as q indicates a temporal average as indicated in the calculations.) The bottom panels in Fig. 4.2(c) contain the standard deviation of $p(\theta)$ for each 1^o bin, which we denote $p_{4,\sigma}$. Despite the differences between the results from the simulations and the physical experiments, the profile of the mean normal stress p_4 is convincingly similar. This is particularly apparent when these pressure data are scaled by the total mass (M) in each drum and the area (A) of the relevant sensor: $\overline{p}_4^* = p_4 \times A/Mg$ (Fig. 4.2(d)).

Certain differences in the two data sets appear related to the size difference of the two drums. For example, the standard deviations of the normal boundary stresses in each 1^o bin are similarly noisy, but the noise does not scale with M. The measures of the stress fluctuations are relatively larger in the smaller simulated drum than in the larger experimental drum. We attribute this difference in stress fluctuations to the difference in the sensor size relative to the particle size (smaller in the simulations than in the physical experiments). Specifically, the scale of particle size to the force plate influences the number of contacts on the plate and therefore the force distribution (e.g., Jalali et al. [127]). Furthermore, the larger the force sensor relative to the particle size, the less the force sensor is capable of capturing individual particlebed collisions. Thus, increasing the size of the force sensor relative to the particle size reduces the effect of individual impacts on the average pressure, effectively smoothing the effect of large (or small) impacts on the pressure calculations. This discrepancy would likely have been alleviated in part had we used a larger area for the force sensor in the simulations, but this would cause other problems. A model sensor length equivalent to that in the experiment (15cm) would span 31^o of the simulated drum. As we will show in Section 3.1, the particle size distribution changes substantially over this angular distance, so the results would not capture local effects so much as global system effects. Thus we accept the different scale of the measured fluctuations in the physical experiments and simulations and use the simulations to understand how measures of contact forces such as local pressures, mean contact forces, and contact force variances vary relative to one another with change in particle size distribution rather than deriving an absolute

measure of the fluctuations.

Additional scaling effects associated with the drum width and tread height may also influence the simulation results. For example, the scaled down treads in the simulations relative to the particle size could allow more slip of the particles relative to the bed. In particular, if the treads are too small compared to the particle size, they do not effectively reduce particle slip as the particles "see" them essentially as negligible roughness elements. However, in our simulations the treads were sufficiently large to reduce boundary slip, so we assume the simulated ridges have the same effect on the flows as the ridges in the physical experiments.

Having confirmed that the dynamics of the particles in the physical drums (e.g., height profiles, segregation details, and boundary forces) are represented relatively well by those in the simulations, we next systematically investigate the effects of particle size distribution on boundary stresses using our simulations.

4.3 Force and stress variability associated with binary mixtures and monosized systems

4.3.1 Simulated mixtures

To systematically investigate the effect of particle size distribution on particle-bed forces, we performed several simulations in the smooth computational drum using different combinations of the same particle sizes used in the validation experiments and simulations. In each case $\sim$ 4.3 kg of particles were rotated at 6 rpm in the smooth computational drum. The simulations were run for three minutes (of computational time), and the contact force data were obtained at a frequency of 75Hz. The results do not change significantly when the simulations are run for a longer period of time. We focus first on two monosized systems (13.8 mm particles, and 25.0 mm particles) and four binary mixtures comprised primarily of 13.8 mm particles with different numbers of larger particles (25.0 mm or 50.0 mm). We refer to the mixtures with one, four and eight 50.0 mm particles as Mix1_{50}, Mix4_{50}, and Mix8_{50}, respectively, and the mixture with ninety-nine 25.0 mm particles as Mix99_{25} (Table 4.5).

Snapshots of simulations of the 13.8 mm particles alone, Mix1_{50}, Mix4_{50}, and Mix8_{50}

(Fig. 4.7) reveal some basic details of the flow. In all four simulations the larger particles spend most of the time at the very front of the flow. The flow is shallow enough so that the large particles protrude from the top. As the number of 50.0 mm particles increases both the local average particle size and the length of the region frequented by 50.0 mm particles increases.

The mass-averaged local particle size $\overline{d}(\theta)$ (please see Appendix B for calculations) illustrates quantitatively the variability of the particle size distribution along the bed (Fig. 4.8). Admittedly, compared to some other measures of representative grain size (e.g., the median grain size) the use of $\overline{d}(\theta)$ has the disadvantage that there is typically no representative particle size of exactly that value in our mixtures. On the other hand, the local average energy and impulse imparted on the bed (hypothesized as important for bedrock incision by Sklar and Dietrich [104, 114] scale with the local average particle size. In Fig. 4.8 we plot $\overline{d}(\theta)$ for the four systems illustrated in Fig. 4.7. As indicated in the snapshots in Fig. 4.7, 50.0 mm particles congregate towards the front of the flow, raising the mean size there. This region of increased $\overline{d}$ increases with increasing numbers of 50.0 mm particles in the mixture, corresponding to a longer region frequented by the larger particles. For all cases, the maximum value of $\overline{d}$ is located near the front of the flow and decreases with distance toward the tail until a point is reached where no 50.0 mm particles travel during the course of the simulation. We note that there is a distinct oscillation in $\overline{d}$ vs. θ, particularly for Mix8_{50}. The wavelength of the oscillations is ~ 50 mm indicating some degree of ordering of the 50.0 mm particles relative to one another, a unique feature of relatively uniform particles.

4.3.2 Normal boundary stress or pressure, p

To determine how the boundary pressure varies with local particle size distribution, we calculate the local average pressure $\overline{p}(\theta)$ at 1^{o} intervals along the drum bed. As detailed in Appendix B, we do so by summing the normal contact forces within a 1^{o} bin centered at θ and dividing by the area of that degree bin. Plots of $\overline{p}(\theta)$ (Fig. 4.9) for the four systems simulated systems shown in Fig. 4.7 are essentially the same, except for a few bumps near the front that correspond to locations where the larger 50.0 mm particles spend more of their time. These data indicate that the local time-averaged pressure is independent of the local particle size distribution and likely dependent only

on the distribution of total mass. To test this interpretation, we calculate the normal stress associated with the weight of the particles, $\overline{p}_w(\theta)$, analogous to the hydrostatic or lithostatic pressure in a continuous system (as detailed in Appendix B).

For all mixtures $\overline{p}(\theta) \approx \overline{p}_w(\theta)$ along the entire length of the flow with some relatively minor exceptions (Fig. 4.9). The similarity in the two sets of data for each mixture extends to the degree of bumpiness corresponding to the average location of 50 mm particles. Comparing these results to the $\overline{d}(\theta)$ data in Fig. 4.8, we conclude that the average normal stress at any point along the boundary is nearly independent of the local and global particle size distribution, except as the particle size distribution governs the distribution of the system mass.

Fig. 4.10 shows $\overline{p}$ for Mix1_{50} for various values of ω. The flow profile and $\overline{p}$ do not change significantly with change in ω. At the front of the flows there is a systematic change, though minor. In the rest of this chapter we will use $\omega = 12$rpm.

It is interesting to consider Bagnold's classic model for collisional stress (Equation 4.1) in light of these results. Bagnold [11] suggested that the mean normal stress $\overline{p}$ is equal to the mean collisional stress. In free surface flows such as ours, the mean normal stress may also be determined from the lithostatic pressure. Considering this in Equation 4.1, implies that the shear rate, $\dot{\gamma}$, is determined by $\overline{p}$ and d. So long as the particle mass is distributed similarly from one system to the next, then, it makes sense that $\overline{p}$ does not change from one system to the next. Then, if Equation 4.1 holds, as particle size d increases $\dot{\gamma}$ should decrease. For deep flows, this decrease in $\dot{\gamma}$ has been reported, for example, in experiments by Hill et al. [84] and simulations by Rognon et al. [75].

Although the variation in $\overline{d}(\theta)$ does not correlate with a noticeable variation in $\overline{p}(\theta)$ in the simulations, there is credible experimental evidence that a higher fraction of larger particles increases the rate of bedrock incision by granular flows (e.g., Hsu et al. [46, 114]). Based on these results, we hypothesize that incision by granular flows is not directly associated with the average boundary pressure, but instead is related to the cumulative effects of individual particlebed collisions as suggested for bedrock incision by fluvial processes by Sklar and Dietrich [128, 104]. Therefore, we focus next on statistics of the individual particlebed contact forces and how they depend on local and global particle size distribution.

4.3.3 Spatial variability of collisional contact forces: Probability distribution functions

The probability distribution function (pdf) of the forces provides a general picture for the variability of normal particlebed contact forces. In Fig. 4.11 we plot pdfs from a few distinct regions of the bed, as noted, for the 13.8 mm uniform system (Fig. 4.11(a)) and the Mix8_{50} system (Fig. 4.11(b)). For both systems, there is a higher probability of large forces toward the front of the flow (e.g., from θ = -10$^{\text{o}}$ to -5$^{\text{o}}$) than toward the back (e.g., from θ = 30$^{\text{o}}$ to 35$^{\text{o}}$), though the difference is much smaller in the 13.8 mm system (Fig. 4.11(a)) than in the Mix8_{50} system (Fig. 4.11(b)). This indicates that the presence of large particles among the small particles has a significant effect on the variability of the forces along the boundary. The shape of the pdfs cannot be described by a simple function, such as a single power law or exponential. Therefore, for simple measures of how the forces vary with particle size distribution, we consider certain basic statistics of the forces associated with particlebed contacts and how these vary in our simulated mixtures in the next subsection.

4.3.4 Local force variability and local average particle size

We calculate three basic statistics of the particle-bed contact forces within each 1$^{\text{o}}$ bin: the mean contact force, $\overline{f}(\theta)$, the standard deviation of the force per contact, $f_\sigma(\theta)$, and a measure of the maximum contact force, $f_{max}(\theta)$. The calculations for $\overline{f}(\theta)$ and $f_\sigma(\theta)$ are detailed in Appendix B. For a representative local maximum contact force $f_{max}(\theta)$ we average the top 0.1% of forces within each degree bin. We performed the same calculation for percentages ranging between 0.1-5% and found that as the percentage value increases, the representative maximum force calculated in this way approaches $\overline{f}(\theta)$), but the functional dependence of the representative force on mean particle size is unchanged.

In Figs. 4.12(a)-(c) we show that $\overline{f}$, f_σ, and f_{max} vs. θ, all peak near the flow front and decrease toward the tail. However, unlike $\overline{p}(\theta)$, the scaling varies considerably from one mixture to the next, particularly near the flow fronts where $\overline{d}(\theta)$ varies most dramatically from one mixture to the next. For the 13.8 mm monosized system, there is a sharp peak in each of $\overline{f}$, f_σ, and f_{max} associated with the flow front (θ = -10$^{\text{o}}$ to

-5°). For $Mix1_{50}$, $Mix4_{50}$, and $Mix8_{50}$, the peaks in $\overline{f}$, f_σ, and f_{max} near the flow front are progressively larger as the number of 50.0 mm particles in the mixture increases. Additionally, the peaks are broader and extend farther back in the flow with increasing numbers of 50.0 mm particles. The values of each measure of the contact forces for the different mixtures eventually drop to the values of the 13.8 mm system. In each case this happens at essentially the same position at which $\overline{d}$ drops to 13.8 mm (See Fig. 4.8).

We suggest that there are two possible causes for the variability of the contact force statistics. The first involves the dynamics at the flow front. In both the physical experiments and the simulations, the flow is noticeably more disordered and highly collisional at the front and more fluid-like and frictional toward the tail. We hypothesize that the effect of multiple particles colliding violently at the flow front results in larger contact forces, an effect described previously in the literature (e.g., [2, 102, 129]). The second factor evident in the contact force statistics (Fig. 4.12) is the simultaneous variation of the forces and the local average particle size $\overline{d}$. To isolate the variability of the force statistics associated with d from those associated with change in phase (collisional to frictional) or slope, we consider data in the central region of the flows ($40^o > \theta >$ -10°). Specifically, we do not consider the data near the flow front ($\theta <$ -20°) where the flow is clearly influenced by the disordered, gas-like dynamics and the flow height is highly spatially variable. Also, we do not consider the data too near the rear of the flow ($\theta > 40^o$) beyond which there are no large particles ($\overline{d} = 13.8$ mm), and the dynamics change due to an unreasonably high bed slope.

Parametric plots of the force statistics as a function of grain size from Figs. 4.8 and 4.12 for -10° $< \theta <$ 40°. (Fig. 4.13) show significant overlap between the data from the $Mix4_{50}$ and $Mix4_{50}$ systems. These results indicate that the local average particle size $\overline{d}$ plays a significant role in determining the force statistics $\overline{f}$, f_σ, and f_{max}. In all cases, there is a clear monotonic relationship between local average particle size and local measures of the forces between particles and the boundary. The data for the average and maximum forces $\overline{f}(\overline{d})$ and $f_{max}(\overline{d})$ are nearly equivalently well-fit with exponential and power law relationships, whereas the data for $f_\sigma(\overline{d})$ are better fit with an exponential curve, using linearized least-square analysis (Table 4.6). Both fitting results indicate that $\overline{f}$ varies approximately linearly with $(\overline{d})$; f_{max} varies somewhat

faster with $\overline{d}$, and f_σ varies much more slowly with $\overline{d}$.

We note that it is not surprising to find a monotonically increasing dependence of the average and maximum contact forces on the local average particle size. For instance, we can relate the force $\overrightarrow{F}$ associated with a particular collision between a particle and the boundary to the impulse or average rate of momentum change of the particle $\Delta(\overrightarrow{mv})$: $\overrightarrow{F} = \Delta(\overrightarrow{mv})/\Delta t$, where m is the particle mass, and Δv is the difference between the velocity before and after the collision. This suggests that as long as Δt (the collisional contact time) does not vary too much with particle size, the impulse should have a monotonically increasing dependence on d (considering, for example, that particle mass $m \sim d^3$). Thus, increasing the number of large particles in a mixture increases the number of large impulses, subsequently increasing average particlecontact force (explored in more detail in Section 4).

We now examine the influence of the globally-averaged particle size compared to the influence of the locally averaged particle size on the particle.bed contact force statistics. To do so, we look at the variability of the force statistics in two pairs of mixtures with similar globally-averaged particle sizes, d_{sys} (Appendix B). In particular, for both Mix99_{25} and Mix4_{50}, $d_{sys} \approx 20$ mm. For Mix8_{50}, $d_{sys} \approx 25$ mm, comparable to the system of 25.0 mm particles alone. The front-to-tail sorting varies from one mixture to the next, even for mixtures of equal average particle sizes (Fig. 4.14(a)). Specifically, Mix4_{50} and Mix8_{50} have a more significant variability of $\overline{d}(\theta)$ than does Mix99_{25} (and trivially, there is no size variation for the system comprised solely of 25.0 mm particles). On the other hand, $\overline{d}(\theta)$ is greater farther back along the bed for Mix99_{25} and the system of 25.0 mm particles. As a result $\overline{f}$, f_{max}, and f_σ (Figs. 4.14 b, c, and d) are all high farther back in the flow for both Mix99_{25} and the 25.0 mm monosized system compared with those of Mix4_{50} and Mix8_{50}. In contrast, relatively high values of $\overline{d}(\theta)$ correspond to large values of f_{max} at the flow fronts for Mix4_{50} and Mix8_{50}.

Similar to Mix4_{50} and Mix8_{50}, a flow of Mix99_{25} exhibits clear monotonic relationships between each statistical measure of the contact forces and the local average particle sizes (Fig. 4.15). The various force statistics exhibit both power law and exponential relationships with $\overline{d}(\theta)$, similar to those exhibited for the mixtures of 13.8 mm and 50.0 mm particles (Table 4.6). However, the dependence of the force measure on $\overline{d}(\theta)$ for

$Mix99_{25}$ is stronger than that for $Mix4_{50}$ and $Mix8_{50}$, as evidenced by the higher values of the parameter in the exponent and the power of these relationships (Table 4.6). These differences are even more apparent when these two sets of data are plotted side by side (Fig. 4.16). For all values of the local average particle size $\overline{d}$, $\overline{f}$ and f_{max} are greater for $Mix99_{25}$ than for $Mix4_{50}$ and $Mix8_{50}$.

In summary, local measures of particlebed forces depend solely on the local average particle size of different mixtures of the same two particle sizes (Fig. 4.13). However, if one of the particle sizes in a mixture is changed, the functional dependence of the local measure of particlebed forces on local average particle size changes significantly (Fig. 4.16).

4.3.5 Variations of system force statistics with system particle size distribution

Next, we consider how various system-wide force statistics depend on d_{sys} for each mixture or system of particles. We do so for the sets of mixtures described above (Table 4.5) and other mixtures of 13.8 mm and 25.0 mm particles and of 13.8 mm and 50.0 mm particles, all having a total mass 4.3 kg. For each mixture, we calculate the average bed forces over the whole system, $\overline{f}_{sys}$, and the variability in terms of the standard deviation of the forces in the entire system $f_{\sigma,sys}$ (Appendix B). We also compute $f_{max,sys}$, the average of the highest 0.1% contact forces across the entire bed. For each set of mixtures, $\overline{f}_{sys}$ (Fig. 4.17a),$f_{\sigma,sys}$ (Fig. 4.17b) and $f_{max,sys}$ (Fig. 4.17c) increase approximately exponentially with d_{sys}. Similar to the local force statistics (Fig. 4.16), the system-wide force statistics for the 13.8 mm and 25.0 mm mixtures are more sensitive to a change in average particle size than the analogous statistics for the 13.8 mm and 50.0 mm mixtures (Table 4.7). Furthermore, for the same average mixture size, $\overline{f}_{sys}$, $f_{\sigma,sys}$ and $f_{max,sys}$ are typically larger for the 13.8 mm and 25.0 mm mixtures than they are for the 13.8 mm and 50.0 mm mixtures (Fig. 4.17).

4.4 Particle size dependence of the boundary forces: Particle-scale mechanics

To understand the particle size dependence of the boundary forces due to granular flows, we consider the dynamics of the particlebed impacts at the particle scale. In particular, we focus on the dynamics of an isolated particle impacting a bed with an impact velocity v_i. Immediately after the impact, the contact force between the particle and the bed increases and the particle velocity decreases, until the particle stops, reverses direction, and begins to rebound. At that time, the deformation associated with that particular particlebed interaction, δ_n in Equation 4a, has reached its maximum value $\delta_{n,max}$. As the particle rebounds; the particle center moves away from the boundary, and the contact force gradually decreases with δ_n until $\delta_n = 0$ and the particlebed contact is broken.

To illustrate typical force scales of this interaction, we plot the temporal dependence of the contact force for a collision between a 25 mm particle and the fixed boundary for three different values of v_i (Fig. 4.18). The total duration of each collision is on the order of 10^{-4} seconds, indicative of our use of relatively hard particles [70, 92]. We use the maximum contact force $f_{c,max}$ as a representative force scale for each collision and plot $f_{c,max}$ as a function of v_i from simulations using three different sized particles, 13.8 mm, 25.0 mm, and 50.0 mm (Fig. 4.19). We find that for a given particle size $f_{c,max} \sim v_i^{1.2}$, and for a given value of v_i we find that $f_{c,max} \sim d^2$.

The contact model (Equation 4a) provides a means for obtaining a relatively simple theoretical expression for the maximum contact force: $f_{c,max,cm}$. Neglecting the damping force and the gravitational force, the maximum force per contact is $f_{c,max,cm} = k_n \delta_{n,max}^{3/2}$. To determine how this expression varies with d and v_i, we consider separately the functional forms of the force parameter k_n and the maximum deformation from the contact model $\delta_{n,max,cm}$. According to Hertzian contact theory, for contact between a particle of diameter d and a flat bed,

$$k_n = \sqrt{\frac{2d}{9}} \frac{E}{1-\kappa^2} \tag{4.4}$$

provided that both the bed and particle have the same modulus of elasticity E and Poissons ratio κ.

To find $\delta_{n,max,cm}$ we equate the kinetic energy loss of a particle of mass m and impact velocity v_i to the energy required for the particlebed deformation from the time of initial contact to the time of maximum deformation, neglecting the damping force and the gravitational force in Equation 4a. In this case, for a particlebed overlap (or deformation) equal to x, the energy associated with an additional incremental deformation of dx is $k_n x^{3/2} dx$. Equating the kinetic energy loss during the entire deformation process to the energy associated with the total deformation gives:

$$-\frac{1}{2} m v_i^2 = -\int_{x=0}^{\delta_{n,max}} k_n x^{3/2} \, \mathrm{d}x. \tag{4.5}$$

where $\delta_{n,max,cm}$ refers to the maximum overlap predicted by the contact model. Integrating and rearranging this expression gives an explicit function for $\delta_{n,max,cm}$:

$$\delta_{n,max,cm} = \left(\frac{5}{4} \frac{m v_i^2}{k_n} \right)^{2/5} \tag{4.6}$$

Using $m = \rho \pi d^3/6$ and k_n from Equation 4.4, we find

$$\delta_{n,max,cm} = \left[\frac{15}{4\sqrt{2}} \frac{\rho \pi v_i^2 (1-\kappa^2)}{E} \right]^{2/5} d \tag{4.7}$$

Considering Equations 4.4 and 4.7, the maximum force per contact predicted by the contact model $f_{c,max,cm}$ may be written in terms of the particle material properties and diameter as:

$$f_{c,max} = \frac{\sqrt{2}}{3} \left(\frac{15\pi}{4\sqrt{2}} \right)^{3/5} \left(\frac{E \rho^{3/2}}{1-\kappa^2} \right)^{2/5} v_i^{1.2} d^2 \tag{4.8}$$

We note that the power law dependencies of $f_{c,max,cm}$ on v_i and d are the same as those obtained from the simulation data (Fig. 4.19). This expression for $f_{c,max,cm}$ can be used to estimate the scaling of the average system boundary stresses with average particle size in a binary mixture of particles of two sizes d_1 and d_2. We simplify the problem by assuming that the number of contacts by each type of particle is exactly proportional to its number representation in the mixture and that all of the particles have the same impact velocity. From Equation 4.8, we can express a theoretical system average force $f_{th,sys}$ based on only the maximum forces per contact as

$$\overline{f}_{\mathrm{th,sys}} = \alpha \frac{\sqrt{2}}{3} \left(\frac{15}{4\sqrt{2}} \rho \pi v_i^2 \right)^{3/5} \left(\frac{E}{1-\kappa^2} \right)^{2/5} \frac{N_1 d_1^2 + N_2 d_2^2}{N_1 + N_2} \tag{4.9}$$

where α relates the time-averaged force for a particular particlebed contact to the maximum force of that contact (assumed here to be a constant parameter); N_1 and N_2 are the assumed numbers of contacts associated with two types of particles, proportional to the number of particles of each type. We calculate the results for several different mixtures consisting of one of the two sets of particles: (1) $d_1 = 13.8$ mm and $d_2 = 25.0$ mm and (2) $d_1 = 13.8$ mm and $d_1 = 50.0$ mm. We use the same physical details as we use in our simulations: E=29 GPa, $\nu = 0.15$, $\rho = 2650$ kg/m^3, and total mass = 4.3 kg. We use an impact velocity of 0.14 m/s, which corresponds to the impact velocity of a particle released from a distance 1 mm above a horizontal surface, chosen somewhat arbitrarily based on the scale of the particles. The functional form of these results do not depend on this value. Finally, we use $\alpha = 1$, though in reality the number should be significantly smaller than one. We plot the results in Fig. 4.20.

Despite the many simplifications used to reach these theoretical results, they exhibit many of the same features as the results from the computational simulations (compare Fig. 4.20 with Fig. 4.17). $\overline{f}_{th,sys}$ depends monotonically and nonlinearly on d_{sys} as was the case for $\overline{f}_{sys}$ and $f_{max,sys}$. Further, for a particular value of d_{sys}, $\overline{f}_{th,sys}$ is higher for the mixture with 25.0 mm particles than that with the 50.0 mm particles. From the calculations described above, this is apparently due to the fact that each particlebed contact force scales with the size of the particle making contact with the bed. For any particular mixture, it takes considerably more 25.0 mm particles in the mixture of 13.8 mm and 25.0 mm particles than it does 50.0 mm particles in the mixture of 13.8 mm and 50.0 mm particles to give rise to the same averaged particle size $\overline{d} > 13.8$ mm. For example, for a mixture comprised of 13.8 mm and 25.0 mm particles where $\overline{d} = 24$ mm, approximately 180 out of 260 (63%) of the total number of particles are 25 mm particles, whereas for a mixture comprised of 13.8 mm and 50.0 mm particles where $\overline{d} = 24$ mm, approximately 7 out of 854 (1%) of the total number of particles are 50.0 mm particles. The dominance of 25.0 mm particles in the first mixture outweighs the effect of the greater force per impact of the 50.0 mm particles in the second mixture. Consequently the mean force $\overline{f}_{th,sys}$ is greater in the mixture of 13.8 mm and 25.0 mm particles. We hypothesize that this is also true with more realistic systems where particlebed contacts

are also influenced by collisions involving multiple particles simultaneously. It is not immediately obvious how to generalize these results to quantify the influence of particle mixtures using a more general description of particle size distribution. Instead, here we emphasize our result that a single measure of particle size for a mixture is not enough information to predict a mean particlebed force for a mixture. Notable quantitative differences between the plots of $\overline{f}_{th,sys}$ vs. d_{sys} (Fig. 4.20) compared with $\overline{f}_{sys}$ and $f_{max,sys}$ vs. d_{sys} (Fig. 4.17) pertain primarily to the magnitude difference between the theoretical and computational results. ($\overline{f}_{sys}$ and $f_{max,sys}$ are much smaller than $\overline{f}_{th,sys}$ for a particular value of d_{sys}.) This is likely at least in part due to our use of $\alpha = 1$ as a placeholder in Equation 4.9, and our choice of a constant value for v_i.

Comparing the scaling results from isolated particle-bed collisions with analogous quantities from the rotating drum simulations provides additional information regarding the relative importance of collective interparticle interactions on the statistics of the particle-bed forces. To do so, we calculate the maximum force and impact velocity associated with each contact between a particle and the drum from a few cases reported in Section 3: Mix1_{50}, Mix8_{50}, and 25.0 mm particles alone. For each case we plot the maximum force for each contact as a function of the normal component of the impact velocity, v_i, (Fig. 4.21) and superpose the relevant results from Fig. 4.19 onto these results. From these plots we see that the highest values of fc;max from the computational results exhibit the same power law dependence on v_i as do isolated particle-bed collisions and contact model predictions ($\sim v_i^{1.2} d^2$). Furthermore, when we consider the largest values of $f_{c,max}$ for Mix1_{50} and Mix8_{50} (Figs. 4.21(a) and (b), respectively), we note that the similarity between the results from these two systems indicates that the statistics of the largest forces considered in this way are essentially independent of interactions between multiple large (50 mm) particles. For the mixtures of 13.8 mm and 50.0 mm particles, Mix1_{50} and Mix8_{50}, there are two lines of data at higher values of v_i and $f_{c,max}$, one corresponding to each of the two particle sizes. The points on the branch corresponding to the 13.8 mm particles have considerably lower values of $f_{c,max}$ for the same values of v_i, consistent with the relationship $f_{c,max} \sim d^2$. For the 25.0 mm system (Fig. 4.21(c)) there is one line of data extending away from the origin consistent with the single size of particles in the system. For the smallest values of $f_{c,max}$ and v_i there is no clean functional relationship between $f_{c,max}$ and v_i which indicates that these forces are

largely associated with multiple particle collisions. The absence of points significantly below the power law relationships plotted in Fig. 4.21 indicates that, for nearly all values of v_i, multiple particle interactions serve to enhance, not buffer or decrease, the value of $f_{c,max}$ for a particular value of v_i. The spatial variation of these force statistics is shown for one mixture (Mix8_{50}) in Fig. 4.22. These results show that near the front of the flow where the particle-bed forces are the largest,the relationship $f_{c,max} \sim v_i^{1.2}$ for the 50.0 mm particles is the strongest; multiple-particle dynamics appear more dominant farther back in the flow where the particle-bed forces are relatively small.

The importance of isolated pure particlebed impacts in determining the largest boundary forces gives some indication of why our simple theoretical model for average particlebed forces has some qualitative success in predicting observed trends in $\overline{f}_{sys}$ vs. d_{sys} for different mixtures. Our model would be improved with information on how the distribution of the impact velocities depends on system parameters.

4.5 Discussion

Our results in Sections 3 and 4 provide some clear direction for bedrock incision models associated with debris flows. First, the temporally-averaged boundary normal stress profile of a granular flow depends primarily on the distribution of mass along the boundary and is essentially unrelated to the particle size distribution. Since experimental and field data show that the rate of bedrock incision by debris flows is dependent on particle size distribution of the particles comprising a debris flow [115, 46, 114], we conclude that the pressure associated with debris flow does not control the bedrock incision except as it influences the distribution of mass along the boundary.

Second, in contrast with the pressure results, the statistics of normal forces associated with individual particle-bed collisions do scale with particle size in a granular flow. Specifically, we have found that increasing the number of larger particles in a binary mixture *for mixtures of the same particle sizes and total mass*, gives rise to an increase in the mean force per contact, in the standard deviation of the mean force per contact, and in a representative maximum contact force. These relationships are qualitatively the same whether we consider local relationships between particle size and forces in small regions along the drum bed or the system-wide measures of the forces and particle size.

We have found that the size-dependence of the contact forces may be modeled by considering the contact mechanics of the particles. The associated scaling of the maximum particle-bed forces with particle size $f_{c,max} \sim d^2$ is consistent with a recently proposed bedrock incision model [102]. We conclude from this that the particle-bed contact force statistics rather than the pressure associated with the contact forces provides a more reasonable basis on which to build a mechanistically-based bedrock incision model for debris flows.

Finally, we consider the next steps for using our results from DEM simulations of granular flows as a guide in model development for bedrock incision from debris flows. In developing Equation 4.3, Stock and Dietrich [102] included an assumption that excursion forces that incise bedrock scale with a measure of the average collisional stress, specifically $K_0[cos\phi\rho\nu_s D_e^2\dot{\gamma}^w]^n$. Our simulation results suggest that this model could be linked to the mechanics of the particle dynamics by using the scaling for the largest impact forces. These scale with the square of the size of the largest particles as does the incision rate in the Stock and Dietrich [102] model. On the other hand, compared to a shear rate dependence in the Stock and Dietrich [102] model, our findings show that boundary forces scale non-linearly with impact velocity. In this context, an important next step for building an impact-based model for bedrock incision involves the development of a predictive form of a probability distribution function of impactor velocities as they depend on particle size distribution and other factors including debris flow depth and shear rate. For an alternative model for bedrock incision by debris flows, it is instructive to consider a model for bedrock incision into exposed bedrock in riverbeds proposed by Sklar and Dietrich [104] due to saltating bedload over exposed bedrock. They suggested that in this context, the bedrock incision rate can be expressed simply as the product of three terms: the average volume of rock detached per particle impact, the rate of particle impacts per unit area per unit time, and the fraction of the river bed made up of exposed bedrock. We could apply our results to a stochastic form of this model, but to do so we would need to develop a predictive form for the statistical distribution of impact velocities as well, particularly those sufficiently large to give rise to impact forces capable of removing bedrock

We conclude this section with three cautionary notes. First, we note that we have focused on quantities such as the statistics of $\overline{f}_{sys}$ and $f_{th,sys}$ but high values of either

does not necessarily correlate with high incision rates. More information is needed about the strength of the bed material before conclusions can be drawn. For example, while $\overline{f}_{sys}$ and $f_{th,sys}$ are typically larger for the mixtures of 13.8 mm and 25.0 mm particles than equivalent mixtures of 13.8 mm and 50.0 mm particles, the 50.0 mm particles still give rise to individual particlebed forces considerably larger than the 25.0 mm particles. If the strength of the bed material is sufficiently large, bedrock incision would still be greater for the mixtures of 13.8 and 50.0 mm particles than for mixtures of 13.8 and 25.0 mm particles. Fatigue due to repeated small collisions may also play a significant role. In other words, in addition to the force statistics one needs information about the material properties of the bedrock itself to fully develop a model for bedrock incision. Our second cautionary note involves the material properties of the particles themselves. The kinematics of softer particles in a granular flow are not the same as for harder particles in a granular flow. For example, the power law relationship between p and $\dot{\gamma}$ is reduced [61], and it is likely that the force statistics change accordingly (e.g., [70, 92] and references within). Therefore it is likely that our results would change for flows of softer particles. The third cautionary note involves the apparent dependence of impact velocity statistics on local particle size distribution and system dynamics. We note that while we have shown certain aspects of the particle size distribution and system dynamics separately determine certain aspects of the velocity and force statistics of impacting particles, the relationships are not independent. Additionally, the system dynamics determine details of the particle size distribution as well. For example, we found that the speed of drum rotation affects the location of large intruder particles. To demonstrate this, Fig. 4.5 (similar to the plots shown in Fig. 4.2(b)) shows the pdf of the location of a 50mm intruder particle at different drum rotation speeds ω. As ω increases the peak of the pdf shifts towards the back of the flow. The shape of the pdf also changes to a symmetric shape as ω is increased. The mean location increases linearly with ω (Fig. 4.6). Therefore, for a more fully predictive model of collisional debris flow incision, an understanding of the feedback between system dynamics and local particle size distribution in the setting of debris flows is also required.

4.6 Summary and future work

We used DEM simulations of dry granular flows in a drum to gain insight on bedrock incision associated with debris flows, particularly incision due to dynamics in the fluid starved front of debris flows. As we have demonstrated, Discrete Element Method (DEM) simulations are capable of producing, with no calibration, physically reasonable particle size distributions and boundary stresses associated with thin granular flows. This indicates that it is a reasonable tool for developing the distribution of impact velocities, collisional frequencies, impact forces, and other dynamics necessary for a mechanistic-based model for impact-driven bedrock erosion.

In particular, we used DEM simulations to investigate the parameters that determine normal stress and other statistical measures of the normal forces associated with sheared granular mixtures for insight into mechanisms associated with bedrock incision due to debris flows. We found that the normal stress or pressure profile along the boundary of a granular flow depends primarily on the distribution of mass along the boundary and is essentially unrelated to the particle size distribution. In contrast, we found that statistical measures of the contact forces (the mean impact forces, the standard deviation of the mean impact forces, and the maximum impact forces) depend strongly on the mean particle size. This is true for both the local dynamics and the global dynamics of a granular flow. Since experimental and field data show that the rate of bedrock incision by debris flows is dependent on particle size distribution of the particles comprising a debris flow [115, 46, 114], we conclude that the impact forces rather than the pressure (mean impact force normalized by area) must be mechanistically linked to bedrock incision rates associated with collisional wear by debris flows.

We developed a simple model that suggests that, even though the particles in a granular flow behave in many ways like a continuous flowing mass, the statistics of the particlebed contact forces are controlled primarily by isolated particlebed collisions rather than cooperative collisions involving, simultaneously, many contacting particles and the bed. Two pieces of evidence support this conjecture: (1) A mechanistic-based model for the force associated with isolated particlebed collisions replicates the size dependence of the contact force statistics associated with bulk granular flow in a drum, and (2) The largest contact forces from the granular flow simulations follow the same

dependence on particle size and impact velocity predicted from the mechanistic-based model for isolated particlebed collisions. Impacts have similarly been found important for governing other details of granular flows [130, 131].

Finally, we suggest that for a mechanistic-based model of bedrock incision due to debris flows, two key steps need to be taken next: (1) Obtain the relationship between the volume of rock detached per particle impact and impact force for bedrock commonly found in the field and (2) Obtain impact velocity statistics as they depend on particle size distribution and system dynamics such as local system mass and depth-averaged velocity to us in Equation 4.9 for the statistics of the largest impact forces. The first would likely require additional laboratory experiments, though Sklar and Dietrich [104] suggest a method for deducing this that is likely applicable for certain debris flow incision problems as well. The second would be nearly inaccessible experimentally for bulk granular flows, but could be determined from additional DEM simulations such as those we have presented in this chapter that have a track record of representing physical velocities, forces and other dynamics in physical granular flows.

4.7 Acknowledgment

We thank William E. Dietrich and Leslie Hsu for collaboration in this research. The physical experiments were performed by Leslie Hsu.

Table 4.1: Material properties of particles in the DEM simulations

property	symbol	value
material density	ρ	2650 kg/m^3
modulus of elasticity	E	29 GPa
Poissons ratio	ν	0.15
coefficient of friction	μ	0.5
coefficient of restitution	e	0.89

Table 4.2: Coefficients of the force model for each combination of particle-particle interaction in a mixture of $d_1 = 13.8$ mm particles and $d_2 = 50.0$ mm particles, as indicated.

parameter	13.8 & 13.8 mm	13.8 & 50 mm	50 & 50 mm
k_n (N/m$^{3/2}$)	1.16×10^9	1.45×10^9	2.21×10^9
k_t (N/m$^{3/2}$)	1.60×10^9	2.00×10^9	3.05×10^9
ζ_n (Ns/m$^{5/4}$)	1.44×10^2	2.25×10^2	1.37×10^3
ζ_t (Ns/m$^{5/4}$)	1.69×10^2	2.64×10^2	1.61×10^3

Table 4.3: Experimental and simulated drum. Drum diameter (D) and width (W) are given in meters

drum	D × W	other remarks
small physical drum	0.56 × 0.15	sandpaper on bed; no instrumentation
large physical drum	4 × 0.8	25 mm 25 mm ridges span bed; 15 cm (4.3^o) × 15 cm force plate
smooth computational drum	0.56 × 0.15	particlebed coefficient of friction $\mu_{pb} = 0.7$
bumpy computational drum	0.56 × 0.15	7 mm semi-cylindrical ridges span bed

Table 4.4: Parameters of the mixtures and monosized systems used for the comparisons between experimental results with simulation results discussed in Section 4.2.3 (e.g., Fig. 4.2). In this table D × W refer to the drum diameter (D) and width (W); "mass" refers to the total mass of all particles in each experiment or simulation; "mat" refers to the matrix particles that comprise the majority of the particles in each experiment or simulation; "int" refers to a single intruder particle where applicable; "ω" refers to the rotation speed of the drum in rotations per minute (rpm). In the list of run types "seg" refers to the segregation experiments using a single larger intruder particle among a matrix of smaller particles. In all cases except one, spherical particles were used; for the experiments these were glass marbles and for the simulations these were spherical particles whose properties are described in Subsection 4.2.1. For the physical experiments in the big drum whose results are shown in Fig. 4.2(c) and (d), the particles used were gravel particles of median grain size 10mm while for the corresponding simulations the particles used were spherical particles.

	Experiments			Simulations		
	drum:	particles:		drum:	particles:	
Figure	D × W (m × m)	mass (kg)	mat, int (mm,mm)	D × W (m × m)	mass (kg)	mat, int (mm,mm)
2a	0.56 × 0.15	3.13	13.8, –	0.56 × 0.15	3.13	13.8, –
2b top	0.56 × 0.15	3.13	13.8, 25	0.56 × 0.15	3.13	13.8, 25
2b bottom	0.56 × 0.15	3.13	13.8, 50	0.56 × 0.15	3.13	13.8, 50
2c-d	4.0 × 0.8	454	10, –	0.56 × 0.15	3.13	10, –

Table 4.5: Names and contents of the particle systems (mixtures and monosized systems) used for the results discussed in Section 4.3 (e.g., Figs. 4.7–4.15)

mixture name	size, type 1 mm, ±	mass type 1	size, type 2 mm, ±	mass type 2
13.8	13.8, 10%	4.30 kg	–	–
25.0	25.0, 10%	4.30 kg	–	–
Mix1_{50}	13.8, 10%	4.13 kg	50, 0%	0.17 kg
Mix4_{50}	13.8, 10%	3.61 kg	50, 0%	0.69 kg
Mix8_{50}	13.8, 10%	2.91 kg	50, 0%	1.39 kg
Mix99_{25}	13.8, 10%	2.15 kg	25.0, 10%	2.15 kg

Table 4.6: Fitting parameters for the relationships between each of the quantities $\overline{f}$, f_σ, and f_{max} as functions of $\overline{d}$ for Mix4_{50} and Mix8_{50} shown in Figs. 4.12 and 4.13 and Mix99_{25} shown in Figs. 4.14 and 4.15. In each case, an exponential and power law were fitted to the data: $y = a_1 \exp(b_1\overline{d})$, and $y = a_2\ \overline{d}^{b_2}$. (In each case, $\text{Mix}n_m$ refers to a 4.3 kg mixture of a "matrix" of 13.8 mm particles and $n \times m$ mm "intruder particles, as detailed in Table 4.5.)

mixture	y (force measure)	a_1 (N)	b_1 (1/m)	a_2 (N/m^{b_2})	b_2 (-)
Mix4_{50} and Mix8_{50}	$\overline{f}$	0.225	0.039	0.026	1.00
Mix4_{50} and Mix8_{50}	f_σ	0.893	0.008	0.578	0.203
Mix4_{50} and Mix8_{50}	f_{max}	2.590	0.057	0.088	1.526
Mix99_{25}	$\overline{f}$	0.227	0.055	0.034	0.998
Mix99_{25}	f_σ	0.288	0.073	0.025	1.301
Mix99_{25}	f_{max}	2.170	0.082	0.146	1.450

Table 4.7: Fitting parameters for the results shown in Fig. 4.17. In each case, an exponential law was fitted to the data: ($y = a_1 e^{b_1 x}$)

mixture –	y (force measure)	a_1 (N)	b_1 (1/m)
13.8mm and 50mm	$\overline{f}_{sys}$	0.249	0.038
	$f_{\sigma,sys}$	0.285	0.070
	$f_{max,sys}$	2.876	0.064
13.8mm and 25mm	$\overline{f}_{sys}$	0.109	0.097
	$f_{\sigma,sys}$	0.122	0.125
	$f_{max,sys}$	0.998	0.132

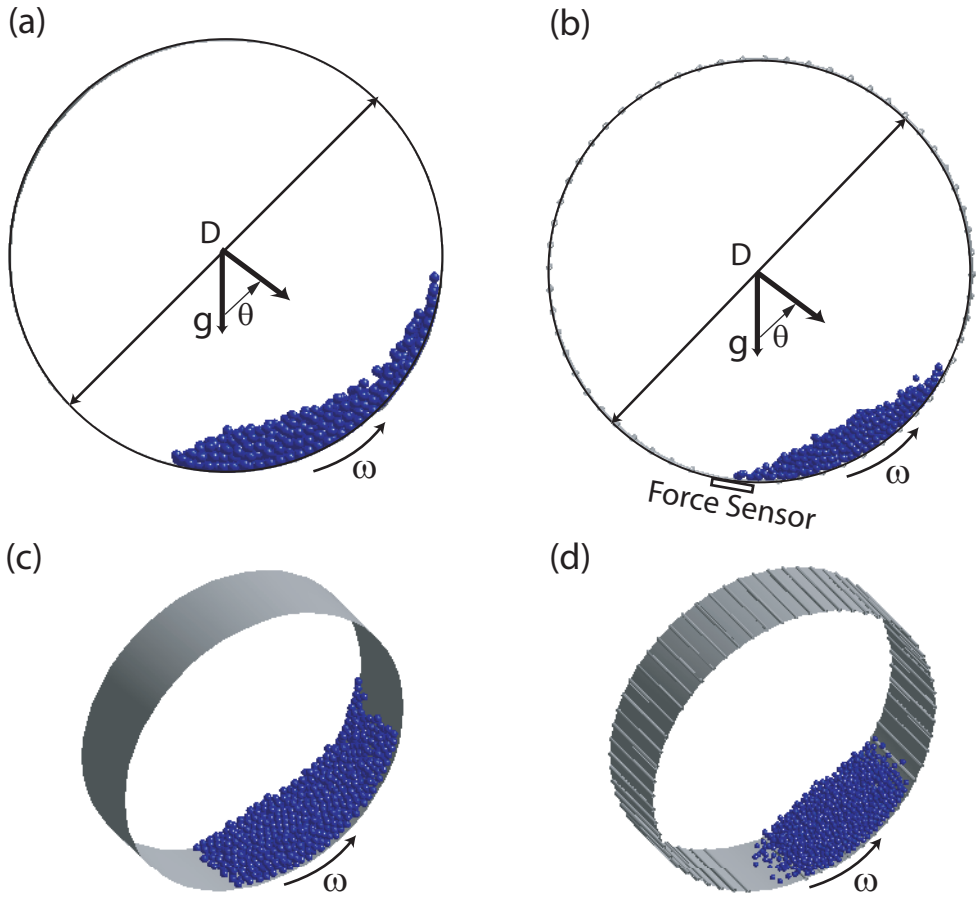

Figure 4.1: Snapshots showing the two simulated drums used for the computational results presented in this chapter. Details of each are given in Table 4.3 (a) A snapshot of the simulations representing the smaller experimental drum, where the walls are physically smooth. For this snapshot 3.13kg of $d = 13.8$ mm particles are rotated at a rotation speed ω of 12 rotations per minute (rpm) (b) A snapshot of the simulations representing the large physical drum, where the outer walls, or bed, have periodic treads as described in the text. For this snapshot 1.6 kg of $d = 10.0$ mm particles are rotated at a rotation speed of 6 rpm (c)Oblique view of the simulation shown in (a). (d) Oblique view of the simulation shown in (b).

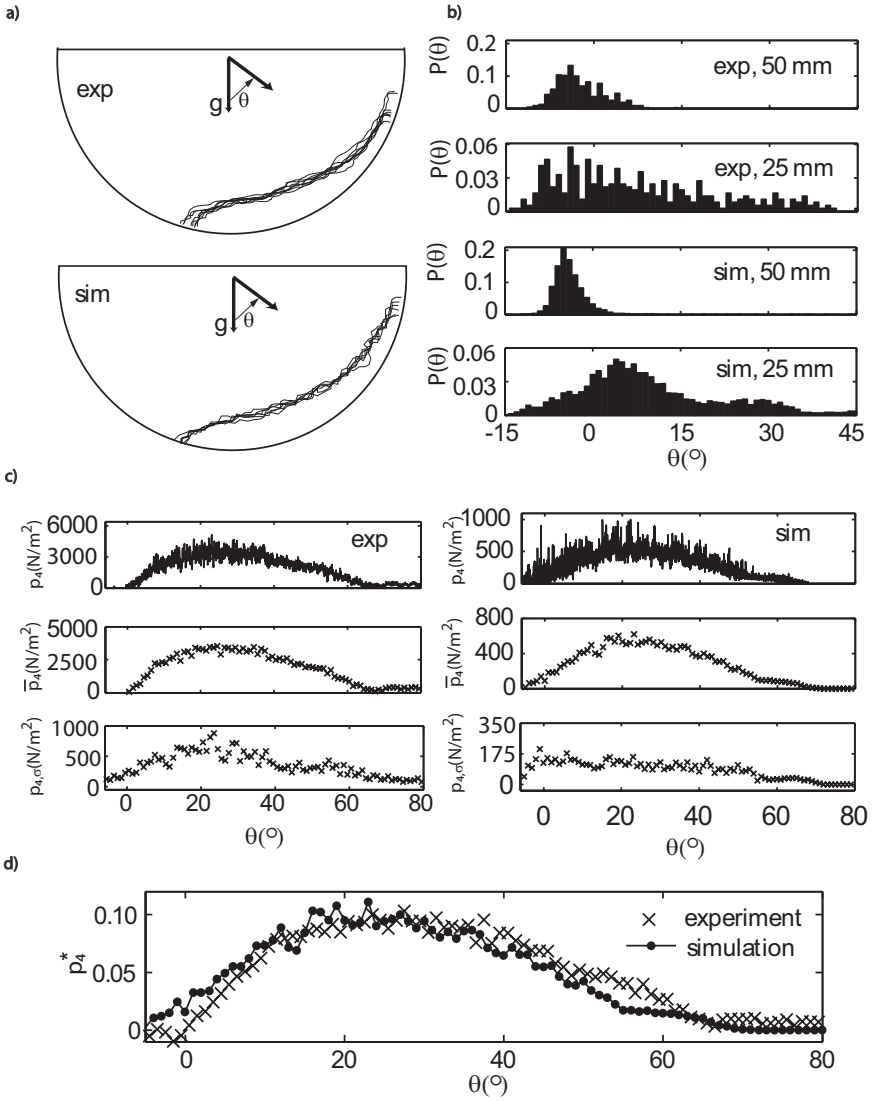

Figure 4.2: Results from analogous physical experiments (exp) and computational simulations (sim) as noted in Table 4.4. (a) The longitudinal surface profiles of the granular flows. (b) The probability distribution function (pdf) of the location of a large intruder particle (size noted in plots) among smaller matrix particles. (c) From top to bottom in each column: instantaneous pressures (p_4), locally averaged pressures ($\overline{p}_4$), and local standard deviation of the bed pressure ($p_{4,\sigma}$) all plotted as functions of drum bed location (d) $\overline{p}_4$ vs. θ normalized by the weight and sensor size (Equation B.1.)

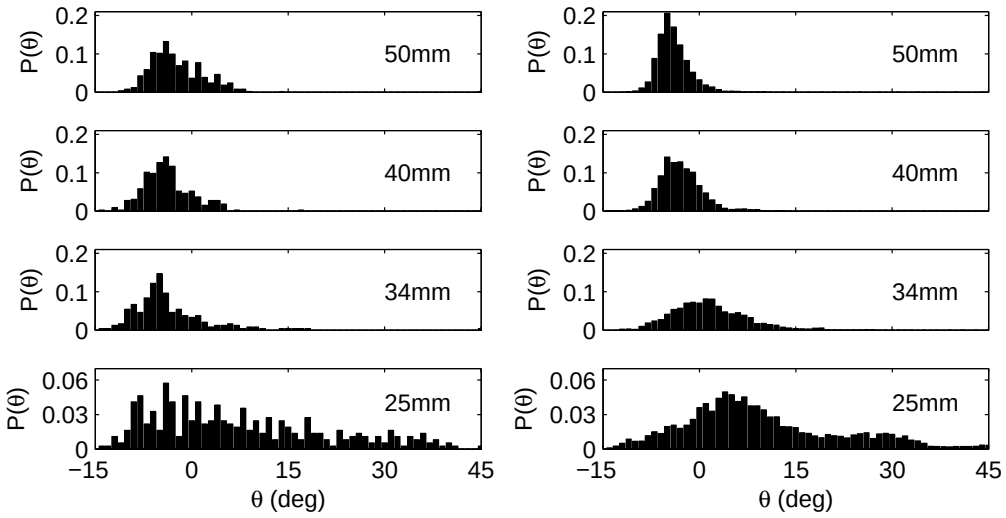

Figure 4.3: The probability distribution function (pdf) of the location of a large intruder particle (size of particles as indicated in the figures) among smaller matrix particles. On the left column are the experimental results and on the right column are the simulation resutls.

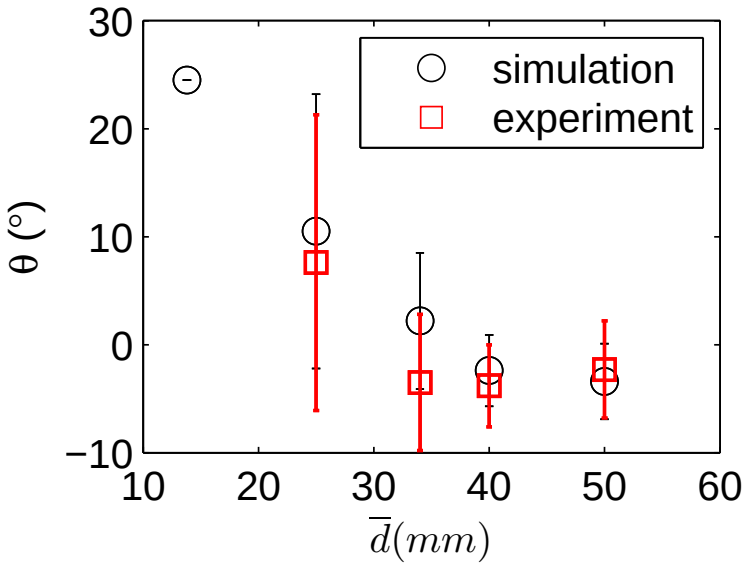

Figure 4.4: The mean location of different sizes of intruder particles among smaller matrix particles. The error bar indicates the standard deviation.

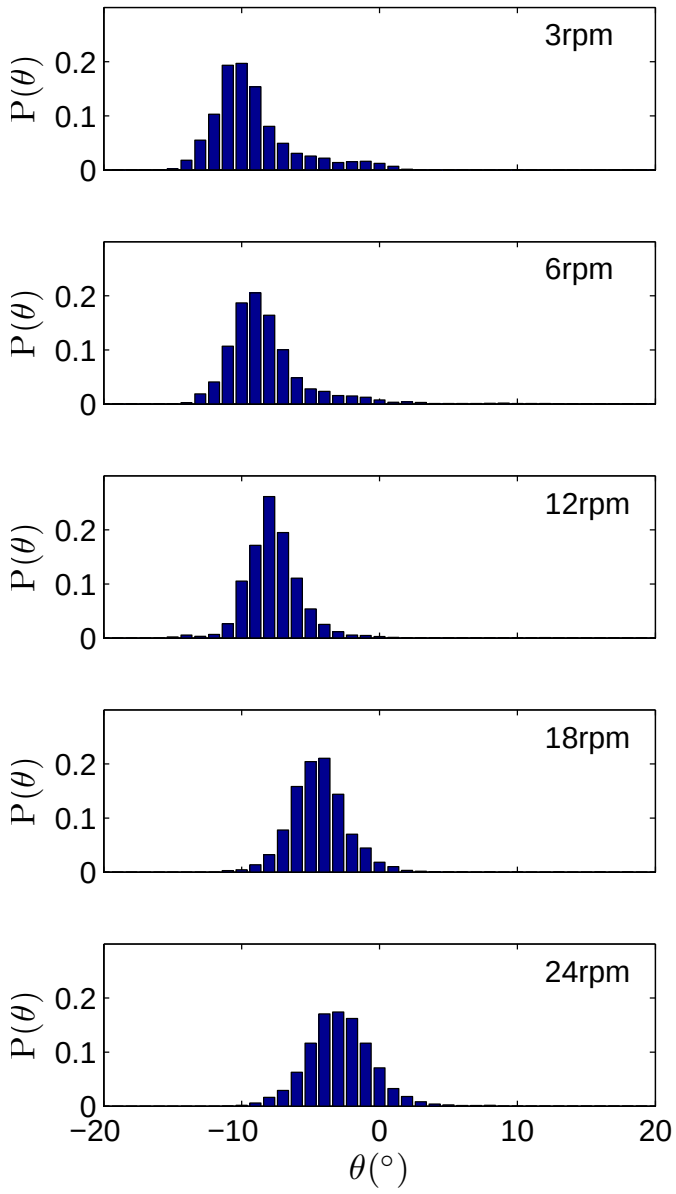

Figure 4.5: The pdf of the location of a 50 mm intruder particle among smaller matrix particles for different speeds of rotation.

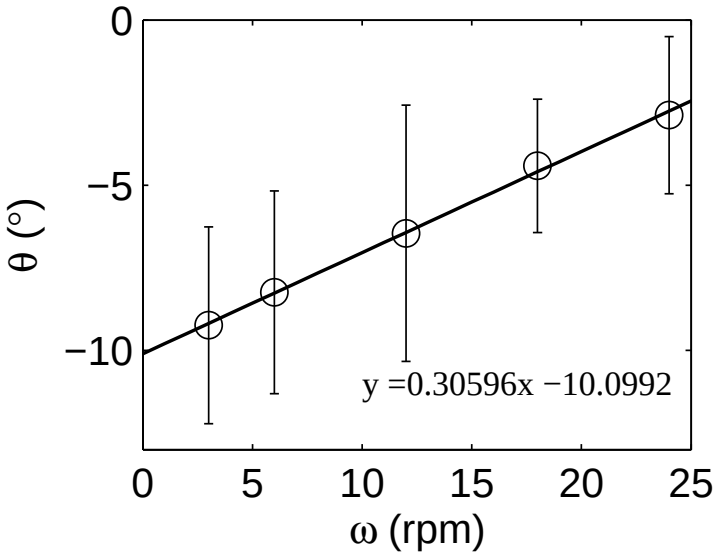

Figure 4.6: The mean location of a 50 mm intruder particle among smaller matrix particles as a function of speed of rotation. The error bars indicate the standard deviation.

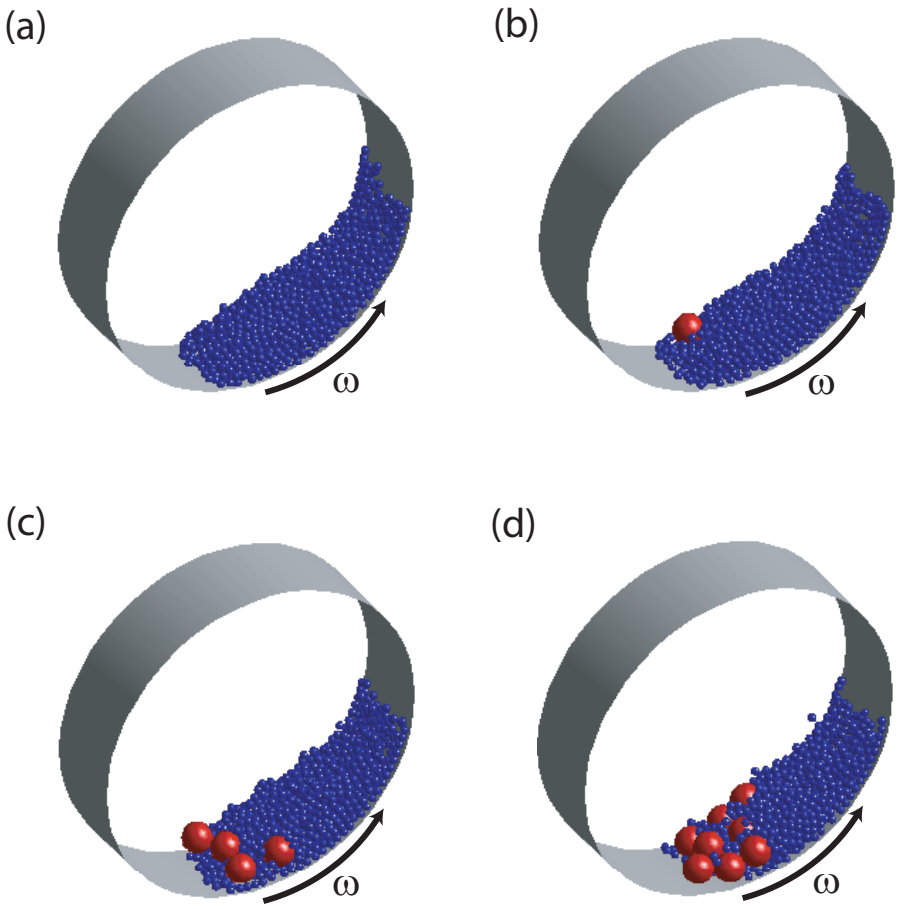

Figure 4.7: Snapshots from simulations of granular flows in a rotating drum obtained using systems of particles of the same total mass (4.3 kg) rotated in the smooth computational drum (D = 0.56m, w = 0.15m) at a rotational speed of 12 rpm. (a) 13.8 mm particles alone, (b) Mix1_{50} (one 50.0 mm particle among many more 13.8 mm particles), (c) Mix4_{50} (four 50.0 mm particles among many more 13.8 mm particles), and (d) Mix8_{50} (eight 50.0 mm particles among many more 13.8 mm particles). System properties are given in Table 4.5

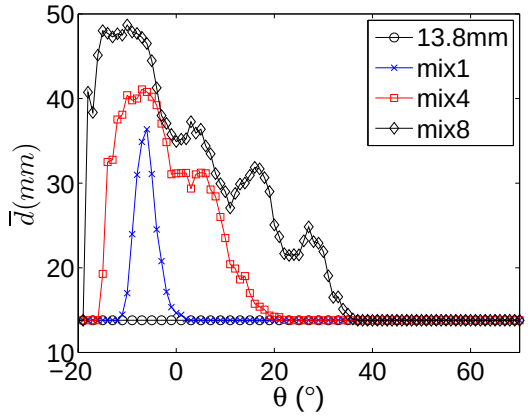

Figure 4.8: Mass-averaged particle size, d, as a function of θ, position along the bed, for the simulations shown in Fig. 4.7. As described in the text, the data are averaged over 1° bins. Lines are included in the plots to guide the eye.

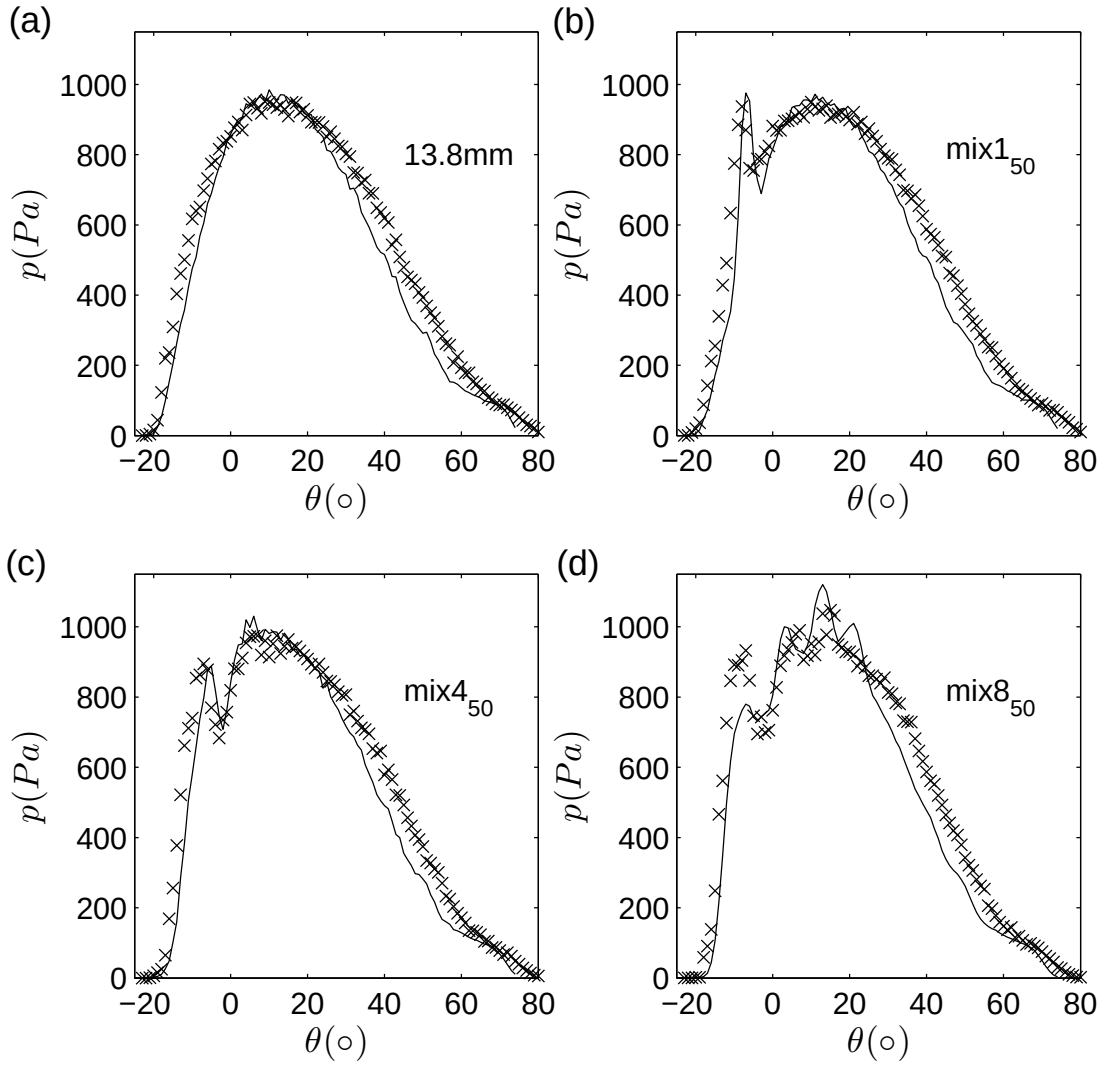

Figure 4.9: Plots of average pressure measured at the bed, $\overline{p}$ ($\times$) and average pressure calculated from the weight of the paritcles $\overline{p}_w$ (lines) vs. location along the bed (θ) from the simulations shown in Fig. 4.7. In each case, the relevant system is noted in the upper right hand corner of each plot. (System properties are given in Table 4.5)

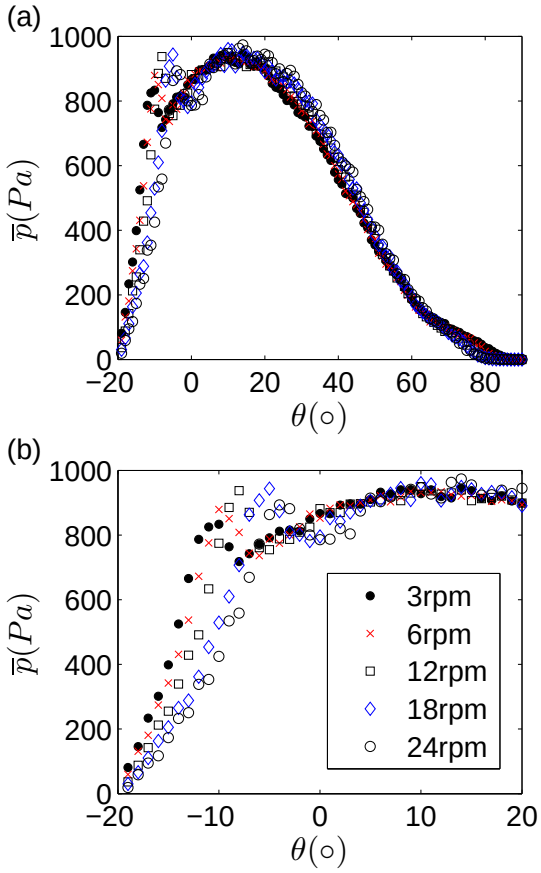

Figure 4.10: (a)Plot of $\overline{p}$ vs. θ for Mix1_{50} for various values of ω. (b) shows the same plots as in (a) but zoomed into the region near the front (-20 $\leq \theta \leq$ 20)

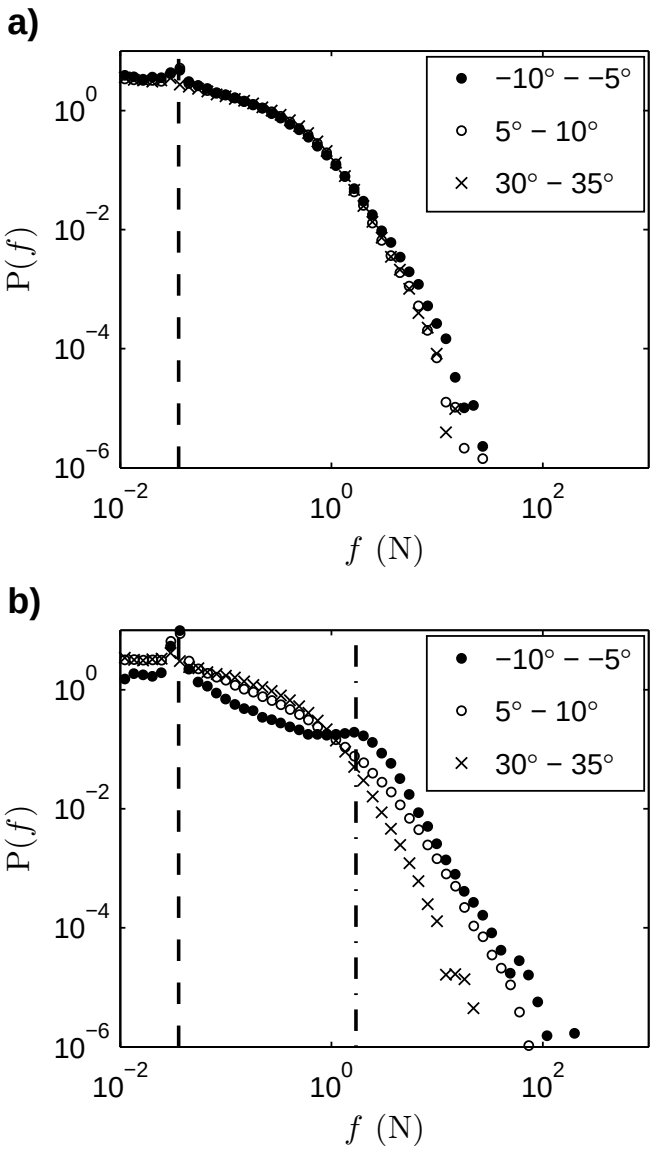

Figure 4.11: Probability distribution functions of the boundary forces at particular locations along the boundary as noted for (a) 13.8 mm particles alone and (b)Mix8_{50} (eight 50.0 mm particles among many more 13.8 mm particles; Table 4.5). The lines indicate the weight of a 13.8mm particle (dashed line) and a 50mm particle (dash-dotted line).

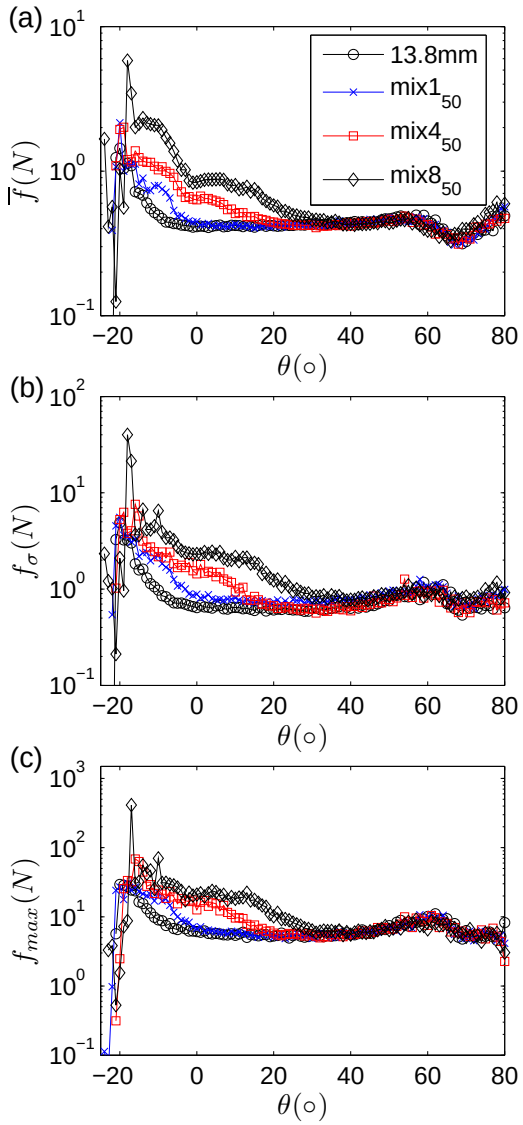

Figure 4.12: Details of forces along the bed as functions of location (θ) for the simulations shown in Fig. 4.7, averaged over 1° bins. (a) Local average contact force ($\overline{f}$). (b) Local standard deviation of the contact force (f_σ), and (c) Local maximum of the contact forces (f_{max}). Lines are included in the plots to guide the eye. Table 4.5 contains particle system details.

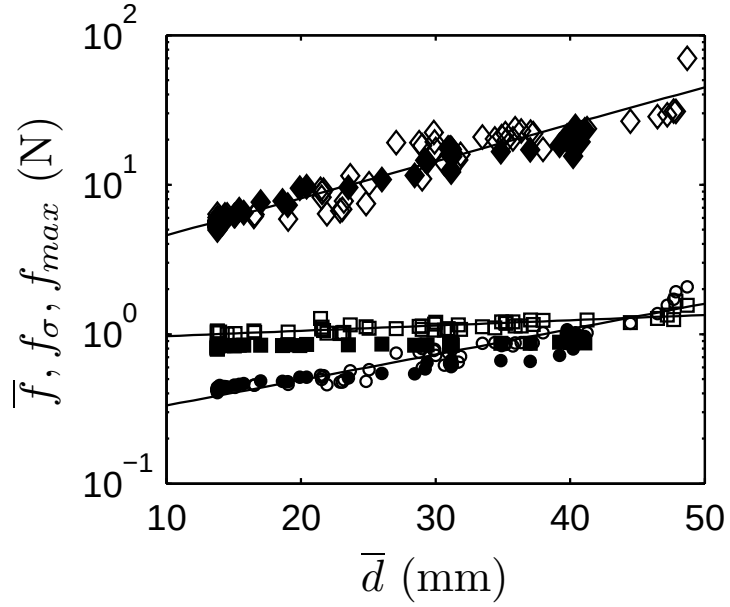

Figure 4.13: Parametric plots of local average contact force $\overline{f}$ ($\circ$), local standard deviation of contact forces, f_σ ($\square$), and local maximum contact forces, f_{max} ($\diamond$) as a function of local average particle size $\overline{d}$ for each 1° bin from the data in Figs.4.8 and 4.12 for Mix4_{50} (filled symbols) and Mix8_{50} (open symbols). (Mix4_{50} refers to a 4.3 kg mixture of four 50.0 mm particles among many more 13.8 mm particles, and Mix8_{50} refers to a 4.3 kg mixture of eight 50.0 mm particles among many more 13.8 mm particles). The lines represent exponential fits, $y = a_1 \exp(b_1 \overline{d})$ where y represents the quantities $\overline{f}$, f_σ, and f_{max}. The coefficients found from fitting these exponential function to the data a_1 and b_1 are given in Table 4.6. (System properties are given in Table 4.5.)

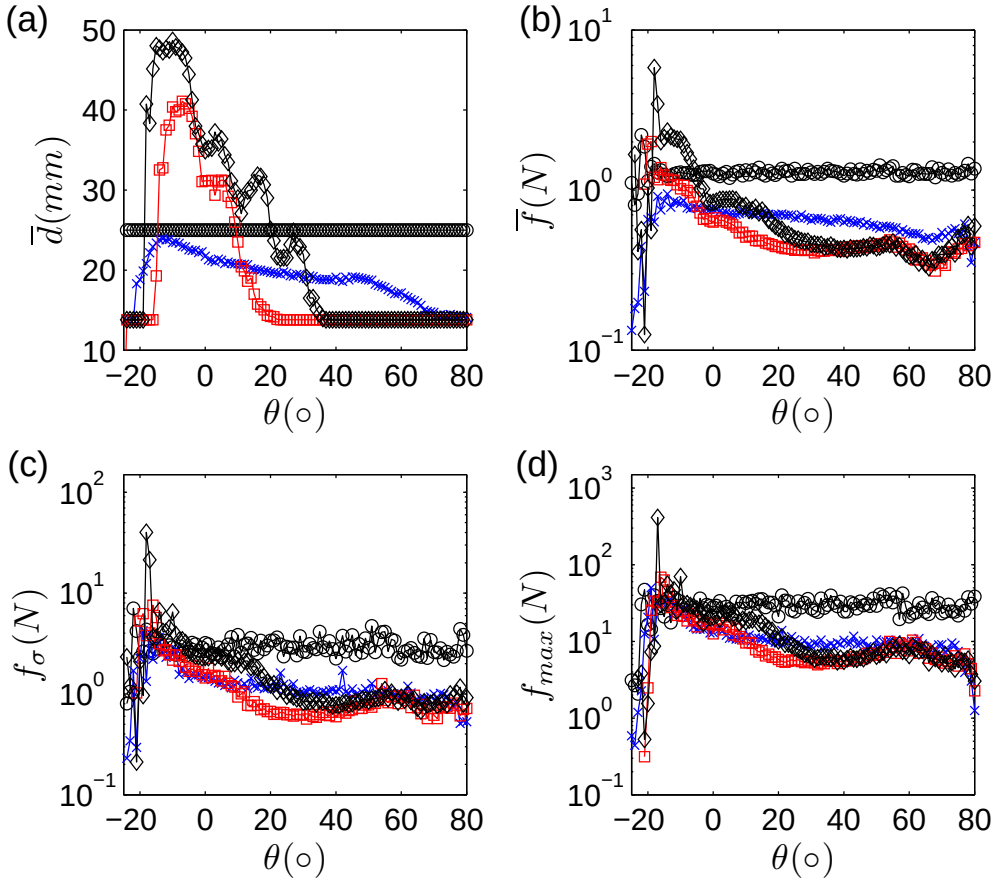

Figure 4.14: Mass averaged grain size and force statistics plotted as functions of bed location, θ, (plots analogous to those shown in Figs.4.8 and 4.12) for two sets of mixtures, each having similar average system sizes: (1) Mix99_{25} and Mix4_{50} and (2) 25.0 and Mix8_{50}. (Mix99_{25} is a 4.3 kg mixture of ninety-nine 25 mm particles among many more 13.8 mm particles; Mix4_{50} is a 4.3 kg mixture of four 50.0 mm particles among many more 13.8 mm particles; Mix8_{50} is a mixture of eight 50.0 mm particles among many more 13.8 mm particles; 25 mm is a system of 25.0 mm particles alone.) (System properties are given in Table 4.5.) In each case, the dependent quantity is averaged over 1° bins. (a) Local average particle size $\overline{d}$. (b) Local average contact forces $\overline{f}$. (c) Local standard deviation contact forces f_σ. (d) Local maximum contact forces f_{max}. Lines are included to guide the eye

.

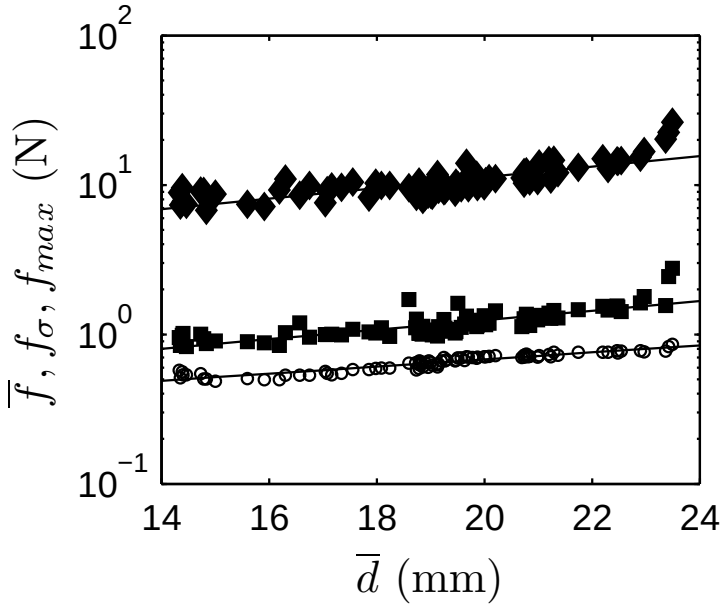

Figure 4.15: Parametric plots of average contact forces $\overline{f}$ (○), standard deviation of the contact forces f_σ (■), and maximum contact forces f_{max} (♦) as a function of local average particle size $\overline{d}$ for each 1° bin from the data in Fig. 4.14 for a mixture of 13.8 mm particles and ninety-nine 25 mm particles (Mix99_{25}). (System properties are given in Table 4.5.)

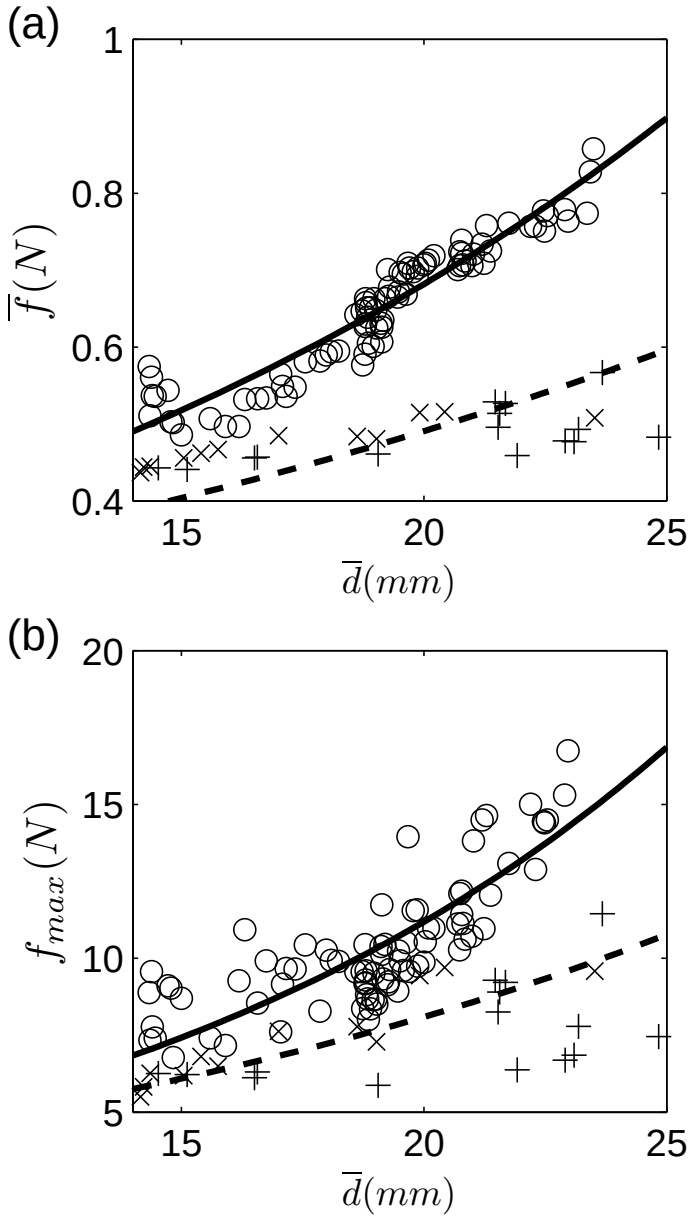

Figure 4.16: Parametric plots of (a) local average contact force $\overline{f}$, and (b) local maximum contact forces f_{max} as a function of local average particle size $\overline{d}$ for Mix4_{50}, Mix8_{50}, and Mix99_{25} over relevant values of $\overline{d}$ for all three mixtures ($\overline{d} = 14\ mm - 25\ mm$). The lines represent the exponential fits for each shown in Table 4.6. (System properties are given in Table 4.5.)

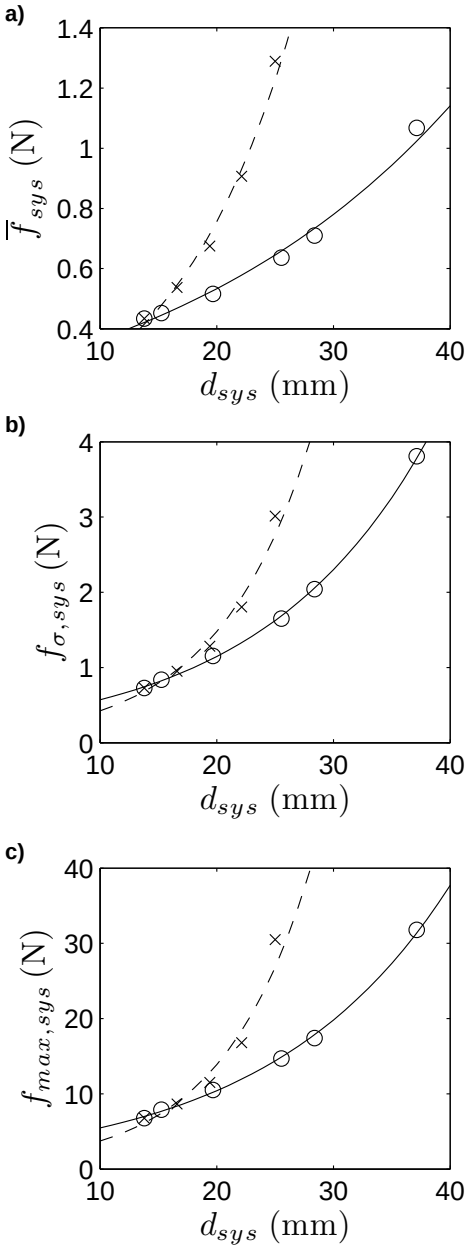

Figure 4.17: Whole system particle.bed force statistics plotted as a function of system-averaged particle size for 4.3 kg mixtures of 13.8 mm and 50.0 mm particles (○) and 13.8 mm and 25.0 mm particles (×). (a) Average contact force on the bed $f_{\sigma,sys}$. (b) Standard deviation of the contact force on the bed $f_{\sigma,sys}$. (c) Maximum contact force on the bed $f_{max,sys}$. The lines are exponential fits to the data, and the fitting parameters are given in Table 4.7.

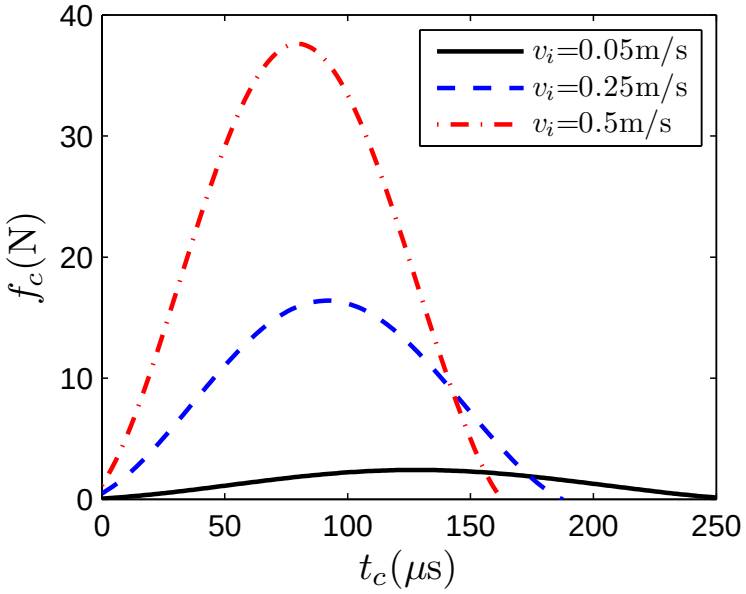

Figure 4.18: The force between a particle 25 mm diameter particle and a fixed boundary as a function of time after initial contact (t_c) for specific impact velocities, v_i as indicated in the legend.

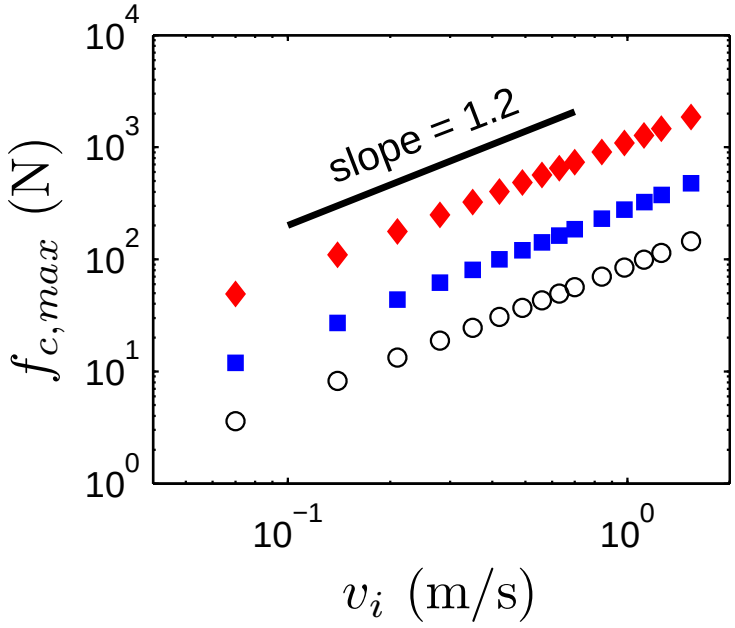

Figure 4.19: The maximum particle-bed force $f_{c,max}$ as a function of impact velocity v_i for isolated particle-bed collisions for four different particle sizes: 13.8mm (○), 25mm (■) and 50mm (♦) particles. The peak force increases as power law function of the impact velocity with a power of 1.2, and for a given value of v_i, $f_{c,max} \sim d^2$.

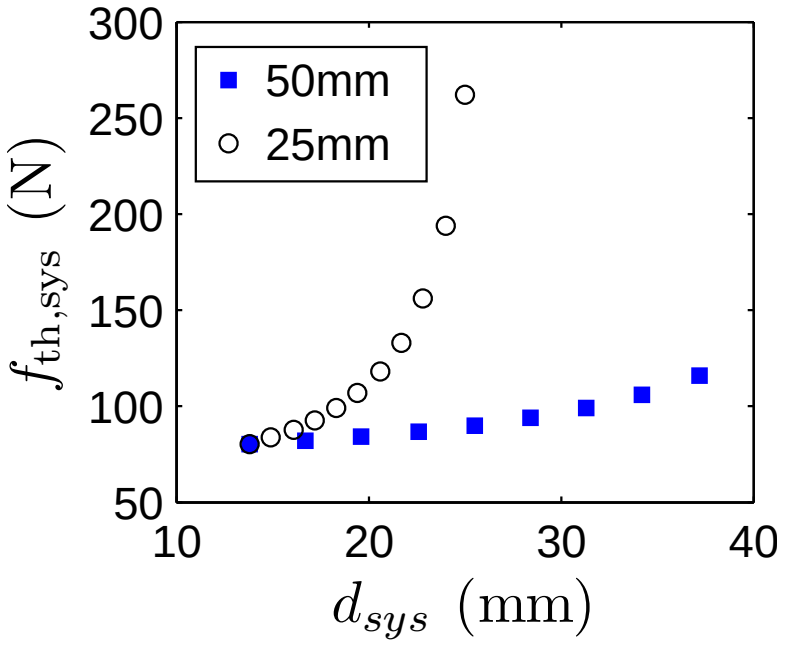

Figure 4.20: Theoretical system-averaged particlebed force $\overline{f}_{\mathrm{th,sys}}$ as a function of system average particle size $\overline{d}_{sys}$ from Equation 4.9 for two different mixtures: 4.3 kg of different fractions of 13.8 mm and 25.0 mm spheres and 4.3 kg of different fractions of 13.8 mm and 50.0 mm spheres (denoted 25 and 50 in the legend, respectively).

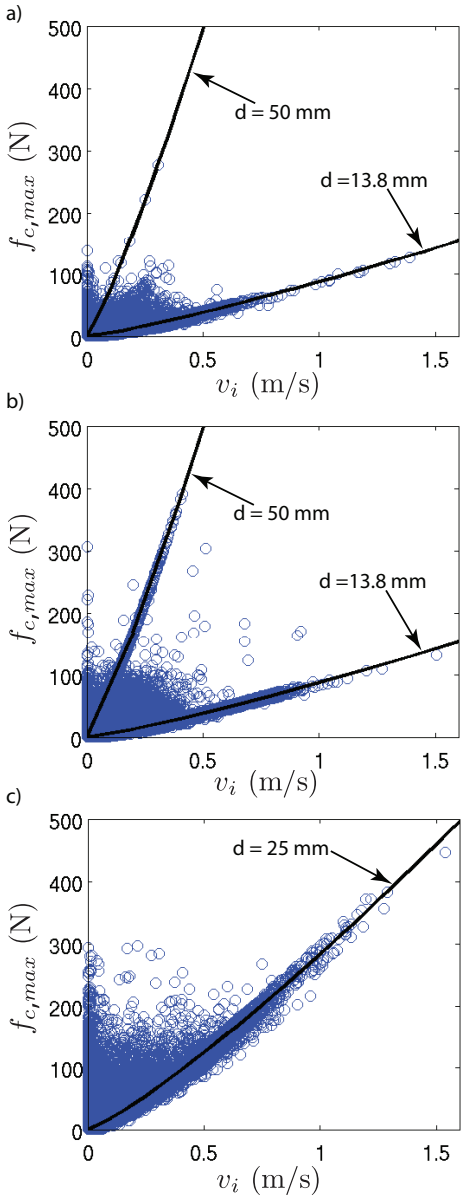

Figure 4.21: The maximum force, $f_{c,max}$, for each particle-bed contact as a function of the impact velocity, v_i, for three granular systems: (a) Mix1_{50} (one 50.0 mm particle among many more 13.8 mm particles), (b) Mix8_{50} (eight 50.0 mm particles among many more 13.8 mm particles), and (c) 25mm particles alone. (System properties are given in Table 4.5.) The solid lines represent the maximum contact forces for releasing a single particle on a horizontal flat boundary. In (a) and (b), the lines represent this information for a 50 mm particle and a 13.8 mm particle, and in (c), the line represents this information for a 25 mm particle as noted.

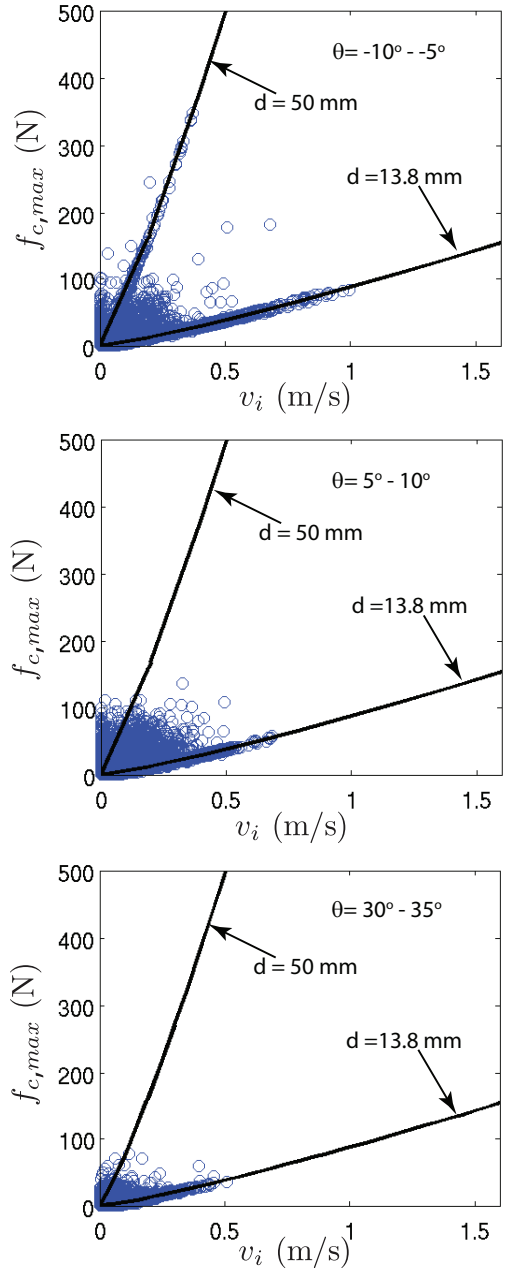

Figure 4.22: The maximum force for each particle-bed contact as a function of the impact velocity for Mix8_{50} (eight 50.0 mm particles among many more 13.8 mm particles) for specific locations along the drum bed as noted. The solid lines represent the maximum contact forces from a single 50 mm particle (top left) and a 13.8 mm particle (bottom right) when released on a horizontal flat boundary. (System properties are given in Table 4.5.)

Chapter 5

Wet granular flows

5.1 Introduction

In the previous chapters the discussion was limited to dry granular flows, which do not include the effects of interstitial fluid. However, in most natural or industrial processes interstitial fluids are present. The interstitial fluids may be air [132, 133], water [63] or other types of liquid [134]. In this thesis we limit the discussion of interstitial fluid to liquid interstitial fluids and "fluid" for the rest of the chapter specifically refers to "liquid". The effects of interstitial fluids have been subject of numerous studies [135, 136, 137, 45, 138, 139, 140, 63, 141, 142, 30, 134, 143]. Understanding the ways in which interstitial fluid mediates interparticle interactions is necessary for the development of a mechanistic model for a particle-fluid system.

The effect of liquids on granular flows can be broadly discussed in terms of one of two categories: unsaturated and saturated granular flows. In unsaturated granular flows an interstitial fluid is present at sufficiently low level that it does not fill all of the pore spaces. As will be discussed in Section 5.2, the presence of small amounts of fluid gives rise to an attractive force between the particles. The attractive force is one of the reasons for cohesivity in many soils [144]. In saturated flows all the pore spaces between the particles are filled with liquid, and there is no attractive force analogous to that of unsaturated granular materials. Instead the interstitial fluid damps particle motion via viscous effects. If this effect is sufficiently large it gives rise to an increase in pore fluid pressure. The pore-pressure effect is viewed by many as dictating the characteristics of

the flow [2]. The magnitude of the pore pressure varies depending on the type of flow. Pore pressure in excess of the hydrostatic pressure can be intermittent and localized to regions of sliding or very fast deformation [145, 146, 147, 148]. In addition, the occurrence of the excess pore pressure depends on the initial void ratio (particle configuration) and particle size distribution of the granular material. Excess pore pressure in excess of the hydrostatic pressure can also be sustained. The magnitude of the pore pressure increases if the fine particle content is high [148] due to the reduced permeability of granular assemblies composed of fine particles [144]. The lower permeability prevents the dissipation of excess pore pressure generated due to some deformation in saturated granular materials.

Increased pore pressure results in reduced interparticle contact and subsequently reduces the effective normal stress and can cause a major failure of granular assemblies [149, 2, 148]. Detailed pore pressure measurements and theoretical models for saturated soil are mainly limited to very small deformations and in undrained conditions, such as in typical triaxial compression test [149, 150]. In such studies, the pore pressure is associated with liquefaction events, in which the saturated granular material losses all of its strength. In cases of large deformations (granular flows), increased pore pressure is often associated with an increased run out distance [2, 146, 151, 147]. These types of studies are limited to laboratory experiments, as it is nearly impossible to measure the pore pressure in natural large scale flows. In large scale flows the pore pressure is back calculated (roughly estimated) from the run out distance of the flow [152, 2]. To better understand the effects of the pore pressure on flow properties, models that account for particle-particle interaction as well as particle-fluid interaction are important.

5.2 Unsaturated granular flows

At lower moisture content, when all of the pore spaces between the particles are not filled with liquid (unsaturated soils, moisture content less than 30%), the liquid might act as a binding force between particles [153, 154, 155, 156]. The interaction between the fluid and particles changes with changes in the amount of moisture content (degree of saturation) and the type of particles (size of particles) [157]. The liquid forms a bridge between pair of closely spaced particles. This bridge is often referred to as a liquid

bridge. The binding force generated is due to surface tension of the interstitial fluid and the pressure gradient at the liquid-air interface [158]. The effect of the binding force is more pronounced on smaller particles (maximum size of about 2mm) where the force associated with the liquid bridge is large compared to the weight of the particles. Compared to electrostatic and/or Van der Waals forces between particles, which dominate the interaction between very fine particles (< 100 μm), the attraction force developed due to liquid bridges is large and affects flow mechanics of larger particles (up to about 2mm diameter) [159]. However, for gravel size particles the binding force becomes less effective and the gravity force begins to dominate the flow rheology [160, 161].

A number of researchers have studied the effect of a cohesive interparticle force on macroscopic behaviors of granular materials. Brewster et al. [65] and Rognon et al. [161] studied the effect of cohesive interparticle forces on the rheology of dense granular flows using DEM models that include a constant attraction force between contacting particles. Brewster et al. [65] proposed that Equation 2.1 could be used to model the rheology, though an additional term proportional to the shear rate is required to account for the cohesive forces between particles. Rognon et al. [161] proposed that Equation 3.3 is more appropriate, using fitting parameters that are a function of the Bond number, which is the ratio of gravitational force and surface tension force. These two models for cohesive particles do not exactly represent the interparticle forces associated with liquid bridges in unsaturated granular materials.

As discussed earlier in this chapter, an attraction force develops between closely spaced pair of particles in the presence of small amount of moisture content. Fig. 5.1 is a sketch of a liquid bridge formed between two particles. In reality, a liquid bridge can involve more than two particles. For simplicity, in this research each liquid bridge is restricted to two particles. The attractive force F_c is modeled using the Boundary Method as in Hotta et al. [158].

$$F_c = 2\pi a \Gamma sin(\alpha) sin(\alpha + \beta) + \pi a^2 (\Delta p_c) sin^2(\alpha) \tag{5.1}$$

where F_c is the attractive force due to the liquid bridge, Γ is the surface tension of the interstitial fluid, a is the particle radius, α is the half filling angle, and β is the contact angle formed between the liquid and the surface of a particle. In this research β is assumed to be zero, which is a good assumption for water on glass [158]. The first

term term in Eq. 5.1 represents the force generated as a result of the surface tension. The second term represents the force generated due to the pressure difference across the interface. p_c is the pressure deficiency across the air-liquid interface and is computed from the Laplace-Young equation

$$\Delta p_c = \Gamma \left(\frac{1}{R_1} + \frac{1}{R_2} \right) = \Gamma \left(\frac{\ddot{Y}}{(1+\dot{Y}^2)^{3/2}} - \frac{1}{Y(1+\dot{Y}^2)^{1/2}} \right) \tag{5.2}$$

where the dots represent derivatives with respect to X (see Fig. 5.1). This equation may be solved numerically as outlined by Lian et al. [162]. Figure 5.2 shows the forces due to liquid bridge between two particles plotted as a function of one half of the separation distance, S_c. The magnitude of F_c and the separation distance for which the attractive force is non-negligible depends on the volume of the liquid between the particles V. In all cases, the attractive force decreases as the separation distance between the particles increases. If V is small, F_c is larger at lower values of S_c and the liquid bridge breaks at a relatively low value of S_c. On the other hand, if V is large, F_c is smaller at S_c and the liquid bridge doesn't break until S_c is an order of the diameter of the particles. The numerical solution by Lian et al. [162] has been previously incorporated into DEM models to investigate particle segregation in granular flows [159, 163], compaction of granular materials [164] and stability and shear strength of assembly of particles [156]. We have incorporated this model into our DEM to perform investigations of the effect of the presence of liquid bridges on rheology of unsaturated granular flows.

We added F_c to the contact force in the normal direction (F_n), previously shown in Chapter 1. We assumed that a liquid bridge forms when a pair of particles comes into contact and the liquid bridge breaks at a critical separation distance, $S_{critical}$, which is equal to the cube root V. Further, we assume that all the liquid bridges have the same predefined V.

We used this model in simulations of a shallow granular flow in a rotating drum. The simulations involve mixtures of three particles: 1.25, 3.0, and 6.25mm. The total number of particles is 12500 and the total mass is 0.0524kg. Fig. 5.3 show snapshots from simulations where $V = 0.0mm^3$ and $V = 0.01mm^3$, which correspond to dry flow and volumetric moisture content of 2% respectively. The added cohesive force changes the flow kinematics. Two differences are apparent. First, the segregation is clearly

affected by the presence of liquid. In the case of the system shown in Fig. 5.3(b), the larger particles no longer segregate all the way to the front of the flow. Second, the longitudinal profile is altered, suggesting the internal stresses of the granular assembly as a whole are affected by the local interactions between individual particles. Fig. 5.4 shows the steady state velocity profiles at two locations in the drum for the model systems depicted in Fig. 5.3. Fig. 5.4(a) is the profile of the particles alone, while Fig. 5.3(b) shows the profile for the case with some fluid. The fluid in this case reduces the maximum velocity and the average shear rate by approximately 1/3. All of this information is useful in considering the possible modifications one could make to continuum models for particle-fluid mixtures. However, for systems of larger particles more typical of debris flows, other fluid-particle interactions are likely more important as we address in the next subsection.

5.3 Saturated granular flows: Review

In the case of saturated granular flows all the pore spaces are filled with interstitial fluid. Depending on the boundary conditions and solid volume fractions ν different approaches have been used in several previous studies. In this section we will briefly review some of these techniques.

Continuum models

Savage and Hutter [34] developed a continuum model for finite, shallow cohesionless granular flows. This model framework involves solving the mass and momentum equations of the bulk granular flow. The most important hypothesis in this model is that the pressure gradient in the stream-wise direction is non-negligible. Iverson [2, 165, 140] applied this model to saturated granular flows. Iverson [2] incorporated the excess pore pressure, which is expected to develop in saturated granular flows, to the momentum conservation equation of Savage and Hutter [34, 166, 118]. In Iverson's model the profile of the excess pore pressure is assumed to be linearly increase with depth [140, 144, 152]. The parameters such as the coefficient of friction, permeability and volume fraction are all assumed or must be measured from experiments or other types of direct numerical simulations. The main disadvantage of this type of models is the lack of explicit

particle-particle and particle-fluid interaction.

Coupled CFD-DEM models

Another way of numerically modeling saturated granular flows involves modeling particle-particle and fluid-particle contact force equations. Coupling computational fluid dynamics (CFD) models with DEM is one of the most common approaches [167, 168, 169, 170]. The CFD models include Reynolds Average Navier Stoke (RANS) [171], Large Eddy Simulation (LES) [172, 173], Lattice Boltzmaan (LB) solution [169], and Smoothed Particle Hydrodynamics (SPH) [170]. In these models the flow field for the fluid and particles is solved simultaneously. The forces due to the particle-fluid interactions are added to the momentum conservation equation of the fluid and the particles. Most of the simulations in the literature include only a drag force. A lift force is also included in some simulations, such as the sediment transport model by Schmeeckle [174]. Additional forces such as the magnus effect, which accounts for the rotation of particles, may also be included in these type of CFD-DEM coupled models. The main disadvantage of these numerical modeling is the intense computational time required to solve the kinematics and dynamics of the two phases. In addition, these types of models are more applicable to sparse flows, where enduring particle-particle contacts are not dominant. In dense granular flows a particle may be partially or fully shielded from the fluid by other particles. In such cases applying forces, such as the drag force, only based on local average relative velocities may lead to overestimating the drag force on the particles, as particles shielded by other particles may not experience the actual local velocity.

Porous media-based models

For a more accurate representation of the relationship between local particle arrangements and pore pressure changes in particle-fluid mixtures Tarumi and Hakuno [175, 176, 177] proposed a DEM based model which accounts for changes in local fluid pressure based on the changes in the volume of local voids. The fluid is treated as an elastic media with specific volumetric elasticity, and the change in fluid-pressure is assumed to be linearly proportional to the change in the local volume. The fluid flow is then determined based on Darcy's law of flow in porous media. For example, if the

volume of a pore space decreases, the pressure gradient forces the fluid to flow to adjacent pore spaces. These models demonstrated the evolution of pore-pressure due to applied stresses in saturated granular materials. However, tracking the pore spaces in DEM models is computationally very intense and the DEM models are limited to 2D or to very small 3D models. In addition, these models have been used only for quasi-static flows of confined granular materials.

Lubrication models

An alternative approach is to focus the modeling of the fluid entirely on the effect the presence of the fluid has on the interparticle forces. The effectiveness of this approach would be limited to those where the fluid moves primarily with the particles and the effect of independent fluid movement on the dynamics of the system is minimal. One way to do this is to adopt the lubrication model to capture the viscous effect of fluid on particle-particle interactions in saturated dense granular flows [178, 179, 180, 181, 182]. The lubrication models have recently been applied to collision of particles that have a wet surface [178]. The core idea of this model is based on the assumption that when two particles approach each other the fluid between the particles is squeezed out. The fluid is squeezed out because of an increased local pressure gradient in the fluid. The increased pressure damps the approach velocity of the two particles [178, 183]. These indicates that the forces on approaching particles resulting in an elevated pressure are dependent on the approach velocity, distance between the particles, and the viscosity of the fluid. If the approach velocity is large, the fluid will be squeezed out at a faster rate. Faster rates require large pressure gradients, which also provides larger damping force on the particles. If the the separation distance is larger, the pressure gradient will be lower. The squeezing out of the fluid also depends on the viscosity of the fluid. Fluids with higher viscosity require a higher pressure gradient to be squeezed out. These lead to the following generalized relationship between the lubrication force F_ν and the approach velocity v_{ij}, separation distance $\tilde{h}_{ij}$, and the viscosity of the fluid η_f.

$$F_\nu \sim \frac{\eta_f v_{ij}}{\tilde{h}_{ij}} \tag{5.3}$$

For two otherwise isolated spheres, analytic [178, 183] and experimental [180] studies

have shown that the exact form of the lubrication force is given as

$$F_\nu = \frac{3}{8}\pi d^2 \frac{\eta_f v_{ij}}{\tilde{h}_{ij}} \tag{5.4}$$

where d is the size of the particles and $\tilde{h}_{ij}$ is the distance between the surface of the two particles.

These analytic solutions and experimental verifications are only possible for the interaction between two otherwise isolated particles. Nevertheless, the application of lubrication models to dense granular flows has received some attention in recent years [184]. Using Eq. 5.4 for dense granular flows poses a problem because in the presence of multiple particles it is not easy to determine the collective effect of all particle displacements and velocities. In our simulation we adapt this framework, and we have ignored the effect of particle rotation and tangential relative velocity. We assume the magnitude of lubrication forces due to the rotation and relative tangential velocities of particles is very small compared to the normal component of the lubrication force. We will assume that Eq. 5.4 can be used to qualitatively study the response of dense granular flows to different interstitial fluids. Before we discuss the details the DEM simulations that incorporate the lubrication models, we will briefly discuss some experiments we did to study effects of different interstitial fluids on the bulk granular flow.

5.4 Saturated granular flows: Experiments

To investigate the effect of interstitial fluids on thin granular flows we carried out experiments in the large rotating drum [Chapter 4]. The experiments were performed at the Richmond Facility at the University of California at Berkeley. In the experiments the amount of water and fines was systematically varied to study the effect of wet mud on flow characteristics. In this thesis we will compare results from two experiments. In the first experiment the granular material consisted of gravel and only water as the interstitial fluid. In the second experiment, the gravel composition was the same as the first experiment but the interstitial fluid consisted of considerable amount of fine particles(see Table 5.1). In this thesis, the first experiment is referred to as GRAVEL+WATER while the second experiments is referred to as GRAVEL+MUD. The GRAVEL+MUD mixture has the highest content of fines of all the other experiments. The total mass of the

mixtures, including the interstitial fluid, is about 1100 kg.

The drum used is the same as the bigger experimental drum described in Chapter 4. Most of the instrumentation is the same, though there are a few exceptions. In these experiments pore pressure and velocity measuring probes were used in addition to the stress and longitudinal profile measuring devices described in Chapter 4. A pair of pore pressure measuring devices were attached to the drum bed. A pore pressure measuring probe was also used to measure the pore pressure at different depths of the flow. A velocity measuring probe is also used to measure the velocities at different depths of the flow; and hence measure the velocity profile (see ref. [185] for details of the measuring devices). These measurements were performed with the drum filled only to a very low level - similar to that described in Chapter 4 - and rotated at different rotational speeds of the drum (ω = 3, 6, and 9 rpm).

Figure 5.5 shows the experimental results for the longitudinal surface profile and the velocity profile for the GRAVEL+WATER and GRAVEL+MUD mixtures. The results shown are for drum rotational speed ω = 6rpm. The results indicate the presence of fine particles affect the measured profiles. The surface slope (repose angle) is lower for the GRAVEL+MUD mixture than for the GRAVEL+WATER mixture. This result indicate that the GRAVEL+MUD mixtures has a higher mobility than the GRAVEL+WATER mixtures. This is similar to the observed behavior in a natural granular flow referred to as longer run out distances, typical of granular materials in the presence of fine particles. The exact cause of higher mobility in the presence of fines is not yet known. Some researchers have reasoned that the higher mobility may be caused by the lubrication effect of the fines that allows the gravel particles to slide past each other easily [73]. Others have hypothesized that this long-runout phenomenon is due to the increased pore pressure due to the presence of fine particles in sheared or compressed granular materials [2]. In our experiments we have measured an elevated pore pressure, that is, one that is higher that than the expected based on the hydrostatic pressure in the presence of fine particles [185]. In both assumptions the content of fines reduces the repose angle of the granular flows. As shown in Fig. 5.5 the fine content also changes the velocity profile of the granular flows. The change in velocity profile is more apparent close to the surface of the flow. The magnitude of the velocity close to the surface is lower for the GRAVEL+MUD mixture. The velocity profile for this mixture slightly

resembles the plug flow, which is usually associated with velocity profile of Bingham fluids.

5.5 Saturated granular flows: DEM simulations

For this research, the main goal of the DEM simulations of saturated granular flows was to identify the minimal parameters that will reproduce the observations in the rotating drum experiments of saturated granular flows qualitatively. To do so, we incorporated the lubrication model and other fluid effects to the DEM. Our adaption of the lubrication model is similar to eq. 5.4. However, there are two minor modifications associated with $\tilde{h}_{ij}$ in the equation. In the original equation $\tilde{h}_{ij}$ is the separation distance between the interacting particles. F_ν approaches to infinity when the two particles are in contact ($\tilde{h}_{ij} \rightarrow 0$). Therefore, the particles do not actually contact based on the original equation (eq. 5.4). However, particles may contact in real dense granular flows [184]. To accommodate particle contacts in these types of models, we modified $\tilde{h}_{ij}$ by using the distance between the centers and refer to this distance as h_{ij} ($h_{ij} = \tilde{h}_{ij} + d$) (Fig. 5.6). This assumption maintains the qualitative aspect of the original equation and will not alter the quantitative results significantly (See Figure 5.7). To overcome the particle contact issue, others [184] have set a limit for a maximum value for F_ν. The maximum value is set by assuming a certain h_{ij} associated with the estimated measure of roughness of particles, below which F_ν remains constant. Our model does not require any assumptions about the roughness of the particles. The second modification is associated with the lack of clarity of the maximum value of h_{ij} where F_ν has significant effect on the flow dynamics. We compute F_ν between two particles only when h_{ij} is less than d. Fig. 5.6 shows the cutoff distance below which F_ν between two particles is added to the DEM model. Considering F_ν when h_{ij} is less than d ensures that no lubrication force between two particles is calculated when a third particle is located between those two particles. An additional benefit to limiting the maximum value of h_{ij} for which F_ν is calculated is reduction in the computation time.

In the following we use Eq.5.4 in the form of $F_\nu = k\frac{v_{ij}}{h_{ij}}$, where in terms of the rigorously defined lubrication model, $k = \frac{3}{8}\pi d^2 \eta_f$. Fig. 5.9 shows the evolution of F_ν and h_{ij} for different values of k. $k = 1.0$ is for d =1.0 mm particles and $\eta_f = 1.0$ Poise

(viscosity equivalent of glycerine). The figure shows results for particles with a unit radius and initial relative particle velocity of v= 2.0. (The length is nondimensionalised by 0.0005m (radius of 1 mm particle), mass is nondimensionlised by the mass of size 1 mm and density 2650 kg/m^3 particle, and time is nondimensionlised by $\sqrt{d/2g}$, where g is the gravitational acceleration and d is the size of particle (1 mm)). At lower value of k ($k \leq 0.1$) the particles rebound after contact and move beyond the cut off distance for the lubrication model. At intermediate values of k ($1.0 \leq k < 2.0$), the particles collide but stop before they move beyond cut off distance. At higher values of k the particles do not even touch; all of the initial kinetic energy is dissipated due to the high viscosity of the fluid.

This framework was added to the dry particle force model introduced in Chapter 1, and the dynamics were studied rotating particles in a drum in a similar configuration to those described in Section 5.2 and in Chapter 4. The rotating drum is same as the drum shown in Fig. 4.3. The speed of rotation is $\omega = 6.0rpm$. Figure 5.9 shows the longitudinal surface profile for different values of k from DEM simulations of dense granular materials in a rotating drum. Changing the value of k does not alter the longitudinal surface profile in most locations. The effect of k on the longitudinal profile is clearly seen only at the front of the flow. The front of the flow retract towards the back of the flow as k is increased (e.g. as viscosity is increased). These results are opposite to the trend we have measured in the physical experiments (Fig. 5.5).

Fig. 5.10 shows the velocity profile for different values of k. For $k = 10.0$ the maximum velocity is slowed by approximately 30% compared to the velocity profile where $k = 1.0$. More notably, however, there is a qualitative difference with the addition of the lubrication model. The flow profile concavity has changed and it resembles slightly more the plug flow expected by excess pore pressure effects and observed in experimental flows in the physical experiments.

Adding the lubrication model described above is not sufficient to capture some of the kinematic measurements in experiments. It is obvious that other types of particle-fluid interactions are important. One major effect of the fluid on the particles that is missing in the model is the effect of buoyancy forces. The buoyancy force is due to the static pressure gradient normal to the free surface. In any type of flow, the free surface is an equipotential surface where the pressure is zero (neglecting atmospheric pressure).

The static pressure increases linearly in the direction perpendicular to the free surface. The diagram in Fig. 5.11 shows the direction and magnitude of the buoyancy force in a typical rotating drum set-up. The net force on a particle (F_b) due to the static pressure is computed as follows:

$$F_b = (p + \mathrm{dp})\mathrm{A} - \mathrm{pA} \tag{5.5}$$

where p is the static pressure, dp is the pressure difference across the particles and A is the projected surface area of the particle ($A = \frac{\pi}{4}d^2$). $dp = \rho_f g dA$, where d is the size of particle and ρ_f is the density of the fluid. It follows,

$$F_b = m_f g. \tag{5.6}$$

m_f is the mass of fluid of volume equal to particle volume. The direction of F_b is always perpendicular to the free surface of the flow.

We incorporated the buoyancy force to the DEM model of the granular flows in the rotating drum. In adapting this extra force into the simulations, we assume the slope of the free surface is uniform at all locations (see Fig. 5.12). However, we do not know the slope of the free surface a priori. We start with a simulation set-up where the slope is zero (perpendicular to the direction of gravity). Then, as the slope of the free surface changes in the simulation, we allow the direction of F_b to change accordingly. When the flow reaches a steady state we measure the longitudinal and velocity profiles. Fig. 5.12 show the longitudinal profile for different combinations of k and ρ_f. In general, as ρ_f increases the angle of repose decreases. This trend is the same as the results observed in the experiments. Fig. 5.13 shows the velocity profile for the results shown in Fig. 5.12. In each case, the profile is measured at the deepest part of the flow. The changes in ρ_f do not change the velocity profile.

5.6 Summary

In this chapter we reviewed various ways of modeling wet, dense granular flows. Modeling wet granular flows is more complicated than modeling dry granular flows. The major challenge in modeling wet granular (slurry) flows is the lack of a good model for the particle-fluid interactions. For dense granular flows the difficulty of modeling particle-fluid interactions is further complicated by the enduring contacts of particles. In

such flows both the particle-particle and fluid-particle interactions are very important. Therefore, it is ideal to use a model which incorporates the particle-particle interaction via DEM and simple fluid-particle interaction model. In this research we modified the interaction of particles based on lubrication models. Adding the lubrication model to DEM is fairly simple compared to coupling CFD and DEM. The lubrication model does not require solving the flow field of the fluid or tracking the fluid. The lubrication model by itself is not sufficient to retrieve the qualitative results observed in the experiments. The effect of buoyancy is necessary to reproduce similar results as those of the experiments. This model showed the reduction of velocity in wet granular flows is associated with the viscosity of the fluid: the maximum velocity decreases as viscosity increases. On the other hand, the changes in the repose angle of the granular material is due to the change in the density of the fluid: repose angle reduces as density of the fluid increases. In our model the fluid has, by default, no resistance to shear. Therefore, as the density of the fluid is increased the granular mixture tends to be less shear resistant, resulting in a lower angle of repose. The combined effect of the lubrication model and the buoyancy model makes it possible to get qualitatively similar longitudinal surface and velocity profiles to those measured in the physical experiments.

5.7 Acknowledgements

We thank William E. Dietrich, Roland Kaitna and Marisa C. Palucis for collaboration in the experiments and for helpful discussion on the modeling. Roland Kaitna, Marisa C. and Bereket Yohannes worked on the experiments. We thank Stuart Foster for helping in the experiments.

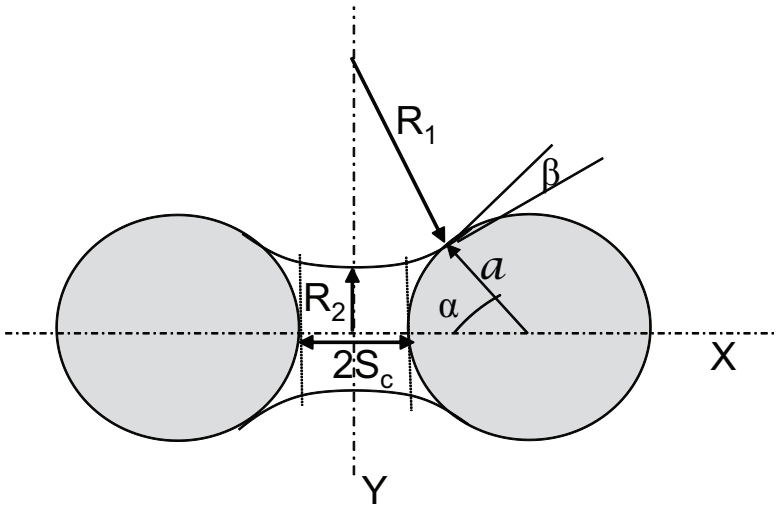

Figure 5.1: Schematics showing a liquid bridge between two particles of radius a. R_1 and R_2 the longitudinal and meridian radius of curvature the liquid bridge. α is the half filling angle, which is the angle formed by the line connecting the centers of the two particles and the line connecting the center of one particle to the junction of the liquid bridge. β is the contact angle formed by contact point between the liquid bridge and the surface of the particle. S_c is half the separation distance between the surface of the two particles.

Table 5.1: Particle size distribution for the GRAVEL+MUD mixture in the experiments described in Section 5.4

size (mm)	name	GRAVEL+MUD mass(kg)	Gravel+WATER mass(kg)
0.0015	Hydrite 121	25.0	0.0
0.0077	DB Float	25.0	0.0
0.022	Silcosil 125	76.0	0.0
0.4	Sand ♯60	51.0	0.0
1.0	Sand ♯1C	51.0	0.0
4.0	Course Aquarium	64.0	64.0
7.0	PAMI 1/4" gravel	64.0	64.0
10.0	PAMI 3/8" gravel	127.0	127.0
13.0	PAMI 1/2" gravel	101.0	101.0
21.0	PAMI 3/4"	101.0	101.0
25.0	Quartzite gravel	102.0	102.0
47.0	Mexican pebbles sm	102.0	102.0
55.0	Mexican pebbles lg	66.0	66.0
Mass of water(kg)		91	177

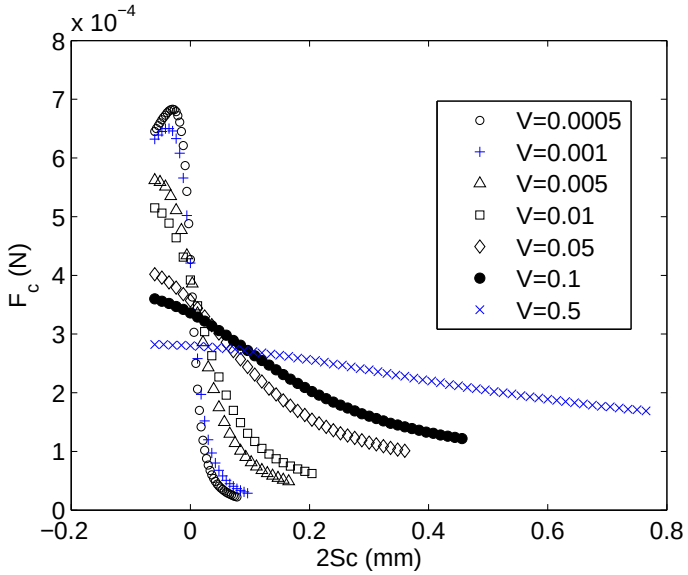

Figure 5.2: Cohesive force (F_c) as a function of the separation distance ($2S_c$) due to a liquid bridge formed between two 2 mm particles. V is volume of liquid bridge.

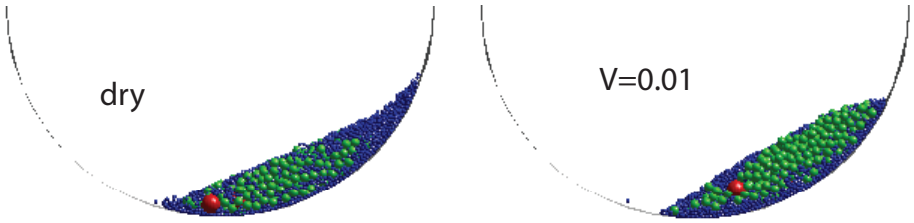

Figure 5.3: Snapshots from simulations of granular flows in a rotating drum. The flows consists of 1.25mm, 3.0mm and 6.25mm particles in a 140mm diameter drum. The speed of rotation Ω of the drum is 48 rpm.

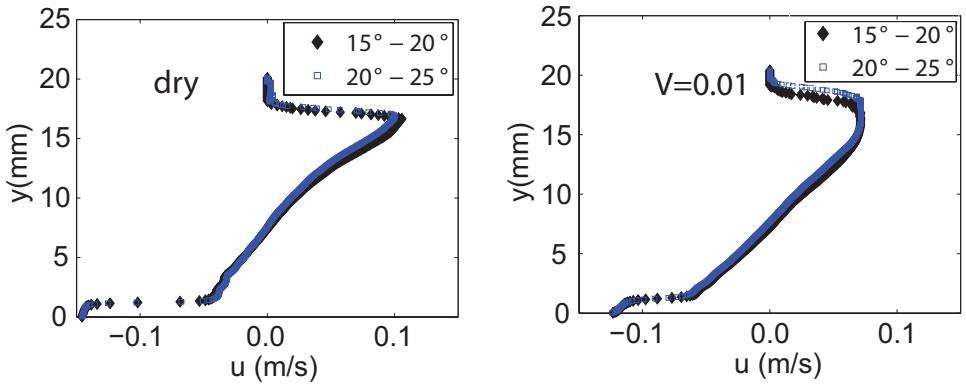

Figure 5.4: Velocity profiles from two different locations in the model debris flows depicted in Fig. 7(a) without and (b) with 2% interstitial fluid. Results from two different positions in the drum are shown for values of θ indicated in the legend.

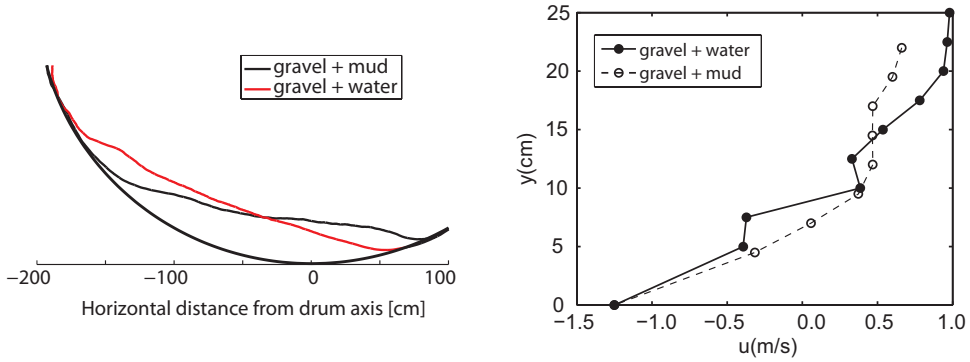

Figure 5.5: Longitudinal profiles (a) and velocity profiles (b) for experiments of MIXTURE+WATER and MIXTURE+MUD mixtures. The composition of the mixtures is as shown in Table 1.1

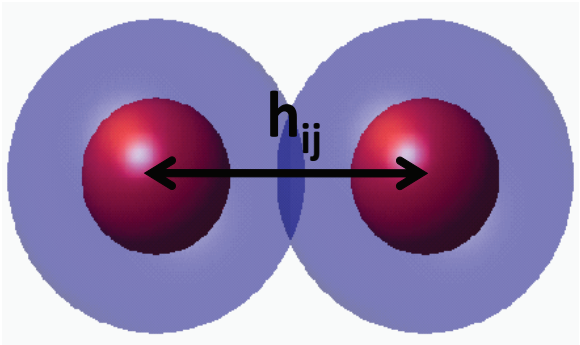

Figure 5.6: Schematics of the lubrication model used to model the interaction between particles in saturated granular flows. h_{ij} is the center to center distance between the particles.

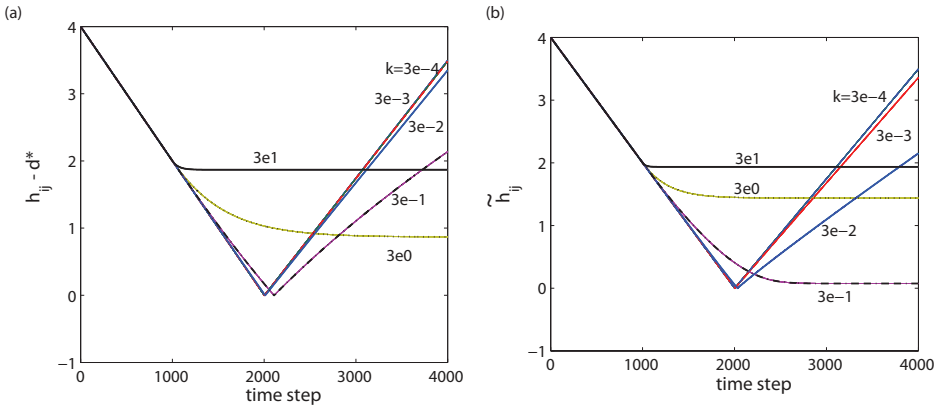

Figure 5.7: (a) $h_{ij} - d^*$ vs. time step for collision of two particles computed using the "modified" lubrication model used in this thesis. d is the diamter of the particles ($d = 2.0$). (b)$\tilde{h}_{ij}$ vs. time step for collision of two particles computed using the lubrication model.

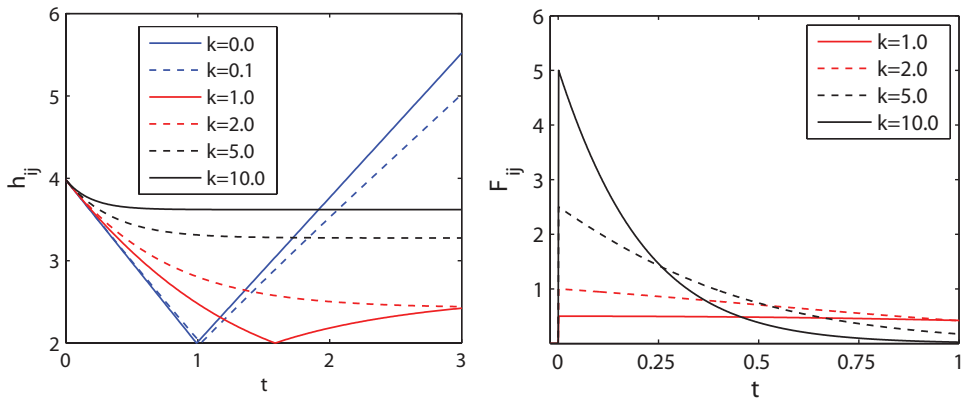

Figure 5.8: The evolution of the separation distance h_{ij} (a) and the lubrication force F_{ij} (b) for head on collision between two particles. The plots are for different value of k ($k = \frac{3}{8}d^2\eta_f$)

.

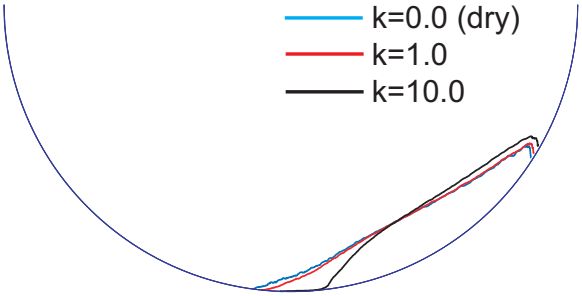

Figure 5.9: Longitudinal surface profiles of granular flow in the bumpy rotating drum simulation using the lubrication model. The particles have $\rho = 2650\ kg/m^3$ and $d = 10\ mm$. The plots are for different values of k as shown in the legend and $\rho_f = 0.0$.

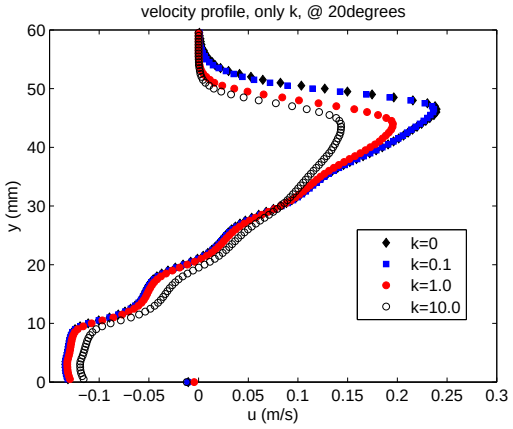

Figure 5.10: Velocity profiles of granular flow in the bumpy rotating drum simulation using the lubrication model. The particles have $\rho = 2650\ kg/m^3$ and $d = 10\ mm$. The plots are for different values of k as shown in the legend and $\rho_f = 0.0$.

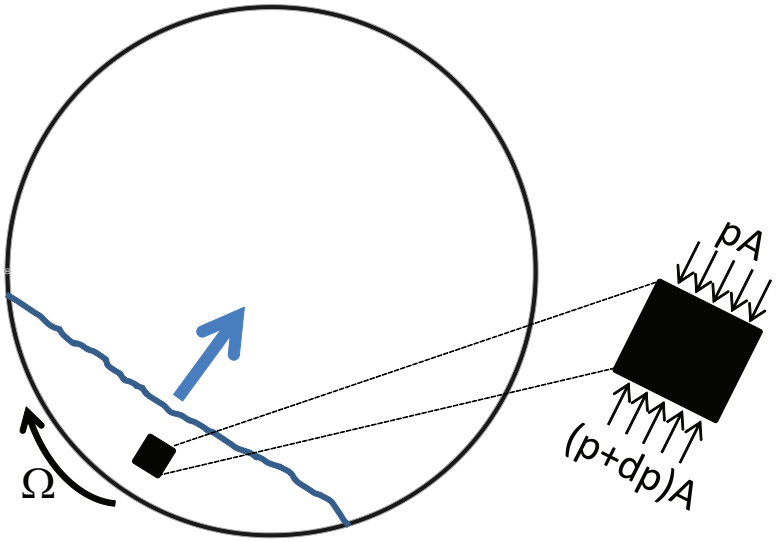

Figure 5.11: Schematics showing the effect of buoyancy on granular flows in a rotating drum. p is static pressure, dp is the static pressure difference at top and bottom of the particle, and A is the projected area of the particle.

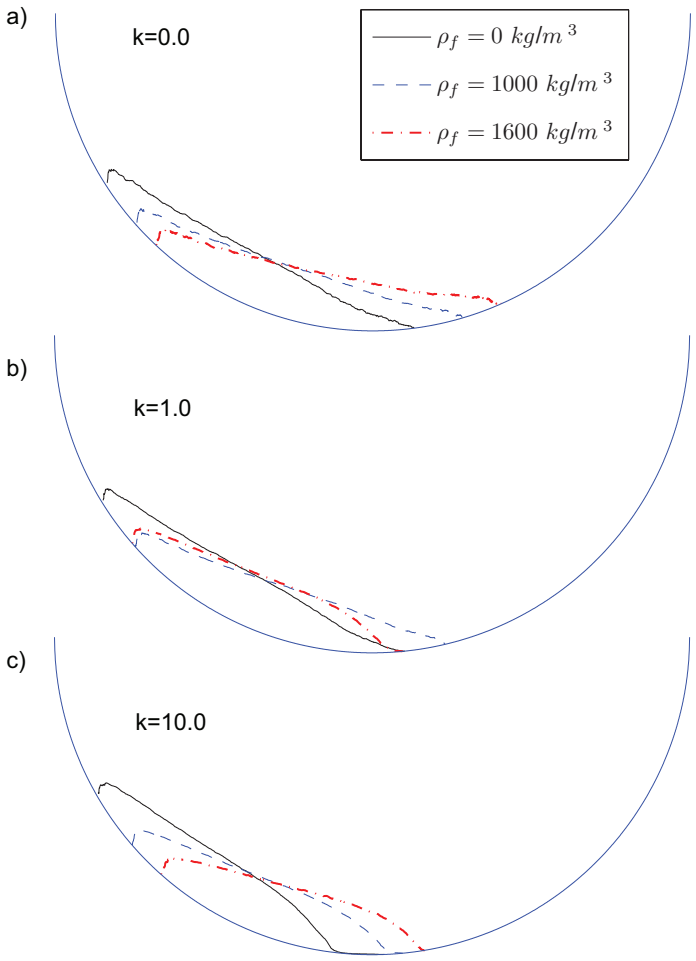

Figure 5.12: Longitudinal surface profiles of granular flow in the bumpy rotating drum simulation using combination of the lubrication model and effect of buoyancy. The plots are for different values of k and ρ_f as shown in the legend.

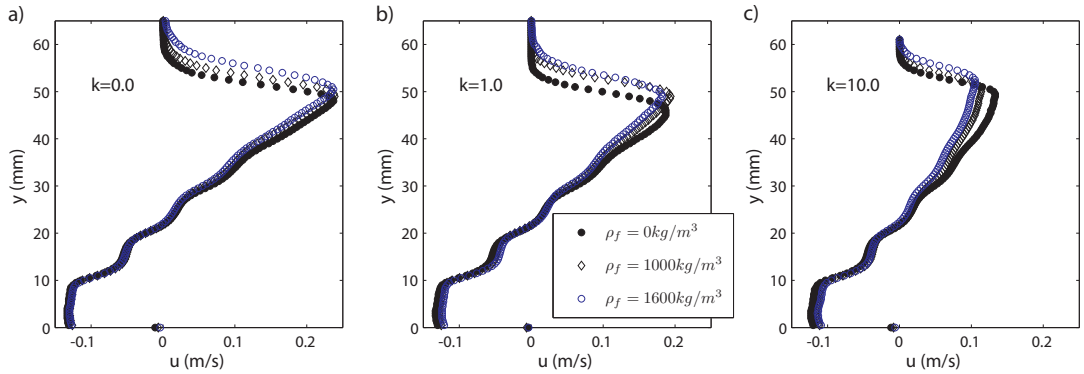

Figure 5.13: Velocity profiles of granular flow in the bumpy rotating drum simulation using combination of the lubrication model and effect of buoyancy. The plots are for different values of k and ρ_f as shown in the legend. The velocity is measured at the deepest location of the flows.

Chapter 6

Conclusion and Future Work

Our research was inspired by the importance and pervasiveness of dense granular flows in natural and industrial processes, their interesting and complex behavior particularly when comprised of particulate mixtures and fluids, and the lack of models capable of predicting, even qualitatively, the dynamics of dense sheared granular mixtures. In this thesis we have focused on four aspects of dense sheared granular flows:

1. The effect of particle size distribution on the boundary stresses in dense sheared granular mixtures (Chapters 2- 3)

2. The effect of particle size distribution on the rheology of dense sheared granular mixtures (Chapter 3).

3. The effect of particle size distribution on boundary stresses and forces due to shallow sheared granular mixtures relevant to debris flow bedrock incision (Chapter 4).

4. The effect of interstitial fluid properties on macroscopic flow behaviors of thin sheared granular materials relevant to saturated and unsaturated debris flows (Chapter 4).

Much of this research was done using discrete element method (DEM) [38] simulations, previously shown to accurately reproduce segregation and flow of dense sheared granular mixtures [121, 186] and here shown also to reproduce key aspects of shallow granular flows in rotating drum simulations (Chapter 4) [1] .

The main findings from this research may be divided into three categories: (1) those with broad applicability to the rheology of dense sheared granular mixtures; (2) those with applicability specific to boundary force statistics associated with shallow free surface granular flows, somewhat similar to debris flows; and (3) those which suggest a method for incorporating the effect of fluids into simple models for thin free surface granular flows. For the first, simulations were performed in simple sheared cells (Couette flow) without gravity where segregation was negligible. For the second and third, simulations and experiments were performed on shallow flows in rotating drums to allow segregation to arise naturally along with other non-uniformities typical of debris flows.

6.1 Rheology of dense sheared granular mixtures

The main findings regarding the rheology of dense sheared mixtures of different sized particles are as follows:

- In general, contrary to what a simple consideration of particle inertia would indicate, the stresses associated with a sheared granular mixture do not have a simple monotonic dependence on the average particle size in a mixture.
  - There is an non-trivial dependence of the stresses on the particle size distribution in a granular mixture.
  - When everything else is held constant (i.e., solid volume fraction, particle properties, and shear rate), the stress depends on how the particle size distribution governs the *packing efficiency* or *maximum potential solid volume fraction* of the granular mixture.
  - This dependence of the stresses on the relative packing faction can be modeled using a relationship between free volume and coordination number (average number of contacts per particle) adapted from a relationship previously derived for the packing of uniform spherical particles near the jammed state [20, 60].
- Recently proposed constitutive laws for effective coefficient of friction in flows of uniform particles [8, 16] are applicable for flows for granular mixtures as well,

though care must be taken to interpret the details within the context of the appropriate boundary conditions.

  - Under constant pressure conditions the effective friction coefficient and the inertial number increase mildly with the average particle size.
  - Under constant volume conditions, on the other hand, the effective friction coefficient and the inertial number exhibit a non-monotonic dependence on the average particle size that is related to the proximity of the system solid fraction to the maximum packing fraction.
  - The relationship between the effective coefficient of friction and the non-dimensionalized shear rate (a generalized Inertial number) is the same for either set of boundary conditions.

- For systems of relatively hard spheres, the particle-scale mechanics that determines the rheological parameters is captured by the ratio between average contact duration and mean-free-path time, also independent of boundary conditions.

  - The inertial number – often interpreted as the ratio of an effective microscopic time scale (time it take particle to rearrange) and macroscopic time scale (shear rate) – can also be used to estimate the ratio of the two microscopic collisional time scales: contact duration and mean-free-path time.

Perhaps the most profound and wide-ranging insights obtained from these results pertain to one of the fundamental differences between monosized granular and systems granular mixtures: the maximum solid volume fraction can vary from one mixture to the next, depending on the particle size distribution. It is tempting to assume that the solid volume fraction is a fundamental variable of a bulk granular material. However, our results demonstrate that for dense sheared granular mixtures, where enduring and multiple simultaneous interparticle contacts govern much of the rheological phenomenology, the dynamics are governed by the *relative* solid volume fraction (relative to the maximum solid volume fraction, that is) rather than the *absolute* solid volume fraction. This relative solid fraction in turn affects the mean free path time of the particles comprising a granular material and the associated macroscopic measures of the rheology.

While our results provide the means for developing appropriate mechanistically-based constitutive laws for the rheology of granular mixtures, there are some limitations to our results that require further research. The applicability of our model relating bulk stresses in granular mixture to average particle coordination number fails in the limit of low solid volume fraction (typically, lower pressures), and high pressures (typically higher solid volume fractions). We hypothesize that the reason our model fails at low relative volume fractions is that multiple enduring contacts no longer dominate the dynamics for these system and therefore the coordination number no longer governs the mechanics of the flow. For the systems we studied, this occurred for absolute solid volume fraction $\nu < 0.5$, and we expect this limit to be higher for systems of higher maximum solid volume fraction than those we studied. We hypothesize that our model fails for very high applied pressures where the coordination number saturates. More work is required to understand the transitions between the regime of dense flow, where our model for bulk stresses works, to more gas-like flows on the one hand and more solid-like deformations on the other, and to extend our model a bit further into these other regimes. In addition, more work is required to enable our model for bulk stresses to be used to predict the behavior in physical granular flows. In DEM simulations, the coordination number is readily available, but in physical granular flows obtaining the coordination number is a daunting task. Therefore, the direct application of our model to physical granular flows requires a way to predict the coordination number from more accessible physical parameters.

The relationships we found between the effective friction coefficient, the generalized inertial number, and the ratio of microscopic collisional time scales in sheared granular mixtures appears to have somewhat broader applicability than the model for the bulk stresses. However, the model appeared to break down in ways associated with boundary roughness conditions. If the roughness was too course, the boundaries trapped smaller particles in a way that was unaccountable in the model. If the roughness was too fine, the particles slipped along the boundary so the generalized inertial number no longer accurately described a measure representative of the entire system. This limits the practical applicability of the model for a broad range of particle size distributions and boundary roughness conditions. More work needs to be done to account for these practical limitations.

6.2 Boundary stresses in shallow granular flows

The main findings regarding the boundary stress due to shallow granular flows:

- The Discrete Element Method (DEM) simulations are capable of producing physically reasonable particle size spatial distributions and boundary stresses associated with shallow granular flows.
- The average normal stress is equivalent to the hydrostatic/lithostatic pressure due to the weight of the granular mixture. The average normal stress in the shallow granular flows depends on the particle size distribution of the granular mixture only as the particle size distribution alters the distribution of the bulk material along the bed.
- The particle size distribution affects the magnitude and the probability distribution function of individual particle-wall contact forces.
  - The magnitude of the individual particle-wall contact forces (e.g., maximum and average boundary forces) increase with the local average particle size
  - Since the large particle segregate to the front of the flow, the individual particle-wall contact forces are higher at the front of the flow
- The largest particle-wall contact forces are due to isolated impacts from a single particle
  - The impact forces are proportional to the particle diameter squared and the 1.2 power of the impact velocity – similar to predictions from Hertzian contact theory for elastic particles
  - Almost all contact forces at the front of the flow are associated with impacts from particles, while pure impact forces are absent in the other parts of the flow.

These results indicate that the individual particle-bed contact forces are very important in determining the mechanics of the shallow granular flows. On the other hand the average stress is only a function of the depth of the flow, hence not directly affected

by the particle size distribution. In natural granular flows, such as debris flows, with a wide particle size distribution, field data support many of these results, particularly that the larger particles segregate to the front of the flow and give rise to larger contact forces at the front of the flow than further back in the flow.

Field measurements further demonstrate that the larger contact forces at the front of the flow likely drive bed erosion and bed rock incision due to debris flow [129, 102, 128]. In their field measurement Berger et al.([129]) have found that most of the bed erosion occur at the front of the flow. The higher erosion at the front of the flow is clearly associated with their measurements of higher magnitude of contact forces at the front of the flow. An important step in predicting the amount of erosion due to granular flows is to formulate mechanistic model for the magnitude of contact forces. Our results have shown this relationships predicted from Hertzian contact theory for small deformations of elastic spheres. Specifically, the maximum particle-bed forces are proportional to the square of the particle size and the impact velocity to the power 1.2. To complete the prediction of impact forces for a given granular mixture and boundary condition, it is important to be able to predict the impact velocities of the particles. In our simulations the impact velocity varies between 0-1.5m/s (for drum rotational speed of 12rpm). Even a rough estimate of the statistical distribution of impact velocities will allow prediction of erosion due to a given granular mixture without running experiments or simulations.

6.3 Effect of interstitial fluid on granular flows

The main findings regarding the effect of interstitial fluid on the characteristics of dense granular flows are as follows:

- For lower moisture content, i.e., unsaturated granular flows, the associated attraction force between particles affects the granular flows in the following ways:
  - The repose angle increases, which indicates reduced mobility
  - The particle segregation is more distinct
  - The magnitude of the velocity is reduced, especially near the surface of the flow, and the shear rate is reduced throughout the flow.

- Large scale experiments of granular flows with higher moisture content, i.e., saturated granular flows, provide two key macroscopic measures of the kinematics of dense granular flows that represent how properties of the interstitial fluid affect the system dynamics. When fluid of a higher density and higher viscosity replaces another interstitial fluid (e.g., when mud replaces water):
  - the repose angle (surface slope) decreases, which indicates increased mobility of the granular mixtures.
  - the velocities decrease near (or especially) at the surface of the flow and the flow becomes more plug-like.
- A model that includes limited modification of the particle-particle interactions based on lubrication model and consideration of buoyancy forces, and therefore accounting explicitly only for density and viscosity of the fluid, captures some of the experimental results for flows of saturated granular materials.
  - The model shows the reduced repose angle is associated with the density of the interstitial fluid.
  - The model shows the reductions in the magnitude of the velocity and the magnitude of the shear rate are associated with are associated with the viscosity of the interstitial fluid.

In this thesis we focused mainly on developing a simple model that could capture the kinematics measured in experiments of saturated dense granular flows. Our model has incorporated the effects of viscosity of the interstitial fluid and buoyancy effects due to the density of the interstitial fluid. The combined effect of viscosity and buoyancy explains the variations of surface slopes and velocity profiles for granular flows containing different amounts of fine particles and water. Though our model is relatively simple, the results from the model are in qualitative agreement with the large scale experiments we performed. Perhaps even more profoundly, in our simulations we were able to investigate the effect of viscosity and density of interstitial fluid separately. The results indicate that and increased mobility of saturated granular flows – often associated with pore pressures greater than hydrostatic pore pressures – may arise only from the buoyancy

effected associated with a denser interstitial fluid such as mud. It is clear that significant improvements in the model are required before using this model to predict quantitatively accurate kinematics and dynamics of saturated granular flows. The main limitations of our current model includes:

- We have assumed two particles interact at a 'long-range' provided the separation distance between the two particles is no more than particle diameter. This assumption needs to be verified, perhaps using careful experiments of collision of particles immersed in liquid.
- The effects of other 'long-range' interactions among many particles, such as those associated with fluid movement through pore spaces, needs to be considered for a more realistic model.
- We have considered a constant viscosity of the interstitial fluid. If this model is to be applied to flows where the interstitial fluid is non-Newtonian as is typical for natural mud in debris flows, the effect of shear rate on the local viscosity needs to be incorporated to the model.
- Even for the application of our model limited to two-particle 'long-range' interactions the effect of particle size distribution on the lubrication model parameters needs to be determined to further improve the broader applicability of our model. For this thesis, the application of the lubrication model is limited to single-sized particles.

In conclusion, in this thesis we have taken crucial first steps in modeling and understanding the effects of particle size distribution and moisture in dense granular flows. We have explored these effects in the idealized Couette cell boundary conditions and the more widely applicable free surface flows in rotating drums. Our results provide some important relationships between the particle size distribution and rheology of granular mixtures and physical intuition for some observations made in particle-fluid flows of granular mixtures. Our research was primarily limited to the study of uniform size particles and binary mixtures. More research is still required determine the breadth

and limitations of the models we propose on a wider range of systems. One of the next important steps is to validate our findings for wide particle size distributions, which are common in nature. Another step for applying our saturated DEM model to predict the behavior of real slurry flows is to calibrate parameters in our model so that it is possible to get quantitatively sound predictions comparable to the physical experiments. The ultimate goals of performing this research was to establish (1) a constitutive law to predict the rheology of dense granular mixtures given only the particle size distribution and important boundary conditions (2) develop a framework for predicting the impact forces associated with these flows, which are crucial to estimate the bed erosion and bed rock incision and (3) develop a better understanding of the effect of certain liquid properties on the characteristics of free surface saturated and unsaturated granular flows. This thesis contributes essential first steps towards achieving these ultimate goals.

References

[1] B. Yohannes, L. Hsu, W. E. Dietrich, and K. M. Hill. Boundary stresses due to impacts from dry granular flows. *JGR-ES*, 117:F02027, 2012.

[2] R. Iverson. Physics of debris flows. *Rev. Geophysics*, 35:245, 1997.

[3] R. A. Bagnold. An approach to the sediment transport problem from general physics. *US Geol. Surv., Profess. Papers*, 422:235–297, 1966.

[4] H. M. Jaeger, S. R. Nagel, and R. P. Behringer. The physics of granular materials. *Rev. Mod. Phys.*, 68:1259, 1996.

[5] A. Daerr and S. Douady. Two types of avalanche behaviour in granular media. *Nature*, 399:241, 1999.

[6] O. Pouliquen. Scaling laws in granular flows down rough inclined planes. *Phys. of Fluids*, 11(3):542–548, 1999.

[7] C. S. Campbell. Stress-controlled elastic granular shear flows. *J. Fluid Mech.*, 539:273–297, 2005.

[8] GDR MiDi. On dense granular flows. *Eur. Phys. J. E*, 14:341, 2004.

[9] S. B. Savage. Gravity flow of cohesionless granular materials in chutes and channels. *J. Fluid Mech.*, 92(01):53–96, 1979.

[10] O. Reynolds. On the dilatancy of media composed of rigid particles in contact, with experimental illustrations. *Phil. Mag., Series*, 5:469–481, 1885.

[11] R. A. Bagnold. Experiments on a gravity-free dispersion of large solid spheres in a newtonian fluid under shear. *Proceedings of the Royal Society of London. Series A*, 225:49–63, 1954.

[12] C. Campbell and C. Brennen. Computer simulations for granular shear flows. *J. Fluid Mech.*, 151:167–188, 1985.

[13] J. T. Jenkins and S. B. Savage. A theory for the rapid flow of identical, smooth, nearly elastic, spherical particles. *J. Fluid Mech.*, 130:187–202, 1983.

[14] H. M. Jaeger, S. R. Nagel, and R. P. Behringer. The physics of granular materials. *Physics Today*, 49(40):32–38, 1996.

[15] L. P. Kadanoff. Built upon sand: Theoretical ideas inspired by granular flows. *Rev. Mod. Phys.*, 71:435–444, 1999.

[16] Y. Forterre and O. Pouliquen. Flows of dense granular media. *Annu. Rev. Fluid Mech.*, 40:1–24, 2008.

[17] R. M. Nedderman. *Statics and Kinematics of Granular Materials*. Cambridge University Press, Cambridge, 1992.

[18] T. S. Majmudar and R. P. Behringer. Contact force measurements and stress-induced anisotropy in granular materials. *Nature*, 435:1079–1082, 2003.

[19] A. Drescher and G. De Josselin de Jong. Photoelastic verification of a mechanical model for the flow of a granular material. *J. Mech. Phys. Solids*, 20:337, 1972.

[20] C. Song, P. Wang, and H. Makse. A phase diagram for jammed matter. *Nature*, 458:629, 2008.

[21] P. Patricio. The hertz contact in chain elastic collisions. *Am. J. Phys.*, 72:1488–1491, 2004.

[22] M. Alam and S. Luding. Rheology of bidisperse granular mixtures via event-driven simulations. *J. Fluid Mech.*, 476:69–103, 2003.

[23] S. B. Savage. Analysis of slow high-concentration flows of granular materials. *J. Fluid Mech.*, 377:1–26, 1998.

[24] A. K. Reddy and V. Kumaran. Applicability of constitutive relations from kinetic theory for dense granular flows. *Phys. Rev. E*, 76:061305, 2007.

[25] M. Y. Louge. Model for dense granular flows down bumpy inclines. *Phys. Rev. E*, 67:061303, 2003.

[26] P. Mills, D. Loggia, and M. Tixier. Model for a stationary dense granular flow along an inclined wall. *EPL*, 45(6):733, 1999.

[27] I. S. Aranson and L. S. Tsimring. Continuum description of avalanches in granular media. *Phys. Rev. E*, 64:020301, 2001.

[28] R. Brewster, L. E. Silbert, G. S. Grest, and A. J. Levine. Relationship between interparticle contact lifetimes and rheology in gravity-driven granular flows. *Phys. Rev. E*, 77:061302, 2008.

[29] L. E. Silbert, G. S. Grest, R. Brewster, and A. J. Levine. Rheology and contact lifetimes in dense granular flows. *Phys. Rev. Lett.*, 99:068002, 2007.

[30] O. Pouliquen, C. Cassar, Y. Forterre, P. Jop, and M. Nicolas. Flow of dense granular material: towards simple constitutive laws. *J. of Stat. Mech.: Theory and Experiment*, page P07020, 2006.

[31] P. Jop, Y. Forterre, and O. Pouliquen. A constitutive law for dense granular flows. *Nature*, 441:727, 2006.

[32] O. Pouliquen. Velocity correlations in dense granular flows. *Phys. Rev. E*, 93:248001, 2004.

[33] F. da Cruz, S. Emam, M. Prochnow, J.-N. Roux, and F. Chevoir. Rheophysics of dense granular materials: Discrete simulation of plane shear flows. *Phys. Rev. E*, 72:021309, 2005.

[34] S. B. Savage and M. Hutter. The motion of a finite mass of granular material down a rough incline. *J. Fluid Mech.*, 199:177–215, 1989.

[35] S. B. Savage and M. Hutter. The dynamics of avalanches of granular materials from initiation to runout. part i: Analysis. *Acta Mechanica*, 86:201–223, 1991.

[36] C. Ancey, P. Coussot, and P. Evesque. A theoretical framework for very concentrated granular suspensions in a steady simple shear flow. *J. Rheology*, 43:1673–1699, 1999.

[37] P. Jop, Y. Forterre, and O. Pouliquen. Crucial role of sidewalls in granular surface flows: consequence for the rheology. *J. Fluid Mech.*, 541:167–192, 2005.

[38] P. A. Cundall and O. D. L. Strack. A discrete numerical model for granular assemblies. *Geotech.*, 29:47–65, 1979.

[39] H. R. Hertz. On contact between elastic bodies. *in Gesammelte Werke (Collected Works)*, 1, 1885.

[40] R. D. Mindlin and H. Deresiewicz. Elastic spheres in contact under varying oblique forces. *J. Applied Mech.*, 20:327–344, 1953.

[41] K. L. Johnson. *Contact mechanics*. Cambridge University Press, 1985.

[42] Y. Tsuji, T. Tanaka, and T. Ishida. Lagrangian numerical simulation of plug flow of cohesionless particles in horizontal pipe. *Powder Tech.*, 71:239–250, 1992.

[43] H. Kruggel-Emden, M. Sturm, S. Wirtz, and V. Scherer. Election of an appropriate time integration scheme for the discrete element method (DEM). *Computers and Chemical Engineering*, 32:2263–2279, 2008.

[44] P. Coussot and M. Meunier. Recognition, classification and mechanical description of debris flows. *Earth Science Rev.*, 40:209, 1996.

[45] T. Takahashi. *Debris Flow: Mechanics, Prediction and Countermeasures*. Taylor and Francis group, London, 2007.

[46] L. Hsu, W. E. Dietrich, and L. S. Sklar. Experimental study of bedrock erosion by granular flows. *J. Geophys. Res.*, 113:F02001, 2008.

[47] Y. Zhong and K. Minemura. Measurement of erosion due to particle impingement and numerical prediction of wear in pump casing. *Wear*, 199:36–44, 1996.

[48] P. C. Johnson and R. Jackson. Frictional collisional constitutive relations for granular materials, with application to plane shearing. *J. Fluid Mech.*, 176:67, 1987.

[49] S. B. Savage and D. J. Jeffrey. The stress tensor in a granular flow at high shear rates. *J. of Fluid Mech.*, 110:255–272, 1981.

[50] P. K. Haff. Grain flow as a fluid-mechanical phenomenon. *J. Fluid Mech.*, 134(2):401, 1983.

[51] M. Massoudi. On the flow of granular materials with variable material properties. *I. J. Non-Linear Mech.*, 36:25–37, 2001.

[52] M. Massoudi and M. M. Mehrabadi. A continuum model for granular materials: Considering dilatancy and mohr-coulumb critrea. *Acta Mechanica*, 152:121–138, 2001.

[53] S. Torquato. Nearest-neighbor statistics for packings of hard spheres and disks. *Phys. Rev. E*, 51:3170–3182, 1995.

[54] J. Jenkins. Dense shearing flows in elastic disks. *Phys. Fluids*, 18:103307, 2006.

[55] C. K. K. Lun and S. B. Savage. A simple kinetic theory for granular flow of rough, inelastic spherical particles. *J. Appl. Mech.*, 54:47, 1987.

[56] C. S. O'Hern, S. A. Langer, A. J. Liu, and S. R. Nagel. Random packings of frictionless particles. *Phys. Rev. Lett.*, 88(7):075507, Jan 2002.

[57] S. Henkes and B. Chakraborty. Jamming as a critical phenomenon: A field theory of zero-temperature grain packings. *Phys. Rev. Lett.*, 95:198002, 2005.

[58] T. S. Majmudar, M. Sperl, S. Luding, and R. P. Behringer. Jamming transition in granular systems. *Phys. Rev. Lett.*, 98:058001, 2007.

[59] J. Zhang, T. Majmudar, A. Tordesillas, and R. Behringer. Statistical properties of a 2d granular material subjected to cyclic shear. *Granular Matter*, 12:159–172, 2010. 10.1007/s10035-010-0170-2.

[60] T. Aste, M. Saadatfar, and T. J. Senden. Local and global relations between the number of contacts and density in monodisperse sphere packs. *Stat. Mech.*, 2006:p07010, 2006.

[61] L. Silbert, D. Ertas, G. Grest, T. Halsey, D. Levine, and S. J. Plimpton. Granular flow down an inclined plane: Bagnold scaling and rheology. *Phys. Rev. E*, 64:051302, 2001.

[62] L. Silbert, J. Landry, and G. Grest. Granular flow down a rough inclined plane: Transition between thin and thick piles. *Phys. Fluids*, 15(1):1–10, 2003.

[63] D. M. Hanes and D. L. Inman. Observations of rapidly flowing granular-fluids materials. *J. Fluid Mech.*, 150:357–380, 1985.

[64] J. Rajchenbach. Dense, rapid flows of inelastic grains under gravity. *Phys. Rev. Lett.*, 90(14):144302, Apr 2003.

[65] R. Brewster, G. S. Grest, J. W. Landry, and A. J. Levine. Plug flow and the breakdown of Bagnold scaling in cohesive granular flows. *Phys. Rev. E*, 72:061301, 2005.

[66] D. Ertas and T. C. Halsey. Granular gravitational collapse and chute flow. *EPL*, 60(6):931, 2002.

[67] O. Baran, D. Ertas, T. C. Halsey, G. S. Grest, and J. B. Lechman. Velocity correlations in dense gravity-driven granular chute flow. *Phys. Rev. E*, 74:051302, 2006.

[68] A. Karion and M. L. Hunt. Wall stresses in granular couette flows of mono-sized particles and binary mixtures. *Powder Tech.*, 109:145–163, 2000.

[69] B. Yohannes and K. M. Hill. Preliminary investigations on the rheology and boundary stresses associated with granular mixtures. *AIP Conference Proceedings*, 1227(1):379–387, 2010.

[70] B. Yohannes and K. M. Hill. Rheology of dense granular mixtures: Particle-size distributions, boundary conditions, and collisional time scales. *Phys. Rev. E*, 82(6):061301, 2010.

[71] C. S. Campbell. Granular shear flows at the elastic limit. *J. Fluid Mech.*, 465:261, 2002.

[72] O. Pouliquen and J. W. Vallance. Segregation induced instabilities of granular fronts. *Chaos*, 9(3):621, 1999.

[73] E. Linares-Guerrero, C. Goujon, and R. Zenit. Increased mobility of bidisperse granular flows. *J. Fluid Mech.*, 593:475–504, 2007.

[74] J. C. Phillips, A. J. Hogg, R. R. Kerswell, and N. H. Thomas. Enhanced mobility of granular mixtures of fine and coarse particles. *Earth Planet Sci. Lett.*, 246:466–480, 2006.

[75] P. G. Rognon, J.-N. Roux, M. Naaïm, and F. Chevoir. Dense flows of bidisperse assemblies of disks down an inclined plane. *Phys. of Fluids*, 19:058101, 2007.

[76] J. T. Jenkins and F. Mancini. Kinetic theory for binary mixtures of smooth, nearly elastic spheres. *Phys. of Fluids*, 31:2050–2057, 1989.

[77] J. E. Galvin, S. R. Dahl, and C. M. Hrenya. On the role of non-equipartition in the dynamics of rapidly flowing granular mixtures. *J. Fluid Mech.*, 528:207–232, 2004.

[78] V. Garzo, J. W. Dufty, and C. M. Hrenya. Enskog theory for polydisperse granular mixtures. I Navier Stokes order transport. *Phys. Rev. E*, 76:031304, 2007.

[79] H. Xu, M. Louge, and A. Reeves. Solutions of the kinetic theory for bounded collisional granular flows. *Cont. Mech. Thermodyn.*, 15:321–349, 2003.

[80] N. Mitarai and H. Nakanishi. Bagnold scaling, density plateau, and kinetic theory analysis of dense granular flow. *Phys. Rev. Lett.*, 94:128001, 2005.

[81] J. M. Montanero, V. Garzo, M. Alam, and S. Luding. Rheology of granular mixtures under uniform shear flow: Enskog kinetic theory versus molecular dynamics simulations. *Granular Matter*, 8:103, 2006.

[82] S. B. Savage and M. Sayed. Stresses developed by dry cohesionless granular materials sheared in an annular shear cell. *J. Fluid Mech.*, 142:391–430, 1984.

[83] D. V. Khakhar, J. J. McCarthy, and J. M. Ottino. Radial segregation of granular mixtures in rotating cylinders. *Phys. of Fluids*, 9(12):3600–3614, 1997.

[84] K. M. Hill, G. Gioia, and V. V. Tota. Structure and kinematics in dense free-surface granular flow. *Phys. Rev. Lett.*, 91:064302, 2003.

[85] G. Berton, R. Delannay, P. Richard, N. Taberlet, and A. Valance. Two-dimensional inclined chute flows: Transverse motion and segregation. *Phys. Rev. E*, 68:051303, 2003.

[86] S. B. Savage and S. McKeown. Shear stresses developed during rapid shear of concentrated suspensions of large spherical particles between concentric cylinders. *J. Fluid Mech.*, 127:453–472, 1983.

[87] A. D. Rosato and H. Kim. Particle dynamics calculations of wall stresses and slip velocities for couette flow of smooth inelastic spheres. *Cont. Mech. and Thermodyn.*, 6:1–20, 1994.

[88] G. Koval, J.-N. Roux, A. Corfdir, and F. Chevoir. Annular shear of cohesionless granular materials: from the inertia to quasistatic regime. *Phys. Rev. E*, 79:021306, 2009.

[89] F. Chevior, J.-N. Roux, F. da Cruz, P. G. Rognon, and G. Koval. Friction law in dense granular flows. *Powder Tech.*, 190:167–188, 2009.

[90] T. Hatano. Power-law friction in closely packed granular materials. *Phys. Rev. E*, 75:060301, 2007.

[91] P. G. Rognon, J.-N. Roux, D. Wolf, M. Naaïm, and F. Chevoir. Rheophysics of cohesive granular materials. *EPL*, 74(4):644, 2006.

[92] K. M. Hill and B. Yohannes. Rheology of dense granular mixtures: Boundary pressures. *Phys. Rev. Lett.*, 106(5):058302, Feb 2011.

[93] S. Hsiau and M. Hunt. Granular thermal diffusion in flows of binary-sized mixtures. *Acta Mechanica*, 114:121–137, 1996. 10.1007/BF01170399.

[94] I. Iordanoff, K. Elkholy, and M. Khonsari. Effect of particle size dispersion on granular lubrication regimes. *J. Eng. Tribology*, 222:725–739, 2008.

[95] A. W. Lees and S. F. Edwards. The computer study of transport processes under extreme conditions. *J. Phys. C: Solid State Physics*, 5(15):1921, 1972.

[96] C. Goujon, N. Thomas, and B. Dalloz-Dubrujeaud. Monodisperse dry granular flows on inclined planes: Role of roughness. *Eur. Phys. J. E*, 11:147–157, 2003.

[97] C. S. Campbell. Boundary interactions for two-dimensional granular flows. part 1. flat boundaries, asymmetric stresses and couple stresses. *J. Fluid Mech.*, 247:111–136, 1993.

[98] A. Tripathi and D. V. Khakhar. Rheology of binary granular mixtures in the dense flow regime. *Phys. of Fluids*, 23(11):113302, 2011.

[99] D. Kadau, J. Andrade Jr., and H. Herrmann. Collapsing granular suspensions. *Eur. Phys. J. E: Soft Matter and Biological Physics*, 30:275–281, 2009.

[100] M. Y. Louge. Computer simulations of rapid granular flows of spheres interacting with a flat, frictional boundary. *Phys. of Fluids*, 6(7):2253–2269, 1994.

[101] G. F. Wieczorek, B. A. Morgan, and R. H. Campbell. Debris-flow hazards in the blue ridge of central virginia. *Env. and Eng. Geoscience*, 6(1):3–23, 2000.

[102] J. D. Stock and W. E. Dietrich. Erosion of steepland valleys by debris flows. *Geol. Soc. Am. Bull.*, 118(9/10):1125–1148, 2006.

[103] K. X. Whipple and G. E. Tucker. Bedrock rivers and the geomorphology of active orogens. *Ann. Rev. Earth and Planetary Sciences*, 32:151–185, 2004.

[104] L. S. Sklar and W. E. Dietrich. A mechanistic model for river incision into bedrock by saltating bed load. *Water Resources Research*, 40:W06301, 2004.

[105] L. S. Sklar and W. E. Dietrich. Implications of the saltation-abrasion bedrock incision model for steady-state river longitudinal profile relief and concavity. *Earth Surface Processes and Landforms*, 33(7):1129–1151, 2008.

[106] J. M. Turowski, N. Hovius, M. L. Hsieh, D. Lague, and M. C. Chen. Distribution of erosion across bedrock channels. *Earth Surface Processes and Landforms.*, 33(3):353–363, 2008.

[107] J. P. L. Johnson, K. X. Whipple, L. S. Sklar, and T. C. Hanks. Transport slopes, sediment cover, and bedrock channel incision in the Henry Mountains, Utah. *JGR-ES*, 114:F02014, 2009.

[108] J. P. L. Johnson and K. X. Whipple. Evaluating the controls of shear stress, sediment supply, alluvial cover, and channel morphology on experimental bedrock incision rate. *JGR-ES*, 115:F02018, 2010.

[109] D. Lague. Reduction of long-term bedrock incision efficiency by short-term alluvial cover intermittency. *JGR-ES*, 115:F02011, 2010.

[110] K. X. Whipple and G. E. Tucker. Dynamics of the stream-power river incision model: Implications for height limits of mountain ranges, landscape response timescales, and research needs. *J. Geophys. Res.*, 104:17,661–17,674, 1999.

[111] L. S. Sklar and W. E. Dietrich. River longitudinal profiles and bedrock incision models: stream power and the influence of sediment supply. *Rivers over rocks: Geophysical Monograph*, 107:237–260, 1998.

[112] J. D. Stock and W. E. Dietrich. Valley incision by debris flows: evidence of a topographic signature. *Water Resources Research*, 39(4):1089–1104, 2003.

[113] L. Hsu, W. E. Dietrich, and L. S. Sklar. Normal stresses, longitudinal profiles, and bedrock surface erosion by debris flows: initial findings from a large, vertically rotating drum. *Debris-Flow Hazards Mitigation: Mechanics, Predictions, and Assessment*, 2007.

[114] L. Hsu. Experimental study of bedrock erosion by granular flows. *PhD Thesis, University of California, Berekeley*, 2010.

[115] J. D. Stock, D. R. Montgomery, B. D. Collins, W. E. Dietrich, and L. Sklar. Field measurements of incision rates following bedrock exposure: Implications for

process controls on the long profiles of valleys cut by rivers and debris flows. *Geol. Soc. Am. Bull.*, 117:174–194, 2005.

[116] J. D. Rodine and A. M. Johnson. The ability of debris, heavily freighted with coarse clastic materials, to flow on gentle slopes. *Sedimentology*, 23:213–234, 1976.

[117] Y. Oyama. *Bull. Inst. Phys. Chem. Res.*, 246:600, 1939.

[118] J. M. N. T. Gray and A. R. Thornton. A theory for particle size segregation in shallow granular free-surface flows. *Proceedings of the Royal Society A-Mathematical Physical and Engineering Sciences*, 461(2057):1447 – 1473, 2005.

[119] G. Plantard, H. Aadaoui, P. Snabre, and B. Pouligny. Surface-roughness–driven segregation in a granular slurry under shear. *Europhys. Lett.*, 75(2):335–341, 2006.

[120] K. M. Hill, Y. Fan, J. Zhang, C. Van Niekerk, E. Zastrow, S. C. Hagness, and J. T. Bernhard. Granular segregation studies for the development of a radar-based three-dimensional sensing system. *Granular Matter*, 2010.

[121] K. M. Hill and J. Zhang. Kinematics of densely flowing granular mixtures. *Phys. Rev. E*, 77:061303, 2008.

[122] S. S. Hsiau and H. W. Jang. Measurements of velocity fluctuations of granular materials in a shear cell. *Experimental Thermal and Fluid Science*, 17:202–209, 1998.

[123] P. A. Thomas and J. D. Bray. Capturing nonspherical shape of granular media with disk clusters. *J. Geotech. and Geoenv. Eng*, 125(3):169–178, 1999.

[124] J. M. Ting, L. Meachum, and J. D. Rowell. Effect of particle shape on the strength and deformation of mechanism of ellispse-shaped granular assemblages. *Eng. Comp.*, 12:99–108, 1995.

[125] M. Swartz and B. W. McArdell. Motion of large particles in debris flows. *Geophysical Research Abstracts*, 7:05943, 2005.

[126] H. Suwa. Focusing mechanism of large boulders to a debris-flow front. *Transactions, Japanese Geomorphological Union*, 9(3):151–178, 1998.

[127] P. Jalali, J. Ritvanen, and P. Sarkomaa. Stress fluctuations in monodisperse and bidisperse rapid granular shear flows. *Physica A: Statistical Mechanics and its Applications*, 369:535–544, 2006.

[128] L. S. Sklar and W. E. Dietrich. Sediment and rock strength controls on river incision into bedrock. *Geology*, 29(12):1087–1090, 2001.

[129] C. Berger, B. W. McArdell, and F. Schlunegger. Direct measurement of channel erosion by debris flows, illgraben, switzerland. *JGR-ES*, 116:F001722, 2011.

[130] N. Menon and D. J. Durian. Diffusing-wave spectroscopy of dynamics in a three-dimensional granular flow. *Science*, 275:1920–1922, 1997.

[131] P. Jalali, W. Polashenski, T. T. Tynäl̈a, and P. Zamankhan. Particle interactions in a dense monosized granular flow. *Physica D*, 162:188–207, 2002.

[132] D. Lohse, R. Bergmann, R. Mikkelsen, C. Zeilstra, D. van der Meer, M. Versluis, K. van der Weele, M. van der Hoef, and H. Kuipers. Impact on soft sand: Void collapse and jet formation. *Phys. Rev. Lett.*, 93:198003, Nov 2004.

[133] D. Lohse, R. Rauhe, R. Bergmann, and D. van der Meer. Granular physics: Creating a dry variety of quicksand. *Nature*, 432:689, 2004.

[134] C. C. Liao, S. S. Hsiau, and K. To. Granular dynamics of a slurry in a rotating drum. *Phys. Rev. E*, 82(1):010302, Jul 2010.

[135] T. Takahashi. Mechanical characterstics of debris flow. *J. Hydraulics Division*, 104(8):1153–1169, 1978.

[136] T. Takahashi. Debris flow. *Annu. Rev. Fluid Mech.*, 13:57, 1981.

[137] T. Takahashi. *Debris flow.* A. A. Balkema, Brookfield,Vt., 1991.

[138] J. J. Major and T. C. Pierson. Debris flow rheology: Experimental analysis of fine-grained slurries. *Water Resources Research*, 28(3):841–857, 1992.

[139] J. J. Major and R. M. Iverson. Debris-flow deposition: Effects of pore-fluid pressure and friction concentrated at flow margins. *Geol. Soc. Am. Bull.*, 111:1424–1434, 1999.

[140] R. M. Iverson. Surge dynamics coupled to pore-pressure evolution in debris flows. pages 503–514, 2003.

[141] N. Jain, J. M. Ottino, and R. M. Lueptow. Effect of interstitial fluid on a granular flowing layer. *J. of Fluid Mech.*, 508:23–44, 2004.

[142] O. Pouliquen, C. Cassar, Y. Forterre, P. Jop, and M. Nicolas. How do grains flow: towars a simple rheology for dense granular flows. *In: Powders and Grains 2005*, (ed. R. Garcia-Rojo, H. Herrmann and J. McNamara):859–865, Tylor and Francis Group, 2005.

[143] L. Rondon, O. Pouliquen, and P. Aussillous. Granular collapse in a fluid: Role of the initial volume fraction. 23(7):073301, 2011.

[144] K. Terzaghi. *Theoretical Soil Mechanics*. John Wiley and Sons, 1943,.

[145] R. Iverson and R. G. LaHusen. Dynamic pore-pressure fluctuations in rapidly shearing granular materials. *Science*, 246:796–799, 1989.

[146] Y. Okada and H. Ochiai. Flow characteristics of 2-phase granular mass flows from model flume tests. *Engineering Geology*, 97:1–14, 2008.

[147] C. Deangeli. Pore water pressure contribution to debris flow mobility. *Am. J. Env. Sci.*, 5(4):487–493, 2009.

[148] G. Wang and K. Sassa. Pore-pressure generation and movement of rainfall-induced landslides: effects of grain size and fine-particle content. *Eng. Geol.*, 69:109–125, 2003.

[149] A. Casagrande. On liquefaction phenomena. *Geotech.*, 21(3):197–202, 1997.

[150] R. J. Finno, W. W Harris, M. A. Mooney, and G. Viggiani. Strain localization and undrained steady state of sand. *J. Geotech. Eng.*, 122(6):462–473, 1996.

[151] O. Hungr. A model for run out analysis of rapid granular flow slides, debris flows, and avalanches. *Can. Geotech. J.*, 32:610–623, 1995.

[152] J. N. Hutchinson. A sliding-consolidation model for flow slides. *Can. Geotech. J.*, 23(2):115–126, 1986.

[153] G. Mason and W. C. Clark. Liquid bridges between spheres. *Chem. Eng. Sci.*, 20:859–866, 1965.

[154] T. Gillisepie and W. J. Settineri. The effect of capillary liquid on the forces of adhesion between spherical solid particles. *J. Colloidal and Interface Science*, 24:199–202, 1967.

[155] J. C. Melrose. Model calculations for capillary condensation. *AIChE J.*, 12:986–994, 1966.

[156] S. H Liu and D. A. Sun. Simulating the collapse of unsaturated soil by DEM. *Int. J. Num. and Anal. Meth. Geomech Condens. Matter*, 26:633–646, 2002.

[157] U. E. Shamy and T. Groger. Micromechanical aspects of the shear strength of wet granular soils. *Int. J. Numer. Anal. Meth. Geomech.*, 32:1763–1790, 2008.

[158] K. Hotta, K. Takeda, and K. Iinoya. The capillary binding force of a liquid bridge. *Powder Tech.*, 10:231–242, 1974.

[159] S. C. Yang. Segregation of cohesive powders in a vibrated granular bed. *Chem. Eng. Sci.*, 61:6180–6188, 2006.

[160] S. T. Nase, W. L. Vargas, A. A. Abatan, and J. J. McCarthy. Discrete characterization tools for cohesive granular material. *Powder Tech.*, 116:214–223, 2001.

[161] P. Rognon and C. Gay. Soft dynamics simulation. 1. normal approach of two deformable particles in a viscous fluid and optimal-approach strategy. *The European Physical Journal E: Soft Matter and Biological Physics*, 27:253–260, 2008.

[162] G. Lian, C. Thornton, and M. Adams. A theoretical study of the liquid bridge forces between two rigid spherical bodies. *J. Colloid and Interface Science*, 61:138–147, 1993.

[163] H. Li and J. J. McCarthy. Phase diagrams for cohesive particle mixing and segregation. *Phys. Rev. E*, 71:021305, 2005.

[164] M. Zeghal and C. Medina. An analysis of the micro-micromechanical response of unsaturated granular soil deposits subjected to a dynamic excitation. *Geomechanics and Geotechniques of Particulated Media; edited by M. Hyoda, H. Murata and H. Nakata*, pages 241–246, 2006.

[165] R. M. Iverson. Elements of an improved model of debris-flow motion. (ed. Nakagawa, M. and Luding, S.). *Powders and Grains 2009, Proceedings of the Sixth International Conference on Micro-mechanics of Granular Media*, pages 9–16, 2009.

[166] M. Preisig and T. Zimmermann. Two-phase free-surface fluid dynamics on moving domains. *J. of Computational Physics*, 229(7):2740 – 2758, 2010.

[167] H. P. Zhu, Z. Y. Zhou, R. Y. Yang, and A. B. Yu. Discrete particle simulation of particulate systems: Theoretical developments. *Chemical Engineering Science*, 62(13):3378 – 3396, 2007.

[168] H. P. Zhu, Z. Y. Zhou, R. Y. Yang, and A. B. Yu. Discrete particle simulation of particulate systems: A review of major applications and findings. *Chemical Engineering Science*, 63(23):5728 – 5770, 2008.

[169] Benjamin K. Cook, David R. Noble, and John R. Williams. A direct simulation method for particle-fluid systems. *Eng. Comp.: Int. J. for Computer-Aided Eng.*, 21(2-3):151–168, 2004.

[170] A. V. Potapov, M. L. Hunt, and C. S. Campbell. Liquidsolid flows using smoothed particle hydrodynamics and the discrete element method. *Powder Technology*, 116(23):204 – 213, 2001.

[171] U. E. Shamy and M. Zeghal. Coupled continuum-discrete model for saturated granular soils. *Journal of Engineering Mechanics*, 131(4):413–426, 2005.

[172] H. Zhou, G. Flamant, and D. Gauthier. DEM-LES of coal combustion in a bubbling fluidized bed. part i: gas-particle turbulent flow structure. *Chemical Engineering Science*, 59(20):4193 – 4203, 2004.

[173] D. Furbish and M. W. Schmeeckle. Coupled large eddy simulation and discrete element model of bedload motion. *AGU Fall Meeting*, EP22A-07(26):San Francisco, Calif., 5–9 Dec, 2011.

[174] M. W. Schmeeckle. Detached eddy simulation (DES) of turbulence and suspended sediment transport in lateral separation eddies in the colorado river in grand canyon. *AGU Fall Meeting*, EP21B-0701:San Francisco, Calif., 5–9 Dec, 2011.

[175] Y. Tarumi and M. Hakuno. A granular assembly simulation for the dynamic liquefaction of sand. *Natural Disaster Science*, 10(1):45–59, 1988.

[176] R. R. Olivera Bonilla. Numerical simulations of undrained granular media. *PhD Thesis.*, University of Waterloo.

[177] Y. Okada and H. Ochiai. Coupling pore water pressure with distinct element method and steady state strengths in numerical triaxial compression tests under undrained conditions. *Landslides*, 4:357–369, 2007.

[178] R. H. Davis, J.-M. Serayssol, and E. J. Hinch. The elastohydrodynamic collision of two spheres. *J. Fluid Mech.*, 163:479–497, 1986.

[179] J.-M. Serayssol and R. H. Davis. The influence of surface interactions on the elastohydrodynamic collision of two spheres. *Journal of Colloid and Interface Science*, 114(1):54 – 66, 1986.

[180] G. Barnocky and R. H. Davis. Elastohydrodynamic collision and rebound of spheres: Experimental verification. *Phys. of Fluids*, 31(6):1324, 1988.

[181] R. H. Davis, D. A. Rager, and B. T. Good. Elastohydrodynamic rebound of spheres from coated surfaces. *J. Fluid Mech.*, 468:107–119, 2002.

[182] A. A. Kantak and R. H. Davis. Elastohydrodynamic theory for wet oblique collisions. *Powder Technology*, 168(1):42 – 52, 2006.

[183] J. S. Marshall. Viscous damping force during head-on collision of two spherical particles. *Physics of Fluids*, 23:013305, 2011.

[184] A. Lematre, J.-N. Roux, and F. Chevoir. What do dry granular flows tell us about dense non-brownian suspension rheology? *Rheologica Acta*, 48:925–942, 2009.

[185] R. Kaitna, M. C. Palucis, B. Yohannes, K. M. Hill, and W.E. Dietrich. Effect of fines and grain size distribution on pore fluid pressure and velocity profiles in large scale experimental debris flow. *In: European Geosciences Union (Ed.), Geophysical Research Abstracts*, 13:EGU2011–6312, 2011.

[186] S. J. de Vet, B. Yohannes, K. M. Hill, and J. R. de Bruyn. Collapse of a rectangular well in a quasi-two-dimensional granular bed. *Phys. Rev. E*, 82(4):041304, 2010.

Appendix A

Bagnold's Hypothesis

For theoretical derivation of pressure due to sheared granular flows Bagnold considered regular array of particle as shown in Figure A.1. In this ideal set up, the particles in the top layer (layer A) move at a velocity δu relative to the lower layer (layer B). As layer A passes over layer B, the particles collide and momentum is transferred. Bagnold defined a linear concentration parameter, $\lambda = \frac{d}{s}$. Then the frequency of collision between a particle in layer A and particles in layer B is proportional to $f(\lambda)\frac{\delta u}{s}$ where $f(\lambda)$ is function of the linear concentration. The number of particles per unit area in the horizontal plane is $\frac{1}{(d+s)^2}$. Assuming purely elastic collisions between particles, the change of momentum of a particle in layer A in y direction is $2m\delta ucos(\alpha_i)$, where m is the mass of the particle and α_i is the the collision angle between particles in layer A and B. Using the above assumptions the stress can be computed as

$$p = \frac{Force}{Area} \tag{A.1a}$$

$$p = Momentum\ transfer \times Frequency\ of\ collision \times \frac{1}{Area} \tag{A.1b}$$

$$p = 2m\delta ucos(\alpha_i) \times f(\lambda)\frac{\delta u}{s} \times \frac{1}{(d+s)^2} \tag{A.1c}$$

$$p = af(\lambda)\lambda\rho_s d^2 \left(\frac{du}{dy}\right)^2 cos(\alpha_i) \tag{A.1d}$$

Similarly the shear stress, τ, can be shown to be

$$\tau = af(\lambda)\lambda\rho_s d^2 \left(\frac{du}{dy}\right)^2 sin(\alpha_i) \tag{A.2}$$

Bagnold estimated the value of λ based on the volume fraction ν and maximum volume fraction ν_{max}. At ν_{max}, $s \to 0$ and $\lambda \to \infty$. From Fig. A.1, it can be shown that

$$\nu_{max} = \frac{\pi d^3/6}{kd^3} \tag{A.3a}$$

$$\nu = \frac{\pi d^3/6}{k(d+s)^3} \tag{A.3b}$$

$$\frac{\nu_{max}}{\nu} = [1 + s/d]^3 \tag{A.3c}$$

$$\lambda = \frac{1}{\left[\frac{\nu_{max}}{\nu}\right]^{\frac{1}{3}} - 1}. \tag{A.3d}$$

In the above equations k is a proportionality constant as defined by Bagnold [11]. To verify these hypothesis and determine the fitting parameters a and $f(\lambda)$, Bagnold carried out experiments of suspended uniform spherical particles in a density matching fluid in a Couette cell. Eqs. A.1 and A.2 were in agreement with the experiments for concentrations, $\nu > 0.09$. Below this concentration the viscous forces dominates the stresses. For $\nu = 0.09$, $tan(\alpha_i) \approx 0.32$. For $\lambda < 12$, $a = 0.42$ and $f(\lambda) = \lambda$.

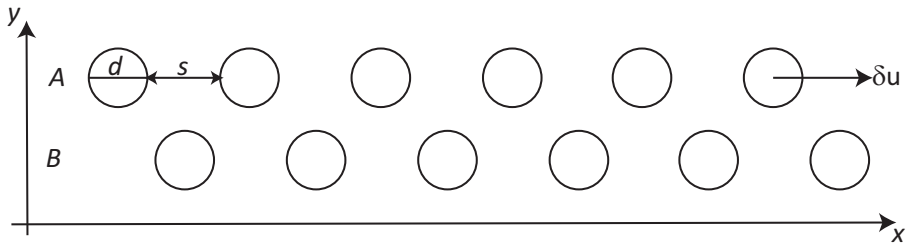

Figure A.1: The schematics shows idealized system of sheared layers of particles.

Appendix B

Calculations for particle size and force statistics

In this Appendix we demonstrate how we calculate the statistics presented in the text.

As mentioned in Section 4.2, to compare force data from the simulations to that from the experiments in the big drum, we consider the sum of all forces normal to the bed in the region where there are no treads, which we label the force sensor in Fig. 4.1(b). To compute the force that corresponds to an individual force sensor readout at drum position θ (reference angle shown in Fig. 4.2(a)), we add all of the normal forces between particles and the drum bed within the 15 cm $\times$ 2.1 cm region corresponding to the force sensor while the drum is rotated by an angle $\Delta\theta = \Omega/\Gamma$, where Ω is the drum rotation speed and Γ is the data output frequency (1kHz). We divide this net force by the number of discrete time steps in the simulation that occur over a time interval. Since the force sensor output from the experiments and simulations results from force distributed over the area of the sensor, we report the measurements in terms of a normal boundary stress, or pressure p_4:

$$p_4(\theta, \Theta, t_o) = \frac{\sum_{\tau=1}^{N_\tau} \sum_{i=1}^{N_{c,4}(\tau)} f\left(\theta_i, t_i\right)}{A N_\tau} \tag{B.1}$$

where the subscript "4"(in p_4 and $N_{c,4}$) is approximately equal to the angle over which the sensor extends (here, $\approx 4.3^{\circ}$) and thus the angle over which the averaging takes place. i refers to the ith contact made between a particle and the part of the wall

corresponding to the simulated sensor at time τ of which there are $N_{c,4}(\tau)$. Θ refers to the angle over which the sensor extends (≈ 4.3 °). θ_i is the azimuthal location of that contact and at time t must satisfy $\theta_s - \Theta/2 < \theta_i < \theta_s + \Theta/2$ where $\theta_s(t)$ is the angular position of the center of the sensor at time t. t_i refers to the time at which that contact is recorded and must satisfy $t_o + 1/2\Gamma > t_i > t_o - 1/2\Gamma$, where t_o refers to the time at which the middle of the simulated sensor passes θ. A is the area of the sensor. N_τ is the total number of time steps.

$p_{4,\sigma}$ denotes the standard deviation of $p_4(\theta)$ for each 1° bin. Specifically, for a particular degree bin containing N normal stress measurements whose mean is $\overline{p}_4$,$p_{4,\sigma} = \sum_{k=1}^{N}(p_k - \overline{p}_4(\theta))^2/(N-1)$. (Please see Fig. 4.2(c).)

For a representative measure of the local particle size, we consider the mass- averaged local particle size $\overline{d}(\theta)$

$$\overline{d}(\theta) = \frac{\sum_{\tau=1}^{N_\tau}\sum_{j=1}^{N_p(\tau)} m_j(\theta_j,\tau)d_j(\theta_j,\tau)}{\sum_{i=1}^{\tau}\sum_{j=1}^{N_p(\tau)} m_j(\theta_j,\tau)} = \frac{\sum_{\tau=1}^{N_\tau}\sum_{\tau=1}^{N_p(\tau)} d_j^4(\theta_j,t_i)}{\sum_{\tau=1}^{N_\tau}\sum_{\tau=1}^{N_p(\tau)} d_j^3(\theta_j,t_i)} \tag{B.2}$$

Here, $m_j(\theta_j,\tau)$ and $d_j(\theta_j,\tau)$ are the mass and diameter, respectively, of the jth particle at time τ whose center is at a location θ_j, where $\theta - \frac{1}{2}^\circ < \theta_j \leq \theta + \frac{1}{2}^\circ$. $N_p(\tau)$ is the number of such particles at time τ.

To determine how normal stress or pressure on the boundary, p varies with local particle size distribution, we consider certain statistical measures of the force at 1° intervals along the drum bed. For angular position θ, we consider contact forces within a 1° bin centered at θ. In the following, $f_j(\theta_j,\tau)$ represents the normal force associated with the jth contact at time step τ between a particle and the drum bed at an angle θ_j satisfying $\theta - \frac{1}{2}^\circ < \theta_j \leq \theta + \frac{1}{2}^\circ$. We use $N_c(\tau)$ to represent the number of such contacts at time step τ, of which there are N_τ. We use A_1 to represent the area at the drum bed over which the forces between particles and the wall are recorded for each 1^o section: $A_1 = (\pi D/360) \times 0.15$ m $\approx 7.33 \times 10^{-4}$ m^2.

Based on these considerations, we calculate a local pressure, the sum of all normal contact forces within a bin divided by the area of that bin:

$$\overline{p}(\theta) = \frac{\sum_{\tau=1}^{N_\tau}\sum_{j=1}^{N_c(\tau)} f_j(\theta_j,\tau)}{N_\tau A_1} \tag{B.3}$$

The pressure associated with the component of the gravitational force due to the local mass normal to the drum bed is analogous to the hydrostatic or lithostatic pressure

in a continuous system. For this calculation, as above, $m_j(\theta_j, \tau)$ and $d_j(\theta_j, \tau)$ are the mass and diameter, respectively, of the jth particle at time τ whose center is at a location θ_j, and , $\theta - \frac{1}{2}^\circ < \theta_j \leq \theta + \frac{1}{2}^\circ$. $N_p(\tau)$ is the number of such particles at time τ. Then the "lithostatic" pressure $\overline{p}_w(\theta)$ may be calculated according to:

$$\overline{p}_w(\theta) = \frac{\sum_{\tau=1}^{N_\tau} \sum_{j=1}^{N_p(\tau)} m_j(\theta_j, \tau) g \cos\theta_j}{N_\tau A_1} \tag{B.4}$$

As for the spatial variability of p and d, for the spatial variability of certain basic statistics of the forces associated with particle.bed contacts we consider each particle and each contact between a particle and the boundary within a 1° bin centered at angular position θ. For a central measure of the local contact force, we consider the locally averaged force per contact $\overline{f}(\theta)$:

$$\overline{f}(\theta) = \frac{\sum_{\tau=1}^{N_\tau} \sum_{j=1}^{N_c(\tau)} f_j(\theta_j, \tau)}{\sum_{\tau=1}^{N_\tau} N_c(\tau)} \tag{B.5}$$

where, as above, $f_j(\theta_j, \tau)$ is the normal force at an angle θ_j at time step τ, $N_{c,\tau}$ is the number of contacts between particles and drum bed at time step τ. For a simple measure of the variability of the contact forces within each degree bin we consider the standard deviation of the force per contact within each bin f_σ and a measure of local maximum f_{max}.

$$f_\sigma(\theta) = \sqrt{\frac{\sum_{\tau=1}^{N_\tau} \sum_{j=1}^{N_c(\tau)} \left[f_j(\theta_j, \tau) - \overline{f}(\theta) \right]^2}{\sum_{\tau=1}^{N_\tau} N_c(\tau)}} \tag{B.6}$$

We consider how certain measures of the force statistics vary for the whole system as the average particle size of the system d_{sys} varies, where:

$$d_{sys} = \frac{\sum_{i=1}^{N_p} m_i d_i}{\sum_{i=1}^{N_p} m_i} = \frac{\sum_{i=1}^{N_p} d_i^4}{\sum_{i=1}^{N_p} d_i^3} \tag{B.7}$$

N_p is the number of particles in the system, and m_i and d_i represent the particle mass and diameter of the ith particle, respectively. We also considered the measures of forces per contact over the whole system:

$$\overline{f}_{sys} = \frac{\sum_{\tau=1}^{N_\tau} \sum_{j=1}^{N_c(\tau)} f_j(\tau)}{\sum_{\tau=1}^{N_\tau} N_c(\tau)} \tag{B.8a}$$

$$f_{\sigma,sys} = \sqrt{\frac{\sum_{\tau=1}^{N_\tau} \sum_{j=1}^{N_c(\tau)} \left[f_j(\tau) - \overline{f}_{sys} \right]^2}{\sum_{\tau=1}^{N_\tau} N_c(\tau)}} \tag{B.8b}$$

$f_j(\tau)$ represents the jth particle-bed contact at any point on the wall at time τ (of which there are $N_c(\tau)$).